The Galactic Bulge Morphology

With Applications to the Fermi GeV Excess

Phaedra Coleman

School of Physical and Chemical Sciences
University of Canterbury

This dissertation is submitted for the degree of
Doctor of Philosophy

December 2020

For Timothy

Acknowledgements

I'd like to thank my supervisor Chris for his mentorship and persistent support. Thanks Dylan for your consistent depth of astrophysical insight and clarity. Thanks to Harrison, Martin, and Oscar for their continued collaboration on research projects with me. I'd also like to thank the following people for their company, support, criticism, and/or insight (in alphabetical order): Alex, Amber, Ari, Asta, Ben, Becca, Chris, David, Ethan, Fabian, grandparents, grateful dead, Jack, Jacob, Jake, Jenni, Jenny, Jenny, Jonty, Josip, Mike, Moe, Orlon, parents, Rosalie, Sarang, Sharlene, siblings, Steve, Toby, Victor.

Abstract

The current generation of near-infrared imaging of the Milky Way with photometric catalogues enables us to see further into the structure of the inner galaxy. With recent deep photometric catalogues extracted out of data released from the Vista Variables in Via Lactea (VVV) survey, we reconstruct the stellar density of the Galactic bulge via several methods. We fitted parametric models which are used as priors in our non-parametric maximum entropy and algorithmic smoothing regularised likelihood optimisation using a semi-analytic luminosity function of red giant stars constructed from stellar isochrone models. Our reconstruction naturally inpaints overcrowded and high extinction regions with curvature based inpainting via the algorithmic smoothing. Assuming two-fold symmetry we obtain our non-parametric bulge model over the inner $40^\circ \times 40^\circ$ region centred on the Galactic centre. Our resulting bulge properties from our best fitting model and systematics were found to be consistent with other investigations utilising the VVV data.

In further investigation of the VVV bulge data, we observed a stellar density in front of the bulge which provided a near side counterpart to the spiral arm structure behind the bulge previously observed in the literature with VVV catalogues. We determined that these features are sensitive to the modelling of the Red Giant Branch Bump and Asymptotic Giant Branch Bump components in our luminosity function construction.

Anomalous emission in the GeV energy range has been detected towards the centre of the Milky Way by the Fermi-Large Area Telescope (LAT). Theories proposed for this Galactic Centre Excess (GCE) include: self annihilation of dark matter particles, an unresolved population of millisecond pulsars, or a series of burst events. The diffuse emission of gamma-rays via cosmic-rays interacting with the interstellar gas and radiation fields dominates the sky in the energy range of the excess. To apply models of the GCE to Fermi-LAT data, this background must be accounted for with care. We utilised a method of modelling the interstellar gas position that exploits hydrodynamic modelling in conjunction with previous gas modelling techniques. We found the hydrodynamic model improves the quality of fit to the Fermi data over

previous methods applied. We also found a boxy Galactic bulge and nuclear stellar bulge produced a statistically better fit to the GCE than a spherical excess that would be more indicative of dark matter self-annihilation. Based on this result we argue that the GCE is likely associated with the stellar population of the Galactic bulge rather than dark matter. Applying new bulge models from our morphological analysis of the Red Clump in VVV infrared data further improved the statistical preference for a non-spherical excess rather than a dark matter interpretation.

Contents

List of Figures

List of Tables

List of Abbreviations

Roman Symbols

2MASS	Two Micron All Sky Survey
AGBB	Asymptotic Giant Branch Bump
B/P/X	Boxy/Peanut/X-shaped
CASU	Cambridge Astronomical Survey Unit
CMD	Colour Magnitude Diagram
CNM	Cold Neutral Medium
CO	^{12}C monoxide
COBE	Cosmic Background Explorer
CR	Cosmic-Ray
DFGB	Diffuse Galactic Background
DIRBE	Diffuse Infrared Background Experiment
FB	Fermi Bubbles
GCE	Galactic Centre Excess
GIEM	Galactic Interstellar Emission Model
H_+	Ionised Hydrogen
H2	Molecular Hydrogen
HI	Atomic Hydrogen
ICS	Inverse-Compton Scattering

ILR	Inner Lindblad Resonance
IMF	Initial Mass Function
ISM	Interstellar Medium
ISRF	Interstellar Radiation Field
L-BFGS	Limited Memory Broyden-Fletcher-Goldfarb-Shanno
LAB	Leiden/Argentine/Bonn
LAT	Large Area Telescope
LMXB	Low-Mass X-ray Binary
LSR	Local Standard of Rest
MSP	Millisecond Pulsar
NFW	Navarro-Frenk-White
OGLE	Optical Gravitational Lensing Experiment
PSF	Point Spread Function
RC	Red Clump
RGBB	Red Giant Branch Bump
SDI	Single Detector Image
SPH	Smoothed Particle Hydrodynamics
TS	Test Statistic
VISTA	Visible and Infrared Survey Telescope for Astronomy
VVV	VISTA Variables in the Via Lactea
WIMP	Weakly Interacting Massive Particle
WNM	Warm Neutral Medium

Chapter 1

Introduction

The dawn of near infrared surveys in the 80's and 90's unveiled the Milky Way centre previously obscured by dust reddening (Minniti & Zoccali, 2008). Though the Galactic bulge was identified earlier by Baade (1946), and Galactic bar suggested from non-circular gas motion in the 21-cm line by de Vaucouleurs (1964), the presence of a Galactic bulge/bar was only firmly established through modelling of the COBE/DIRBE (Cosmic Background Explorer / Diffuse Infrared Background Experiment) space telescope data and gas kinematics through the 1990's (Binney et al., 1991; Blitz & Spergel, 1991; Weiland et al., 1994). The bulge is visible in the DIRBE K-band data, displayed in Fig. 1.1. These DIRBE models typically found a triaxial bar or boxy bulge with its major axis rotated at an angle in the range between 10 and 45 degrees to the Sun-Galactic centre line (Dwek et al., 1995; Bissantz et al., 1997; Freudenreich, 1998; Bissantz & Gerhard, 2002), this range encompassing the 30 to 45 degree bar rotation proposed earlier by de Vaucouleurs (1964). Subsequent near-infrared and optical surveys such as OGLE (Optical Gravitational Lensing Experiment) (Udalski et al., 1992), 2MASS (Two Micron All Sky Survey) (Skrutskie et al., 2006), and VVV (VISTA Variables in the Via Lactea) (Minniti et al., 2010) have provided us with increasingly sensitive observations of the stellar distribution towards the Galactic centre, allowing resolution of individual stars in the bulge.

This thesis will focus on the extraction of a morphological model of the Galactic bulge from infrared surveys. Astrophysical phenomena suggested to be traced by the bulge distribution, such as the distribution of millisecond pulsars, brings forth a natural application of the morphological model in contexts where these phenomena are difficult to sample with current limitations on our observational equipment. The result of applying bulge models from infrared surveys to gamma-ray data and other modelling

considerations in this process are then considered. This introductory chapter will review several structural features that may arise in disc galaxies and an observational overview of these structures in the Milky Way context. The impact of our Galaxy's nature towards the Galactic centre is then placed in the context of gamma-ray observations and the potential implications of these observations on the nature of dark matter and the evolution of millisecond pulsars.

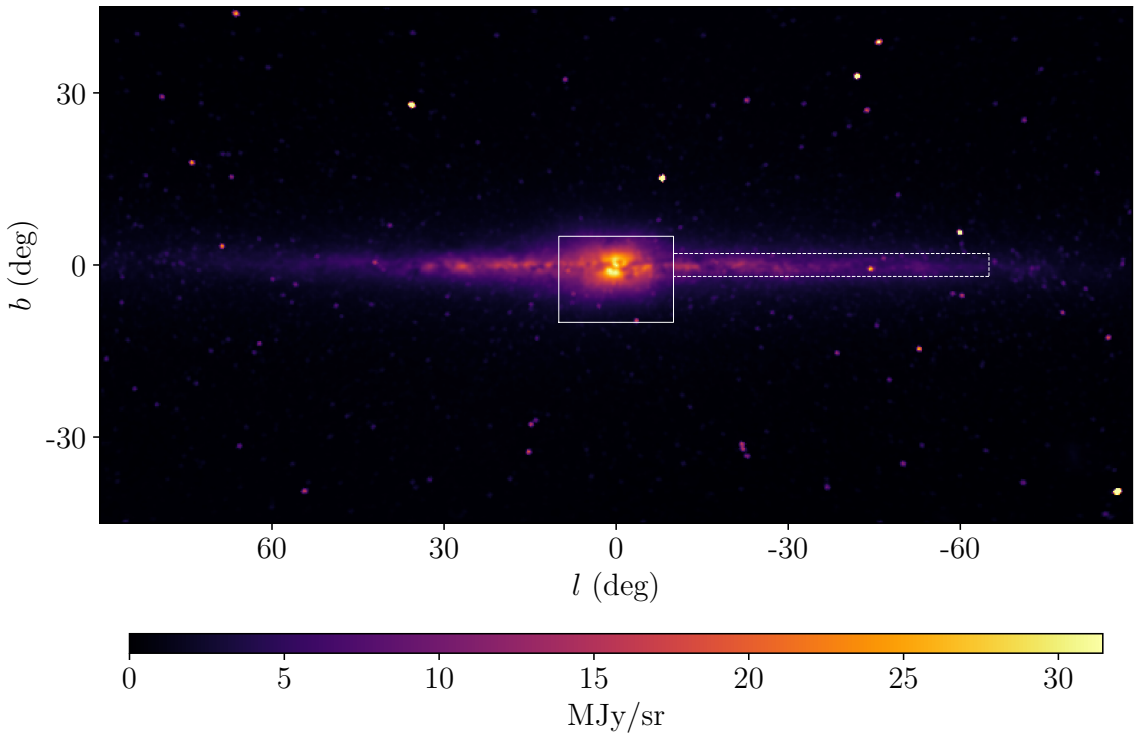

Fig. 1.1 Annual average COBE/DIRBE K-band emissivity map of the inner Milky Way in a Galactic Cartesian projection. The solid box bounds the VVV bulge window $-10° < l < 10°$ and $-10° < b < 5°$, and the dashed box outlining the VVV plane area survey.

1.1 Galactic Bar Formation

In disc galaxies, such as the Milky Way, an important dynamic structure which may form is a rotating bar in the centre of the disc. The formation of a Galactic bar in disc galaxies has multiple proposed formation channels, analysed predominantly through simulation. We summarise several scenarios discussed by Sellwood (2014).

Simple models of rotationally supported galactic discs have been known to be unstable via simulations as early as Hohl (1971). Sellwood (1989) investigated linear and non-linear instabilities which can produce bars. In the linear bar formation regime, disc instabilities can manifest in the form of an $m = 2$ azimuthal harmonic (or two-arm spiral). At the disc centre these arms can straighten out into a barred formation. This regime, which concerns small amplitude disturbances and predicts bar making modes, as above, should not possess Inner Lindblad Resonances (ILRs), where orbits overtake the potential. In the non-linear regime, in which disc perturbations are much larger in amplitude, the ILR is saturated with orbits trapped in the potential minimum, persisting thereafter in a barred formation. Alternatively, eccentric orbits of stars could result in their gradual capture in a slow rotating structure forming a bar. Lastly, the tidal interaction of a disc galaxy with satellite galaxies could induce bar formation, which can have a much slower rotation speed than the dynamically induced bars from normal disc instability (Miwa & Noguchi, 1998). Evidence of galaxies with nearby companions showing a greater rate of bar formation than those with more distant neighbours has remained inconclusive, leaving the significance of this channel of bar formation unclear.

If bars drive too much gas into their galaxy's centre, the complete dissolution of the bar may occur, meaning secular evolution processes, such as bulge formation, involving a bar could have occurred in some galaxies without observing one (Kormendy & Kennicutt, 2004). The methods of bar formation, prevention, and dissolution with the current state of the literature are still unable to explain the observed bar fraction in the universe (Sellwood, 2014). Instabilities occurring after bar formation such as buckling, will become relevant to later discussion.

1.2 Galactic Bulge Formation

The formation of structure in the central regions of galaxies can arise through several means, resulting in a range of morphological and dynamic phenomena. Bulge formation scenarios are typically grouped into two main families, those of classical bulges and pseudo-bulges. Though these distinct classifications are made, the existence of different bulge formations is not necessarily mutually exclusive. Erwin et al. (2015) observe nine S0-Sb galaxies with distinct classical bulge and discy pseudo-bulge components. However, below we discuss the bulge formation scenarios separately for conceptual clarity.

The classical bulge formation is expected to present radial profile similar to elliptical galaxies with an ellipsoidal shape (Athanassoula, 2005). Through simulation and observation, several possible formation histories of these classical bulges have been identified. The collapse of small scale density fluctuations comprised of old metal rich stars can trigger a starburst event resulting in a classical bulge which a disc later forms around, as explored in the simulations of Steinmetz & Muller (1995). Alternatively a disc may merge with another similar galaxy, stirring and concentrating disc stars into a central classical bulge formation, observed in simulation by Steinmetz & Navarro (2002). From observations of high red-shift discs, many have large star forming clumps which are suggested to rapidly sink via dynamical friction into the disc centre combined with inward dumping of cold gas inducing violent relaxation and star burst event producing a classical bulge (Kormendy, 2016). The high star formation rate in these clumps is expected to produce an enhancement of α-elements in bulge stars (Athanassoula, 2005).

Pseudo-bulges are the encompassing class of non-classical bulges. Two commonly described forms of pseudo-bulge are the discy bulge and the boxy/peanut/X-shaped bulge. The discy scenario involves the slower buildup of disc gas through secular evolution processes, concentrating disc gas in the central most regions, resulting in a classical bulge-like formation, though much flatter in distribution (Kormendy & Kennicutt, 2004). Boxy/peanut/X-shaped (B/P/X) bulges have several possible formation channels. In particular, we focus on the peanut/X-shape formation. The many proposed ways this type of pseudo-bulge can form appear to require a bar as a mediator (Sellwood, 2014). Athanassoula (2005) comment that the B/P/X bulge are a natural part of the evolution of barred galaxies. In particular, from the gradual acquisition of vertical motions relative to the disk plane or resonant heating (Combes & Sanders, 1981). In these resonant heating analyses, orbits in a vertical ILR following the bar contribute to a B/P/X-like structure, often in the form of a banana-like orbit when observed edge on, with two vertical oscillations per orbit (e.g. Combes et al. (1990) and Pfenniger & Friedli (1991)).

Buckling instability of the bar can drive the formation of the B/P/X bulge through weakening the bar and concentrating matter towards its centre, which Sellwood (2014) considers to be the principle driver of the B/P/X shape. Raha et al. (1991) examine galactic bar buckling in the context of a Kelvin-Helmholtz-like instability, dubbed the fire-hose instability (Toomre, 1966; Araki, 1985), as a buckling process which may induce a B/P/X bulge in the galaxy centre. Though rotationally supported discs were understood to be relatively robust to this instability, barring excessively flat

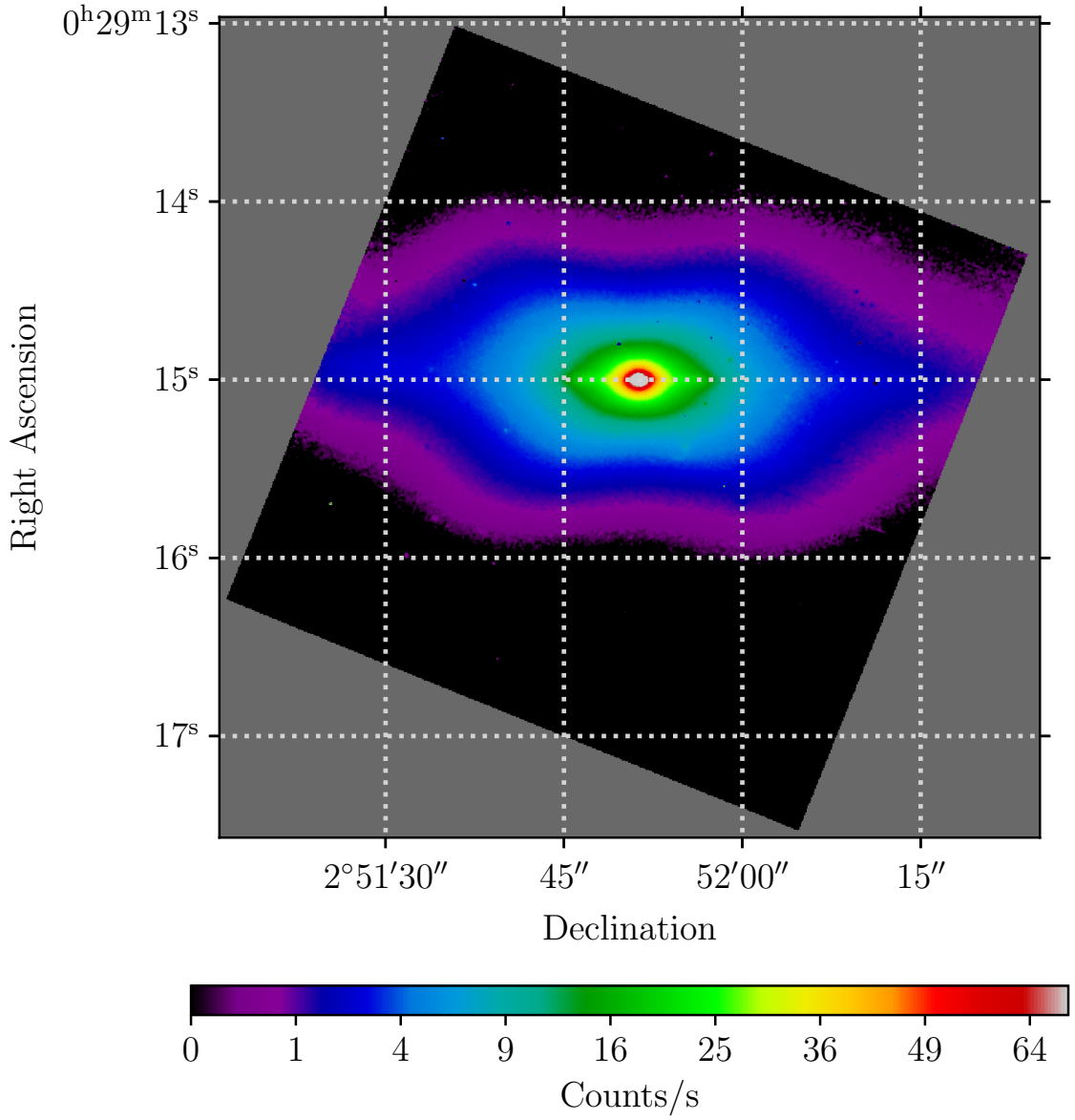

Fig. 1.2 Observation of NGC 128 in the optical spectrum. Based on observations made with the NASA/ESA Hubble Space Telescope, and obtained from the Hubble Legacy Archive, which is a collaboration between the Space Telescope Science Institute (STScI/NASA), the Space Telescope European Coordinating Facility (ST-ECF/ESA) and the Canadian Astronomy Data Centre (CADC/NRC/CSA). The colour map is in a square root scale to more clearly display the Peanut/X-shape peaks.

velocity dispersion, Raha et al. (1991) found the bar to be vulnerable to buckling via a fire-hose-like instability. The remaining peanut shape does not encompass the full bar length, resulting in a peanut shape with pointed flat bar ends (Sellwood, 2014).

In a simulation and orbital analysis of B/P/X bulge disc galaxies after buckling, Portail et al. (2015b) found a mixture of resonant and non-resonant "brezel-like" orbits, with similarity to an orbit family which requires 10 vertical and 6 horizontal orbits to close, provided a better orbital description than the 2:1 vertical ILR "banana-like" orbits in the orbital trapping bulge formation scenarios considered earlier. These brezel orbits allowed for a less radially broad peanut shape.

B/P/X bulges have been observed in edge-on external galaxies. For example, the barred lenticular galaxy NGC 128, displayed in Fig. 1.2, from the Hubble Space Telescope, has been observed to have these features as early as Burbidge & Burbidge (1959) in which they describe apparent four equal bulge-like components parting from the nucleus like a cross. Additional curious structural properties of NGC 128 were uncovered by Ciambur & Graham (2016), in which two co-existing bars with inner peanut bulge components associated with each corresponding bar were observed in their modelling.

1.3 The Milky Way Bulge

The Milky Way bulge exhibits kinematic and structural properties strongly suggestive of a B/P/X-shaped inner bulge. The formation of a B/P/X bulge being the result of secular evolution processes in a galactic bar would appear to explain the discrepancy between the angles of bars in DIRBE models, as the B/P/X formation involves a concentrating of a bar towards the centre. This is reflected by works such as Wegg et al. (2015) in which a long bar component extending from the bulge was identified. This was also supported by N-body simulations which could reasonably reproduce this observation, where the boxy bulge and long bar can hold together as a single unifying structure (Martinez-Valpuesta & Gerhard, 2011). The blending of bar and bulge in the B/P/X scenario leads us to refer to this bulge/bar component as "the bulge" throughout this work, as suggested by Zoccali & Valenti (2016).

The simultaneous presence of a substantial classical bulge component in the Milky Way is less clear. In modelling the ARGOS and GIBS surveys, Shen et al. (2010) places an upper bound on the possible classical bulge mass of about 8% of the disc mass in simulations where the bar forms from an exponential disc comprising 55% of the total mass. Galaxy formation scenarios discussed in Saha & Gerhard (2013) suggest that finding kinematics of the spheroid population distinct from the pseudo-bulge may prove difficult if the galaxy formed around an initial classical bulge that spun

up with the bar. Kunder et al. (2016) find that RR Lyrae exhibit negligible rotation, demonstrating these stars exhibit a classical-bulge-like structure separate from the bar. The kinematically hot component exhibiting this distribution amounted to less than 1% of the central mass of the galaxy.

Metal poor stars attributed to a classical spheroidal bulge shape may in fact be part of the thick disc and stellar halo of the inner galaxy (Ness & Freeman, 2016). Studies of metallicity with kinematics such as Babusiaux et al. (2010); Ness et al. (2013) also found more metal rich stars tended to follow bar-like orbits and metal poor stars follow more spheroidal shaped orbits. The conflicting conclusion in Vásquez et al. (2013) was later suggested to have been a result of foreground contamination (Rojas-Arriagada et al., 2014; Babusiaux, 2016).

Relating to this observation of metallicity correlating to the orbits that trace the bulge structures, the morphology of the bulge can depend heavily on the choice of stellar tracer. While the Red Clump (RC) modelling typically produces a more peanut-like or X-shaped bulge in the literature (Nataf et al., 2010), old variable stars RR-Lyrae provide a different picture of the Galactic bulge to RC stars, tracing out a spheroidal shape of the galaxy (Dékány et al., 2013). The observation of different tracers not producing a B/P/X shape, or in particular, the apparent double peak that can result from the processes discussed in Section 1.2 when viewed along lines-of-sight from certain angles to the bulge, has resulted in some works disputing the observation of this morphology. The young F0-F5 main sequence stars (López-Corredoira, 2016) and Mira variables (López-Corredoira, 2017) disfavour a peanut-like or X-shaped interpretation. However, the young F0-F5 star populations may be of negligible impact to the structure of our interest as the proportion of stars in the bulge younger than 5 Gyr appears to be bounded by around 3.4% (Clarkson et al., 2011).

A split in the magnitude distribution of RC stars of about 0.4 mag was predicted by Girardi (1999) between helium enhanced stars and a population of stars with just enough mass for helium to ignite in non-electron-degenerate conditions. This provided a theoretical population-based explanation of a gap comparable to the split RC observed. An absolute magnitude separation of such order was observed in RC stars by López-Corredoira et al. (2019), finding it unlikely that both peaks could be explained by the same population of RC stars. From a chemical standpoint, the study of Lee et al. (2019) found that the observed sodium abundance bi-modality in the outer region of the bulge supports a spheroidal classical bulge formation history for the split RC as a population effect. However, the limits on a classical bulge component placed by Shen et al. (2010) and Kunder et al. (2016) could mean a classical bulge (if present) combined with a

pseudo bulge would have insufficient mass to produce the geometric interpretation of Lee et al. (2015). The age-based mass bounds of 3.4% for stars younger than 5 Gyr in the bulge by Clarkson et al. (2011) may significantly constrain the importance of the faint peak in the population effect scenario of the split RC too, as those stars are predicted by Girardi (1999) to be predominantly around 1 Gyr old.

Some works have incorporated kinematic data and metal content into their models of Milky Way morphological structure producing B/P/X bulges. By combining Bulge Radial Velocity Assay (BRAVA) measurements with the RC model of Wegg & Gerhard (2013), Portail et al. (2015a) further constrained the RC properties, such as mass estimates and rotation speeds. This was adapted to accommodate metallicity variations with ARGOS and APOGEE surveys, obtaining similar conclusions on the barred nature of metal rich populations as prior metallicity kinematic studies (Portail et al., 2017).

1.4 VISTA Variables in the Vía Láctea

The Visible and Infrared Survey Telescope for Astronomy (VISTA) 4.1m wide-field telescope observing in five pass-bands from 0.9-2.5 μm provides a particularly apt basis for investigating the Milky Way bulge population (Minniti et al., 2010). Covering a 300 deg^2 area around the Galactic bulge and 220 deg^2 adjacent plane region outlined in Figure 1.1, the observed area covers the majority of the bulge distribution. The VVV survey compiled from VISTA observations was intended for the construction of a 3-D survey of the bulge population, studying globular cluster evolution, gaining a clearer understanding of variable sources such as RR Lyrae and Cepheids, and extracting information on stellar population ages and probe star formation in the disk, among the many possible applications.

Initial data releases of the VVV photometric catalogues were based on aperture photometry (Saito et al., 2012), which suffers significantly in crowded regions. They noted then that PSF photometry would be expected to reach $\sim$1.5 mag deeper than the $\sim$16 mag typical in this release. Later PSF photometric catalogues were produced using PSF fitting photometry routines such as DAOPHOT (Stetson, 1987) and DoPHOT (Schechter et al., 1993), where DoPHOT fits analytic PSF functions while DAOPHOT works with a combination of analytic and empirical PSF forms. DoPHOT has an advantage of being mostly automated and computationally faster than DAOPHOT which requires much more user input. Mauro et al. (2013) using a DAOPHOT and ALLFRAME (Stetson, 1994) pipeline requiring less user input demonstrated this

approach can reach much fainter sources while offsetting much of the "repetitive interaction" of the user. ALLFRAME takes an object list produced by the often applied DAOPHOT/ALLSTAR pipeline and iteratively applies corrections to the brightness values and coordinates using the residuals from an object's current estimate. Surot et al. (2019) applied a similar pipeline to produce deep photometric catalogues for J and K_s bands while producing completeness estimates in every field. The earlier DoPHOT-based PSF catalogue of Alonso-García et al. (2018) provided a more comprehensive data set, but lacked these completeness estimates. The completeness estimation approach Surot et al. (2019) used involved artificial star injection into the single detector images (SDIs) of left and right detector halves, using J K_s magnitude pairs drawn from a 2D colour-magnitude distribution derived from the observed set. These images were reprocessed in the same way as the main catalogue minus the PSF modelling aspect. From the fraction of stars recovered to artificial stars added they determined a completeness value assignable to each star in the catalogue. This deep photometric catalogue of the VVV survey, with completeness correction and extinction correction pre-computed, provides the observational basis of our Milky Way bulge reconstruction. Chapter 2 presents our work published as Coleman et al. (2020) and Paterson et al. (2019), in which we systematically examine several methods of bulge density reconstruction, infer bulge properties, and explore potential features of interest within the observed region of the sky reconstructed from the VVV catalogue. The contributions of the author in these works include data preparation, implementation and development of deconvolution methods, and interpretation of results in a collaborative environment with their research team.

1.5 Gamma-Ray Astronomy and the Fermi-Large Area Telescope

The gamma-ray energy regime of astronomy concerns photons with energies of about a hundred keV and above (Knödlseder, 2016). Due to how gamma-rays interact with the Earth's atmosphere, gamma-ray observation is typically performed by either detecting the cascades produced in the atmosphere and reconstructing the event, or detectors raised into the stratosphere by balloons or launched into space. The dominant production of observed gamma-rays is typically attributable to two classes of process: relativistic cosmic-rays interacting with radiation fields, and particle decay (Degrange & Fontaine, 2015). These processes are discussed in further detail in Section 3.1 in the

context of the diffuse emission of gamma-rays explored in that chapter. Due to the narrow wavelength of gamma-rays, mirror based telescopes, as used in many of the lower energy bands, are no longer viable. Some approaches to detecting gamma-rays include (in order of increasing energy): Compton scattering based telescopes, pair production inducing telescopes, and Cherenkov radiation based telescopes (Knödlseder, 2016).

In this work we focus on the detection of gamma-rays via pair production based space telescopes, in particular the Fermi-Large Area Telescope (LAT). Fermi-LAT, designed for the study of the gamma-ray sky, was launched in 2008, encompassing energy ranges of about 20 MeV to over 300 GeV for sources across the full sky (Atwood et al., 2009). In this instrument, incident gamma-rays are expected to convert to electron-positron pairs when interacting with one of the tungsten layers. These tungsten layers are interleaved with positron-sensitive detectors which monitor the particle tracks resulting from one of the tungsten layers, allowing reconstruction of the incident photon's path. A calorimeter provides a measure of the gamma-ray's energy. In reconstructing the gamma-ray event, the probability distribution of the direction reconstruction is referred to as the point-spread function. Potential multiple scattering instances of the electron-positron pairs and bremsstrahlung effects create energy dependent limits on the telescope's resolution. Unless specified otherwise, "Fermi" in this work refers to the space telescope, with the LAT instrument described above and Gamma-ray Burst Monitor (GBM) on board.

The Fermi telescope was intended to monitor high energy gamma-ray bursts, catalogue thousands of high-energy sources across the sky accurately locating point sources in the process, obtaining a measure of the isotropic diffuse background, and explore the parameter space of dark matter candidates.

1.6 The Fermi Galactic Centre GeV Excess

Through applying standard modelling of diffuse gamma-ray emission and known gamma-ray sources, a significant anomalous emission in the energy range of a few GeV remained. The apparent spherical distribution of the so-called GeV excess, or Galactic centre excess (GCE) lead to speculation of a dark matter origin (Goodenough & Hooper, 2009; Abazajian & Kaplinghat, 2012; Gordon & Macías, 2013). Soon after this dark matter attribution, a spherically distributed millisecond pulsar (MSP) population in

the Galactic centre was proposed as a similarly appropriate explanation of the excess (Abazajian, 2011).

The modelling of interstellar emission from known sources has a significant impact on resolving the GCE. On 2 years of LAT data Boyarsky et al. (2011) found variation in the spectral models of known point sources could account for the GCE within the central 2 degrees of the Galactic centre. While residuals in the Galactic centre were found to be significant but spectral interpretation was heavily dependent on interstellar emission models by Ajello et al. (2016) and Calore et al. (2015b), affecting the ruling on interpretation of the excess.

In Chapter 3, based on our work published as Macias et al. (2018) and the GCE section of Coleman et al. (2020), we explore the addition of information of Galactic structure to improve on models of the Diffuse Galactic Background (DFGB) traced by gas as part of the interstellar emission model. We also examine astrophysical components in the Galactic centre which may trace or affect the resulting morphological signature of the GCE. The author's contributions that were ultimately included in this publication concerned the reproduction and construction of DFGB models, primarily the gas annuli maps and dust templates. Contribution to the interpretation of results was also involved.

The excess has become a testing ground for various phenomena such as dark matter, cosmic-ray bursts, and millisecond pulsar emission models that could reproduce this spectrum and spatial morphology. Cosmic-ray emission independent of dark matter by-products has been investigated as a possible source of the emission. Cholis et al. (2015) proposed leptonic cosmic-ray outbursts from the centre of the Galaxy producing gamma-ray emission, where models of this scenario could reproduce the GCE signal in the inner 1-2°. However, this required so far unobserved leptonic outbursts exhibiting the necessary properties, and the CR propagation and injection parameters required fine tuning and somewhat extreme values. Steady state CR propagation has also been studied as a source of the GCE signal in works such as Gaggero et al. (2015) and Carlson et al. (2016). However, Gaggero & Valli (2018) discuss the sorely needed advancement in the physics of CR transport, particularly in the case of efforts in dark matter indirect detection with Fermi-LAT. We employed the more standard approaches to CR transport currently available via GALPROP (Strong et al., 2011) in our analysis rather than attempt to build on this rapidly developing field. We discuss the dark matter and MSP interpretations in greater detail later in this chapter.

1.7 Dark Matter

The majority of matter content in the Universe has been attributed to cold dark matter. Recent estimates by the Planck Collaboration place the prevalence of dark matter at 84.3% of the matter in the Universe (Planck Collaboration et al., 2018). There are a multitude of dark matter candidates that have been proposed and tested. One compelling class of dark matter theorised is the Weakly Interacting Massive Particle (WIMP) (Jungman et al., 1996). Here, for brevity, we only consider this class of dark matter particle when dealing with the Fermi GCE. However, our methods in this work are relatively model independent, depending on the dark matter encounter rate for some self-annihilation channel, which follows the square of dark matter density, tracing ultimately the density morphology.

The reasoning behind the WIMP as a dark matter candidate typically goes as follows: In the early universe, at high temperatures, an electrically neutral particle such as the WIMP may be created and destroyed. At this stage, the distribution of WIMPs is in local thermal equilibrium. After the universe has expanded and cooled past a point, these particles will fall out of thermal-equilibrium and "freeze-out". The predicted annihilation cross section at freeze out results in a relic density close to the measured dark matter density in observations such as the Planck Collaboration (Bergström, 2012).

Towards the dense core of galaxies, the dark matter halo is expected to increase substantially in density. The consequence of this is a significant increase in self-annihilation rates in the WIMP regime. The self-annihilation of WIMP dark matter can produce gamma-rays (Bergström et al., 1998). The gamma-rays and gamma-ray producing byproducts of WIMP annihilation have been modelled in the context of the GCE e.g., (Hooper & Linden, 2011; Gordon & Macías, 2013; Abazajian et al., 2014; Calore et al., 2015a; Daylan et al., 2016). These works reproduce the energy spectrum of the GCE, typically using a Navarro-Frenk-White (NFW) spatial distribution (Navarro et al., 1996). This model prevailing as an adequate description of the excess would also provide non-gravitational evidence for the existence and nature of dark matter, inviting further study.

1.8 Millisecond Pulsars

Millisecond pulsars are simply defined as pulsars with a period in the millisecond range. The canonical formation scenario is that they are the result of old recycled neutron

stars spun up in a low-mass X-ray binary (LMXB) system with accretion from the binary companion (Alpar et al., 1982).

MSPs that cannot be resolved through current telescopes such as Fermi-LAT (unresolved MSPs) distributed through the Galactic centre provide an alternative explanation to dark matter for the GCE. The spectral energy distribution of MSPs have been found to be consistent with the GCE spectrum. For example the best fit energy spectrum for MSPs observed by Fermi-LAT and MSP populated globular cluster models, as performed by Macias & Gordon (2014) was found to be consistent with the GCE spectrum. A preference for a B/P/X bulge in gamma-ray data is suggestive of a potential MSP interpretation over dark matter. We might expect a MSP population tracing the bulge to exhibit additional morphological features of the system. We examine the MSP interpretation through the application of B/P/X-shaped parametric bulge models and fully non-parametric bulge models in this gamma-ray context in Chapter 3. Here we explore aspects of the MSP scenario for the GCE which motivate our interpretation of a stellar bulge distributed excess corresponding to such an origin.

Simulations of MSPs have shown that there can be a sufficient number of MSPs to produce the GCE without resolving a single MSP in the bulge region supposing that the bulge has a similar MSP luminosity function to what has been observed in the disc (Ploeg et al., 2017). For the case of pulsars for comparison (rather than MSPs), their gamma-ray lifetimes are on the order of a few Myr, meaning there needs to be some way for the pulsars to have formed recently. Outside the nuclear disc region of the bulge the star formation rate of the bulge is negligible, leaving most bulge stars with ages greater than 8 Gyr (Nataf, 2016), creating difficulties for this scenario. Meanwhile, MSPs may be generated from older stellar populations (Ploeg et al., 2017). Observations have found large numbers of MSPs may form in globular clusters in the Milky Way (Abdo et al., 2013). The tidal disruption of these clusters depositing MSPs into the bulge could produce sufficient gamma-ray producing MSPs to account for the excess. Modelling by Fragione et al. (2018) found that the disrupted globular cluster scenario should produce a spherically symmetric distribution, which we find in Chapter 3 to be inadequate. Changing the conditions of their model to have a B/P/X bulge with tidal globular cluster disruption could produce the appropriate distribution (Macias et al., 2019). This scenario is still developing in the literature, inviting further study.

Millisecond pulsar production observed and modelled in globular clusters may provide possible explanations for the production and retention of MSPs within the bulge (*in situ* formation) that could explain the GCE. The two MSP formation mechanisms considered by Macias et al. (2019) are the dynamical and primordial formation scenarios.

The dynamical formation scenario is the capture, or recycling, of neutron stars into low mass X-ray binaries leading to MSPs, i.e. the usually considered formation scenario for MSPs. The formation rate in this scenario depending on the observed correlation between stellar encounter rate and prevalence of LMXBs, the scaling of encounter rate, hence MSP rate, depending on the square of the stellar density (Hui et al., 2010). The primordial scenario here involving the formation of neutron stars in a pre-existing binary system. The rate of MSP occurrence, in this case, scales linearly with stellar density. These MSP scenarios in admixture can reproduce the GCE, and provided a statistically significant improvement on a dominant single formation explaining the GCE counts distribution (Macias et al., 2019).

Chapter 2

Modelling the Galactic Bulge

2.1 Introduction

For our investigation of the Galactic bulge, the main observational data set of interest is the VVV survey (Minniti et al., 2010), in particular, the stars occupying the Red Clump region of the Colour-Magnitude Diagram (CMD). The narrow dispersion of the RC (Chan & Bovy, 2019; Hall et al., 2019) combined with the photometric star catalogues in the near infrared regime enables estimates of the distance to stars based on their apparent magnitudes, though this comes with some caveats, including the effects of their age and metallicity distribution, and theoretical calibration uncertainties shared by the rest of the Red Giant Branch's evolution (reviewed in further detail by Girardi (2016)). The RC has been the focus of several studies characterising the three-dimensional density structure of the Galactic bulge. Many studies have exploited distance-magnitude related properties of the RC to fit triaxial models to the bulge (Stanek et al., 1997; Rattenbury et al., 2007; Cao et al., 2013; Simion et al., 2017). Non-parametric methods have also been used in viewing the RC distribution, initially with an assumed constant intrinsic RC magnitude (Saito et al., 2011), then later accounting for its intrinsic and metallicity dispersion in works such as Wegg & Gerhard (2013) (from here on, denoted by WG13). The Galactic RC magnitude distribution was found to produce a double photometric peak by Nataf et al. (2010) using OGLE-III data and McWilliam & Zoccali (2010) using 2MASS. This has been interpreted as being the result of an X-shaped structure which is characteristic of the B/P/X-like morphology seen in extragalactic studies of barred galaxies (e.g. Laurikainen et al., 2014; Ciambur & Graham, 2016) and N-body simulations (e.g. Gardner et al., 2014). Through the cross matching of VVV RC stars with *Gaia* in Sanders et al. (2019) and Clarke et al.

(2019) also found that the proper motions of the VVV RC stars indicate a spatial separation in the split RC peak. Objections raised about the main interpretation of the photometric split clump peaks were discussed in Section 1.3.

Triaxial symmetry has often been assumed in morphological studies, such as the analytic models used by Simion et al. (2017) (from here on, denoted by S17). The models used by S17 represent only a subset of the broader class of triaxial bulge models (Dwek et al., 1995). Triaxial symmetry has also been enforced for non-parametric studies such as that of WG13 (hereafter, eight-fold symmetry for this context) to overcome gaps in the data and improve signal to noise when producing their final model. In this chapter, we use maximum entropy and smoothness regularisation (Jaynes, 1957; Storm et al., 2017) to help estimate the bulge morphology. This allows us to make fewer symmetry assumptions and it also provides a natural way of inpainting masked regions and matching onto parametric fits outside the region of interest covered by the data.

In this chapter, we initially make a mirror symmetry assumption about the Galactic plane to enable a constrained extension of the non-parametric RC bulge model to the inner $40^\circ \times 40^\circ$ region, which is important for our intended applications to Fermi-LAT data in Chapter 3. In addition, we absorb into our background known features outside the bulge that may otherwise be picked up by the deconvolution. We also performed systematic checks of this bulge analysis pipeline. We later model the VVV data without any symmetry requirements, which enabled clear exposure of features adjacent to the bulge.

This chapter is arranged as follows: In Section 2.2 we provide an overview of our VVV data set preparation and our non-parametric deconvolution method for inverting stellar statistics to recover the three-dimensional RC density distribution. We also motivate our choice of parametric model as a prior distribution and as a simple geometric model of the bulge with an explicitly peanut/X-shaped morphology. In Section 2.3, we test our deconvolution pipeline against simulations. We present our results and discuss them in Sections 2.4 and 2.5. In Section 2.6, we estimate various properties of the bulge. Lastly, in Section 2.7, we examine features adjacent to the bulge, association of these features with previous literature, and their dependence on Red Giant Branch luminosity modelling.

2.2 Method

2.2.1 VVV Data Preparation

Several photometric catalogues have been compiled from the VVV data releases. We employed the MW-BULGE-PSFPHOT ultra deep photometric catalogue produced by Surot et al. (2019). This set itself being comprised of 196 tiles corresponding to the VVV survey tiles used in the catalogue construction, in which DAOPHOT/ALLFRAME PSF-fitting photometry has been applied to the J and K_s band images. Relevant properties of the catalogue stars include extinction corrected J and K_s apparent magnitudes, their corresponding photometric and combined errors, and completeness for each star.

This catalogue was calibrated on the Cambridge Astronomical Survey Unit (CASU) aperture photometry. The aperture catalogues have a known field to field variation in the K_s band zero-point, discussed in depth by Hajdu et al. (2019). We corrected for this zero-point variation using the 2MASS (Skrutskie et al., 2006) point source catalogue. Stars within $12 < K_s < 13$ in the VVV catalogue were cross-matched with 2MASS using a cross-match threshold of 0.1 arcseconds. The magnitude range was selected to ensure good photometric quality in both catalogues and the threshold limit set to reduce effects of crowding and source merging, rather than a previously used larger threshold of 1 arcsecond (Hajdu et al., 2019). For each tile in the VVV catalogue the median difference between the 2MASS stars and their VVV matches was computed. We corrected magnitudes tile-by-tile in the K_s magnitude band using these offsets. The resulting offsets from the cross-match are displayed in Fig. 2.1.

Our region of interest in the CMD of this catalogue is the Red Clump, which we select for by applying a colour-magnitude cut of $11 < K_s < 15$ and $0.4 < J - K_s < 1.0$ in extinction corrected magnitudes. We bin stars within this colour-magnitude window in an $(80 \times 100 \times 75)$ grid in (K_s,l,b) for ranges $-10^\circ < l < 10^\circ$, and $-10^\circ < b < 5^\circ$. Some stars in the catalogue lack a computed completeness value, so we computed the mean completeness within a voxel from stars with available data then divided the counts in that voxel by the completeness fraction to account for this.

We applied a mask of lines-of-sight to our binned data based on the mean error, σ, of extinction and K_s band errors rather than a colour-excess-based mask. This was to account for crowding and regions of more severe photometric error effects in the PSF photometric data. A boundary of $\sigma = 0.06$ was chosen, as displayed in the bottom panel of Fig. 2.1. This value was chosen by eye so the new mask approximately matches an $E(J-K) = 0.9$ boundary (displayed in the top left panel of Fig. 2.1) in the less

crowded regions of $|l|> 5°$, around the extinction-based masking value of similar works. A systematic check of this method is investigated in Section 2.5.

Lastly, we excluded lines-of-sight from the analysis known to contain a globular cluster using the GLOBCLUST (Harris, 2010) catalogue.

2.2.2 Luminosity Function

To convert a stellar density estimate into a stellar count prediction binned as our prepared data, we required a luminosity function for the CMD window we selected. In works such as Wegg & Gerhard (2013) and Simion et al. (2017), a luminosity function had been produced by drawing masses from an initial mass function (IMF), for some age and metallicity, then interpolating the mass-magnitude relations in isochrones to assign absolute magnitudes to each star drawn. Parametric models such as Gaussians and exponentials would then be fitted to the resulting distribution to extract the distinct populations of the luminosity function such as the RC, Asymptotic Giant Branch Bump (AGBB), and Red Giant Branch Bump (RGBB).

We adopted a semi-analytic approach to constructing our luminosity function using the PARSEC+COLIBRI isochrone sets of Marigo et al. (2017) and a Chabrier log-normal Initial Mass Function (IMF) (Chabrier, 2003).

For a given age, τ, and metallicity, z, the luminosity function is

$$\phi\left(M_{K_s}, z, \tau\right) = \sum_i \xi\left(\theta_i^{-1}\left(M_{K_s}, z, \tau\right)\right) \left| \frac{d\theta_i^{-1}\left(M_{K_s}, z, \tau\right)}{dM_{K_s}} \right| \tag{2.1}$$

where ξ is the IMF and θ is the mass-absolute magnitude relation

$$M_{K_s} = \theta\left(m, z, \tau\right). \tag{2.2}$$

As the mass-absolute magnitude relation is not uniquely invertible everywhere, the luminosity function takes the sum of all possible solutions to the inversion of θ. Taking the expected value of Eq. 2.1, where f is our metallicity distribution function, we have our luminosity function for the full population:

$$\Phi\left(M_{K_s}\right) = \int_{-\infty}^{\infty}\int_{-\infty}^{\infty} \phi\left(M_{K_s}, z, \tau\right) f\left(z, \tau\right) dz d\tau. \tag{2.3}$$

Following (Zoccali et al., 2008), we assumed a single bulge age of 10 Gyr and a normally distributed metallicity with solar mean metallicity $\mu_{[\mathrm{Fe/H}]} = 0.0$ and a dispersion of

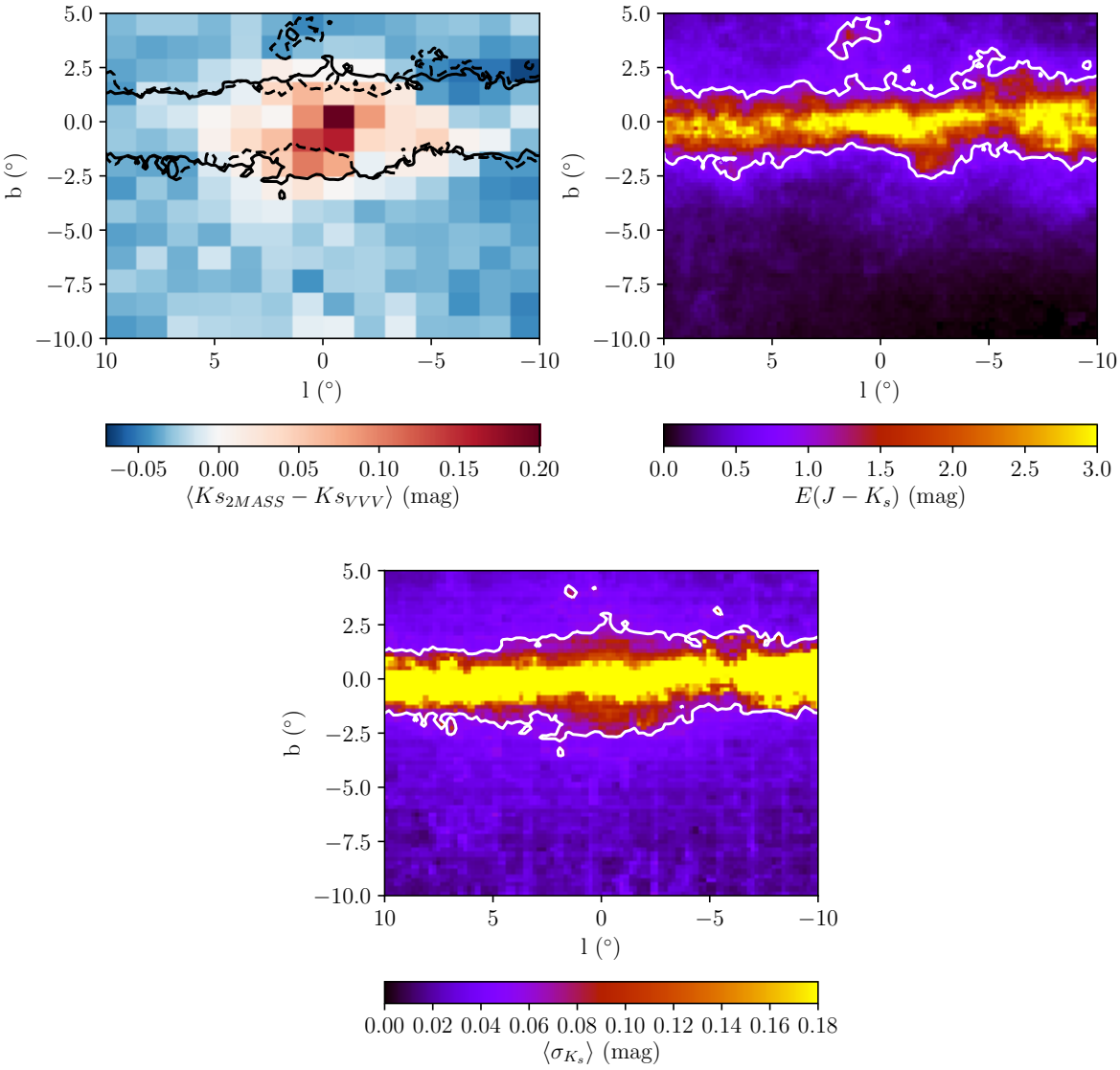

Fig. 2.1 *Top Left:* Median difference in K_s between cross matched 2MASS and VVV sources. We used this difference to correct the photometric zero-point within each tile. The solid line is the $\langle\sigma_{K_s}\rangle = 0.06$ mask boundary and the dashed line is the $E(J-K_s) = 0.9$ mask boundary. *Top Right:* Colour excess used in the extinction correcting the MW-BULGE-PSFPHOT photometry. Inside the white boundary, $E(J-K_s) > 0.9$, extinction severely degrades the quality of the VVV photometry. *Bottom:* Mean over $12.975 < K_s < 13.025$ of the combined photometric and systematic K_s uncertainty from the PSF fitting procedure used in compiling the MW-BULGE-PSFPHOT catalogue. Inside the white boundary, $\langle\sigma_{K_s}\rangle > 0.06$, the photometry is affected by the increased crowding, causing blending and source confusion.

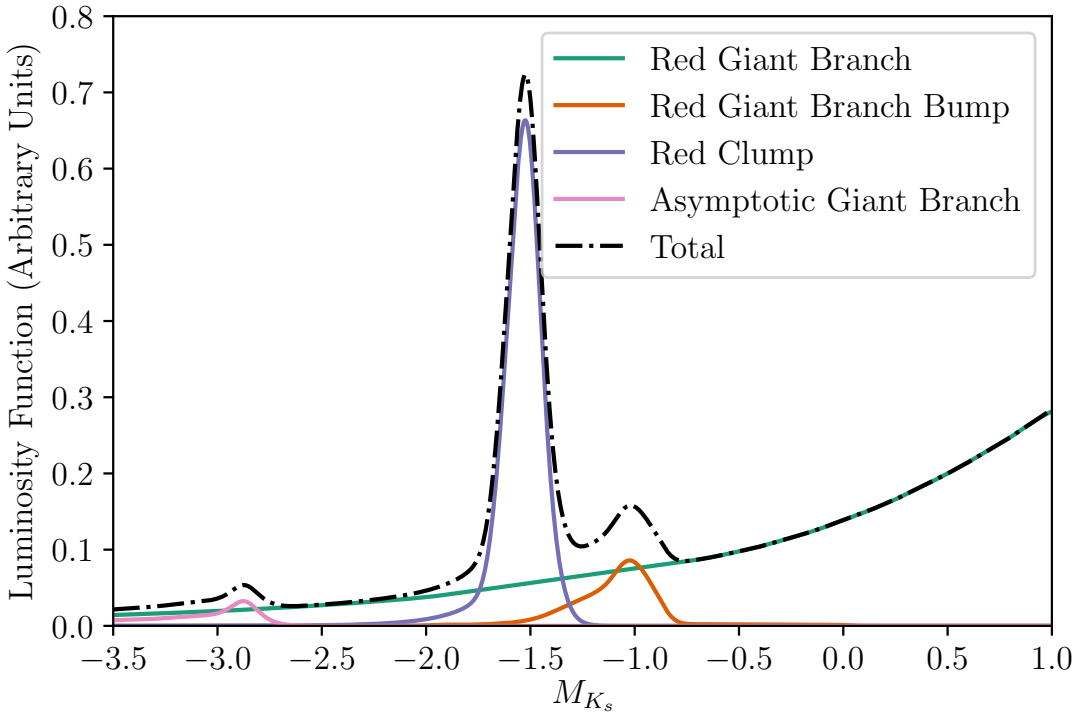

Fig. 2.2 Luminosity function of a 10 Gyr old population with $\langle[\mathrm{Fe/H}]\rangle = 0.0$ and $\sigma_{[\mathrm{Fe/H}]} = 0.4$ using PARSEC+COLIBRI isochrones and Chabrier (2003) log-normal IMF. We convolved the luminosity function by a Gaussian with standard deviation equal to the combined photometric and systematic uncertainty in K_s. For display purposes, the luminosity function, in this figure, was convolved with a Gaussian with $\sigma = 0.05$ which is a typical value for the error in K_s.

$\sigma_{[\mathrm{Fe/H}]} = 0.4$. An exponential function was fitted to the red giant branch, excluding the absolute magnitude range $-1.75 < M_{K_s} < -0.75$, to extract the RGBB component.

2.2.3 Deconvolution Procedure Fundamentals

The stellar density (ρ) of the Galactic bulge can be reconstructed by inverting the equation of stellar statistics (López-Corredoira et al., 2000):

$$N(K_s,l,b) = B(K_s,l,b) + \Delta\Omega\Delta K_s \int_{4\,\mathrm{kpc}}^{13\,\mathrm{kpc}} \rho(s,l,b)\,\Phi(K_s - 5\log s - 10)\,s^2\,\mathrm{d}s, \qquad (2.4)$$

where N is the predicted number of stars in a voxel centred at (K_s,l,b) and B is the number of smooth background stars in the voxel that are neither RC or RGBB stars. The $\Delta\Omega$ denotes the solid angle subtended by the line-of-sight, ΔK_s is the width of

the K_s magnitude bin, and s (measured in kpc) is the distance from the Sun. The luminosity function Φ is the sum of the bulge RC and bulge RGBB luminosity function components. Note that as the RGBB is a much smaller component than the RC, we sometimes refer to our obtained density in terms of the RC only, but more precisely it does contain both the RC and RGBB. As the Galactic bulge density tends to become negligible beyond several kpc, we only integrate the range $4\ \mathrm{kpc} \leq s \leq 13\ \mathrm{kpc}$ when computing the bulge contribution in modelling stellar counts.

Our analysis uses penalised likelihoods with penalties which come in two general forms: the first is maximum entropy regularisation, inspired by its application in Storm et al. (2017), which is defined for a 3-D grid of numbers q,

$$-2\ln\mathcal{L}_{MEM} = 2\lambda \sum_{i,j,k} \left(1 - q_{i,j,k} + q_{i,j,k}\ln q_{i,j,k}\right) \tag{2.5}$$

where i, j, and k are the grid points for K_s, b, and l respectively. The maximum entropy regularisation has a minimum at $q_i = 1$, so for our application we will use a parameterisation where q is the ratio between a modelled quantity of interest and a smooth prior estimation of the quantity. As shown in Section 2.2.6, the prior relative standard deviation of the reconstructed density from the prior density is of order $1/\sqrt{\lambda}$. So, the larger the value of λ chosen, the smaller the prior uncertainty assumed and so the more regularisation of the solution is applied.

The second form of likelihood penalty we use is the ℓ_2-norm regularisation of the second derivative of the logarithm of some quantity (also inspired by its application in Storm et al. (2017)). For a 3-D grid of numbers, F, which varies over one dimension, we use the second order central difference equation approximation of curvature:

$$-2\ln\mathcal{L}_{\mathrm{smooth}} = \eta \sum_{i} \left(\ln F_{i-1} + \ln F_{i+1} - 2\ln F_i\right)^2 . \tag{2.6}$$

This penalty has a minimum when F is the exponential of a linear function of grid coordinates. As shown in Section 2.2.6, the prior relative standard deviation from an exponential of a linear function is approximately $1/\sqrt{6\eta}$. So, the larger the value chosen for η, the more smoothness regularisation is applied.

2.2.4 Background

We modelled the background (B) non-parametrically as a free parameter for each (K_s, l, b) voxel. Without regularisation we would have a Poisson likelihood for data

Table 2.1 Regularisation parameters used when fitting to the simulated population and the VVV sample.

	λ	η_s	η_l	η_b
Background	1.0	1000.0	100.0	100.0
3-D Deconvolution	0.01	400.0	200.0	100.0

$n_{i,j,k}$ with expected counts $B_{i,j,k}$ where i,j,k are the grid points for (K_s,l,b) respectively. With maximum entropy and smoothness regularisation, we have the following formula for the natural log of the penalised likelihood ($\mathcal{L}$):

$$\begin{aligned}\ln\mathcal{L} = \sum_{\{i,j,k\}\in\{K_s,l,b\}} \Big[& n_{i,j,k}\ln B_{i,j,k} - B_{i,j,k} \\ & -\lambda\left(1 - q_{i,j,k} + q_{i,j,k}\ln q_{i,j,k}\right) \\ & -\eta_{K_s}\left(\ln B_{i-1,j,k} + \ln B_{i+1,j,k} - 2\ln B_{i,j,k}\right)^2/2 \\ & -\eta_l\left(\ln B_{i,j-1,k} + \ln B_{i,j+1,k} - 2\ln B_{i,j,k}\right)^2/2 \\ & -\eta_b\left(\ln B_{i,j,k-1} + \ln B_{i,j,k+1} - 2\ln B_{i,j,k}\right)^2/2\Big],\end{aligned} \tag{2.7}$$

where q is the ratio between our background model and a smooth prior estimation of the background:

$$q \equiv \frac{B}{B_{\rm prior}}. \tag{2.8}$$

The first line on the RHS of Eq. 2.7 is from the usual Poisson likelihood distribution. The second line is an entropy regularisation of the form of Eq. 2.5 and the third, fourth, and fifth lines are smoothness regularisations of the form given in Eq. 2.6 for K_s, l, and b respectively. The regularisation parameter values we used are listed in Table 2.1 and we discuss their choice in Section 2.3. We maximised Eq. 2.7 using the magnitude ranges $11 < K_s < 11.7$ and $14.3 < K_s < 15$, see Section 2.3 for more details. This means the behaviour in $11.7 \leq K_s \leq 14.3$ is determined entirely by the prior, maximum entropy, and smoothness regularisation.

The background is mainly composed of red giant stars in the bulge and foreground disc stars, so for the prior background ($B_{\rm prior}$) we used the S-model+discs fitted by S17 with the RC and RGBB components subtracted. Only the asymptotic giant branch and red giant branch (excluding the RGBB) components of the semi-analytic luminosity function are used for the bulge component in determining the background. Included in the S-model+discs are thin and thick disc components of the Besançon

galaxy model of Robin et al. (2003), where we have used the thin disc and thick disc parameters tabulated in Table 2.2. The S-model+discs of S17 was fitted to aperture photometry of the VVV DR2 data in the range $12 < K_s < 14$, so the background was underestimated for some lines-of-sight. To compensate for this, we multiplied each pixel (line-of-sight-wise) of the prior background by a constant, so that its mean matched the mean of our data in the range $11 < K_s < 11.5$ mag. Initial tests of our deconvolution method on the VVV data showed that our method was finding a feature in the density consistent with the structure behind the bar reported in Gonzalez et al. (2018), investigated further in Section 2.7. As we are trying to determine the bulge component, we decided to add this feature to our background, by first estimating our density using our maximum entropy background, then adding the star counts associated with any density significantly greater than our prior parametric density (see SX model of Section 2.2.7) to the maximum entropy background. We considered any density which was beyond the limits

$$\begin{array}{ll} s > 10 \text{ kpc} & l \geq 0^\circ \\ s > (10 - 0.1818\, l) \text{ kpc} & l < 0^\circ \end{array} \tag{2.9}$$

and at least 2.6×10^{-5} stars pc^{-3} sr^{-1} above the parametric model density to be part of the structure behind bar. In Fig. 2.3 we display the density summed over $|\mathrm{b}| < 10^\circ$, where the feature behind the bar is visible in the model fitted using our maximum entropy method. The contribution of the feature behind the bar to the background is visible in the bottom panel of Fig. 2.4 as a bump in the fitted background at $K_s \sim$13.8 mag. When using the updated background, the feature behind the bar is no longer present in the density, as seen in the right panel of Fig. 2.3.

Shown in the top panel of Fig. 2.4 is the fitted background for a $1^\circ \times 1^\circ$ box around $(l,b) = (0.9^\circ, -6.1^\circ)$, where we can see that the fitted background is only slightly deviating from the prior background. In the bottom panel, the background fitted in a $1^\circ \times 1^\circ$ box around $(l,b) = (0.9^\circ, 3.1^\circ)$ fits the data well in the shaded regions. However, the background needs to deviate significantly from the prior background at $K_s > 14.7$ mag, where the data may have residual extinction and completeness issues. In the unshaded region, apart from the added feature behind the bar, the background closely follows the shape of the prior solution. The background also smoothly trends back to passing through the data in the shaded regions.

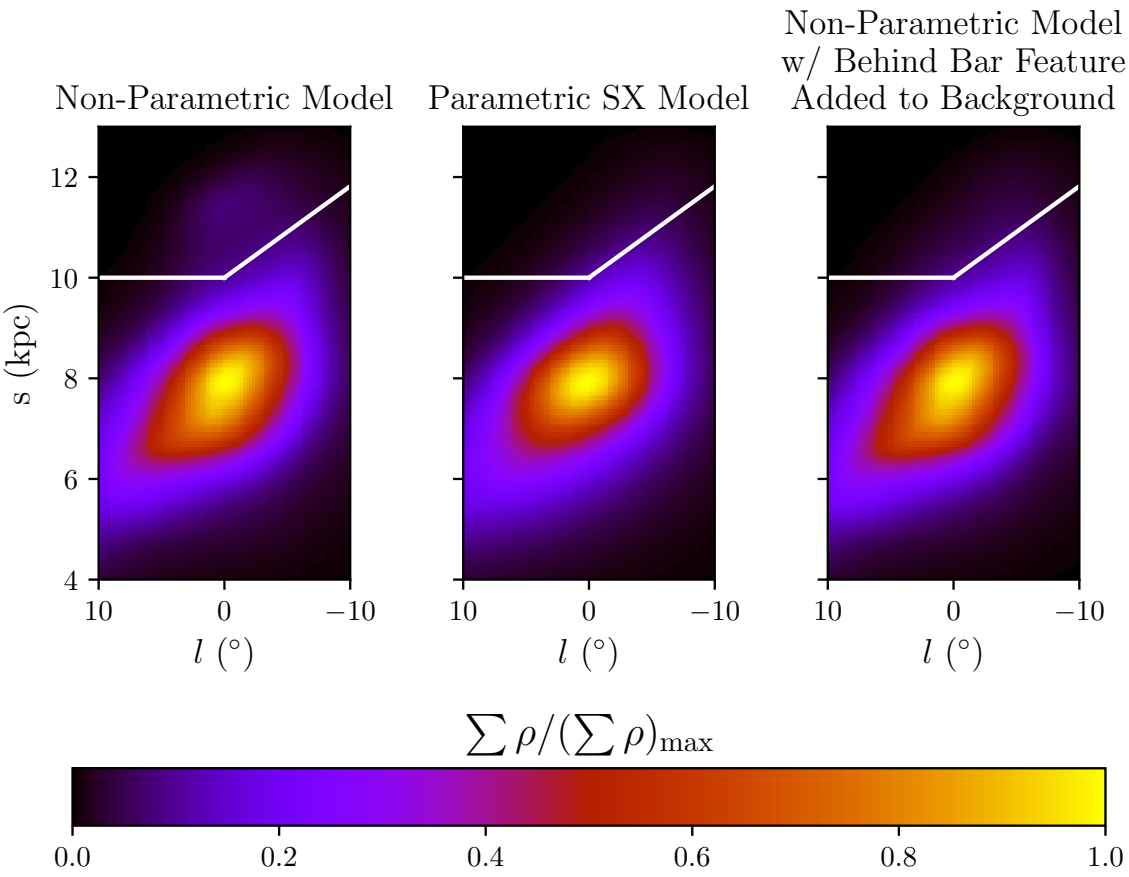

Fig. 2.3 Apparent structure behind the bar in the VVV data, visible in the left panel, was added to the background of our model. We remove any density which is significantly greater than the fitted parametric model (middle panel) and at distances greater than indicated by the white line. In these figures, the density has been summed in the range $|b| < 10°$.

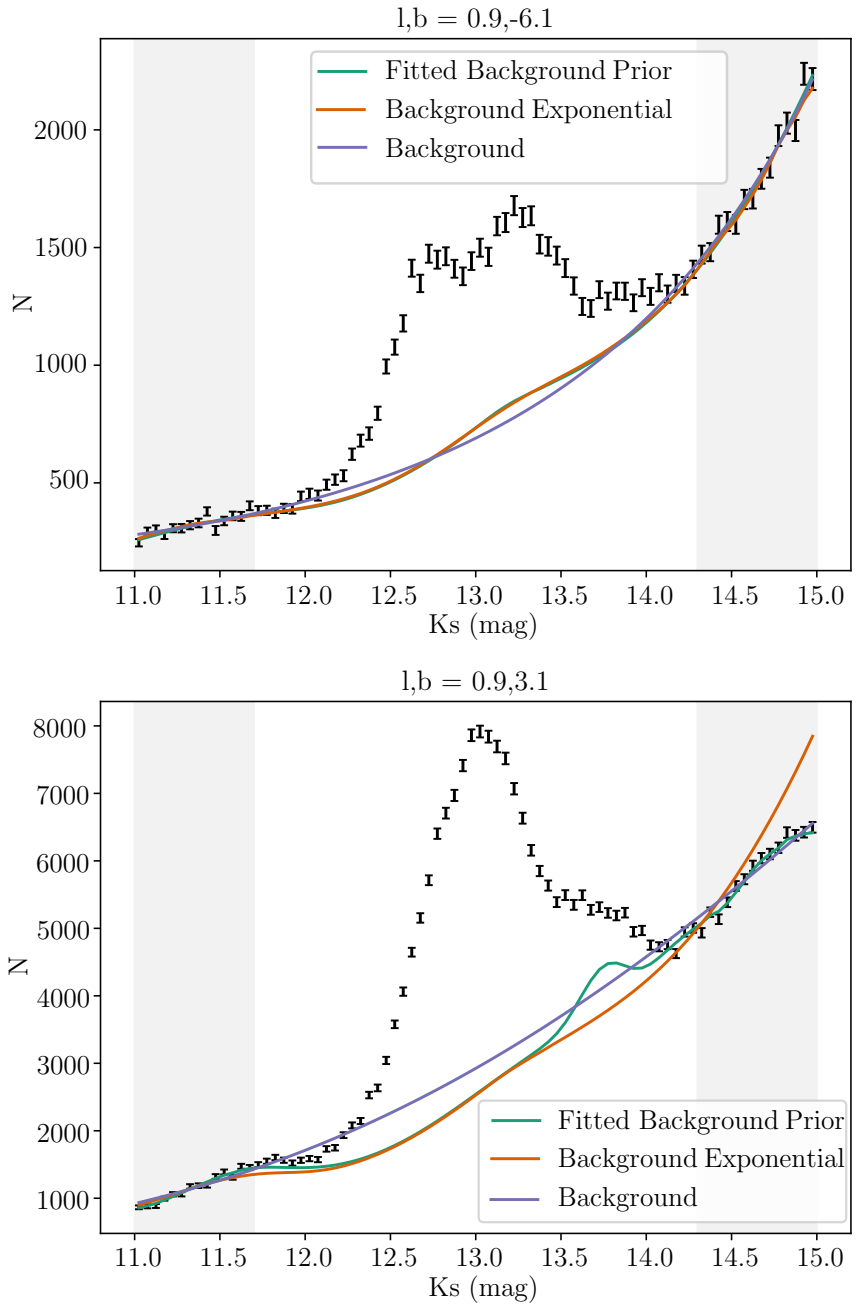

Fig. 2.4 Demonstration of the maximum entropy background fitting in two $1^\circ \times 1^\circ$ regions. The background has been fitted in the grey shaded regions using the maximum entropy method. The prior background was calculated using the S17 S-model+discs, which has been scaled to match the VVV observations between $11.0 < K_s < 11.5$ mag. The bump in the bottom panel "fitted background" at $K_s \sim 13.8$ mag is from a feature behind the bar, see text in Subsection 2.2.4 for more details. The exponential background is described in Section 2.5.8.

2.2.5 Maximum Entropy Deconvolution

Our maximum entropy method provides a non-parametric estimate of the stellar density which predicts the binned star counts of a stellar catalogue. It maximises the same $\ln \mathcal{L}$ as Eq. 2.7, except that B is replaced with the total expected star counts (N) and q is replaced by κ which is the ratio between the bulge density model and a prior estimation of the density such as a parametric bulge model like that of Section 2.2.7:

$$\kappa \equiv \frac{\rho}{\rho_{\text{prior}}}. \tag{2.10}$$

Also, as we are estimating ρ on a grid of (s,l,b), we need a separate sum for the regularisation terms in contrast to Eq. 2.7 where we could use one sum as we estimated the background (B) on a (K_s,l,b) grid. This gives

$$\begin{aligned}
\ln \mathcal{L} = & \sum_{\{i,j,k\}\in\{K_s,l,b\}} \left(n_{i,j,k} \ln N_{i,j,k} - N_{i,j,k}\right) \\
& - \sum_{\{h,j,k\}\in\{s,l,b\}} \Big[\lambda \left(1 - \kappa_{h,j,k} + \kappa_{h,j,k} \ln \kappa_{h,j,k}\right) \\
& + \eta_s \left(\ln \rho_{h-1,j,k} + \ln \rho_{h+1,j,k} - 2 \ln \rho_{h,j,k}\right)^2 /2 \\
& + \eta_l \left(\ln \rho_{h,j-1,k} + \ln \rho_{h,j+1,k} - 2 \ln \rho_{h,j,k}\right)^2 /2 \\
& + \eta_b \left(\ln \rho_{h,j,k-1} + \ln \rho_{h,j,k+1} - 2 \ln \rho_{h,j,k}\right)^2 /2 \Big] .
\end{aligned} \tag{2.11}$$

Including the maximum entropy term in the likelihood discourages the modelled density from over-fitting to regions of the data that are dominated by noise, where it will instead favour the smooth prior density. In practice this is important in the regions where the background makes up a significant part of the model (K_s near 12.0 and 14.0), where the density should be tending towards zero. Addition of the smoothness terms discourages spurious high frequency variations in the modelled density by minimising curvature in the logarithm of the density. The smoothness term also has the added benefit of inpainting the density in lines-of-sight which have been masked. For Eq. 2.11, we set $\lambda = 0$ in masked regions so as they are only affected by the smoothness term and the values of the model at the edge of the mask.

2.2.6 An Analytic Likelihood Gradient Formulation

We derived an analytic gradient form of our full likelihood to enable a computationally feasible optimisation with the number of parameters we are using. The analytic gradients

of $\ln\mathcal{L}$ were determined as follows. We take ρ to be a field, in the mathematical sense, over (s,l,b) so that a single density value, $\rho_\delta = \rho(s,l,b) = \rho_{h,j,k}$ where $\{h',j',k'\} \in \{s,l,b\}$. Each of the ρ_δ represents a free parameter in our model. The gradient of $\ln\mathcal{L}$ with respect to ρ_δ is then

$$\frac{\partial}{\partial\rho_\delta}\ln\mathcal{L} = \frac{\partial}{\partial\rho_\delta}\ln\mathcal{L}_\mathrm{P} + \frac{\partial}{\partial\rho_\delta}\ln\mathcal{L}_\mathrm{MEM} + \frac{\partial}{\partial\rho_\delta}\ln\mathcal{L}_\mathrm{smooth} \tag{2.12}$$

where $\ln\mathcal{L}_\mathrm{P}$ is the Poisson log-likelihood, $\ln\mathcal{L}_\mathrm{MEM}$ is the maximum entropy penalty term and $\ln\mathcal{L}_\mathrm{smooth}$ is the smoothness penalty term. The gradient of the Poisson term is then

$$\frac{\partial}{\partial\rho_\delta}\ln\mathcal{L}_\mathrm{P} = \sum_{\{i,j,k\}\in\{K_s,l,b\}}\left(\frac{n_{i,j,k}}{N_{i,j,k}} - 1\right)\left(\frac{\partial N}{\partial\rho_\delta}\right)_{i,j,k} \tag{2.13}$$

where the derivative of the model, N, is determined by differentiating Eq. (2.4) with respect to ρ_δ so that

$$\left(\frac{\partial N}{\partial\rho_\delta}\right)_{i,j,k} = \Delta\Omega\Delta K_s\left(\int_4^{13}\frac{\partial\rho}{\partial\rho_\delta}\Phi\left(K_s - 5\log s - 10\right)s^2\,\mathrm{d}s\right)_{i,j,k}. \tag{2.14}$$

The integral above can be approximated by the midpoint rule:

$$\left(\frac{\partial N}{\partial\rho_\delta}\right)_{i,j,k} = \Delta\Omega\Delta K_s\Delta s\left(\sum_{h\in s}\left(\frac{\partial\rho}{\partial\rho_\delta}\right)_{h,j,k}\Phi_{h,i,j,k}s_h^2\right)_{i,j,k} \tag{2.15}$$

Where $\Phi_{h,i,j,k}$ is the discretised version of the luminosity function which needs an index for s, K_s, l, and b. Since ρ_δ is single value at $(h,j,k) = (h',j',k')$ in the field ρ, then $\frac{\partial\rho}{\partial\rho_\delta} = \delta_{hh'}\delta_{jj'}\delta_{kk'}$, where the δ here are the Kronecker delta. Substituting this into Eq. (2.15) and simplifying gives

$$\left(\frac{\partial N}{\partial\rho_\delta}\right)_{i,j,k} = \Delta\Omega\Delta K_s\Delta s\,\delta_{jj'}\delta_{kk'}\Phi_{h',i,j,k}s_{h'}^2\,. \tag{2.16}$$

Substituting Eq. (2.16) into Eq. (2.13) gives the final form of the Poisson component of the gradient as

$$\frac{\partial}{\partial\rho_\delta}\ln\mathcal{L}_\mathrm{P} = \Delta\Omega\Delta K_s\Delta s\sum_{i\in K_s}\left(\frac{n_{i,j',k'}}{N_{i,j',k'}} - 1\right)\Phi_{h',i,j',k'}s_{h'}^2. \tag{2.17}$$

The gradient for the Poisson component is equal to zero when $n = N$, so that the log-likelihood has an extremum when the model, N, and the data, n, are equal.

The gradient of the maximum entropy penalty was determined by taking the derivative of Eq. (2.5) with respect to ρ_δ and applying the chain rule

$$\frac{\partial}{\partial \rho_\delta} \ln \mathcal{L}_{\mathrm{MEM}} = \frac{\partial}{\partial \kappa} \left(-\lambda \sum_{\{h,j,k\} \in \{s,l,b\}} \left(1 - \kappa_{i,j,k} + \kappa_{i,j,k} \ln \kappa_{i,j,k}\right) \right) \frac{\partial \kappa}{\partial \rho_\delta} \tag{2.18}$$

where $\kappa = \frac{\rho}{\rho_{\mathrm{prior}}}$ is the ratio between the density field and a smooth prior estimate, ρ_{prior}. Evaluating the derivative in Eq. (2.18) and substituting in $\frac{\partial \kappa}{\partial \rho_\delta} = \frac{1}{(\rho_{\mathrm{prior}})_\delta}$ gives

$$\frac{\partial}{\partial \rho_\delta} \ln \mathcal{L}_{\mathrm{MEM}} = -\frac{\lambda}{(\rho_{\mathrm{prior}})_\delta} \ln \left[\frac{\rho_\delta}{(\rho_{\mathrm{prior}})_\delta} \right], \tag{2.19}$$

which equals zero (thus giving the extremum) when $\rho_\delta = (\rho_{\mathrm{prior}})_\delta$. It follows from this equation that

$$\left. \frac{\partial^2}{\partial \kappa_\delta^2} \ln \mathcal{L}_{\mathrm{MEM}} \right|_{\kappa_\delta = 1} = -\lambda. \tag{2.20}$$

We can then evaluate the expected deviation from the prior using the standard Gaussian approximation for estimating errors in maximum likelihood:

$$\sigma_{\mathrm{MEM}} \equiv \sigma_\kappa = \left(-\left. \frac{\partial^2}{\partial \rho_\delta^2} \ln \mathcal{L}_{\mathrm{MEM}} \right|_{\rho_\delta = (\rho_{\mathrm{prior}})_\delta} \right)^{-1/2} = \frac{1}{\sqrt{\lambda}} \tag{2.21}$$

The gradient of the smoothing term was obtained by direct differentiation of the last three lines of Eq. (2.11) so that

$$\begin{aligned}
\frac{\partial}{\partial \rho_\delta} \ln \mathcal{L}_{\mathrm{smooth}} = & \\
& -\frac{\eta_s}{\rho_\delta} \left[\left(\ln \rho_{h'-2,j',k'} - 4 \ln \rho_{h'-1,j',k'} + 6 \ln \rho_{h',j',k'} \; -4 \ln \rho_{h'+1,j',k'} + \ln \rho_{h'+2,j',k'} \right) \right] \\
& -\frac{\eta_l}{\rho_\delta} \left[\left(\ln \rho_{h',j'-2,k'} - 4 \ln \rho_{h',j'-1,k'} + 6 \ln \rho_{h',j',k'} \; -4 \ln \rho_{h',j'+1,k'} + \ln \rho_{h',j'+2,k'} \right) \right] \\
& -\frac{\eta_b}{\rho_\delta} \left[\left(\ln \rho_{h',j',k'-2} - 4 \ln \rho_{h',j',k'-1} + 6 \ln \rho_{h',j',k'} \; -4 \ln \rho_{h',j',k'+1} + \ln \rho_{h',j',k'+2} \right) \right]
\end{aligned} \tag{2.22}$$

It is easy to check by substitution that this equation is equal to zero when $\rho_{h,j,k}$ is an exponential function of the form:

$$\rho_{h,j,k} = A \exp(A_h h + A_j j + A_k k) \tag{2.23}$$

where A, A_h, A_j, and A_k are constants. Similarly to the MEM case, it follows from differentiating Eq. (2.22) and evaluating the result using (2.23) that the relative deviation from an exponential function is given by:

$$\sigma_{\text{curvature}} \equiv \frac{\sigma_\rho}{\rho_\delta} = \frac{1}{\sqrt{6\eta}}. \tag{2.24}$$

2.2.7 Parametric Model of the X-Bulge

In light of the X-shape apparent in the eight-fold symmetrised WG13 style deconvolution, we considered a closed form parametric base case that allows for an X-arm perturbation. We characterise its potential pathologies in fitting to data and simulations. The parametric density models fitted in this section are used as prior estimates for the density (ρ_{prior}) with the maximum entropy deconvolution in Section 2.4. Our base case parametric-model fit was subsequently applied in a template fitting analysis of the Fermi GCE for comparison with our base non-parametric model result (see Section 3.5).

Triaxial models of the barred galaxies have been used by Athanassoula et al. (1990) in the extragalactic context, and for the Milky Way by Dwek et al. (1995) and Freudenreich (1998). We selected the S-model, which proved successful for bulge modelling in Freudenreich (1998) and S17, as our base distribution. Inspired by the X-bulge parametric form of López-Corredoira (2016), we perturb the S-model with a X-like shape. We use a right-handed, Galactic centre origin, Cartesian grid (X,Y,Z) aligned with the bulge axes of symmetry. The coordinates are chosen so that the X-axis lies along the major axis of the bulge and the Z-axis points towards the north Galactic pole. We refer to the arms of the X-bulge as the X-arms but these are not necessarily aligned with our X coordinate. The perturbation shape was freed in X and Y to accommodate non-circular X-arm shapes. The X-arms in this model part linearly along the bar-aligned Z-axis with gradient C. We also allowed the density of the X-arms to trail off as an exponential of a power-law with exponent n rather than assuming an exponential or Gaussian distribution. We label this parametric form the SX model, with its components defined as follows:

$$\rho_{\text{SX}}(X,Y,Z) = \rho_0 \text{sech}^2(r_1) \tag{2.25}$$

$$\times [1 + A \times (\exp(-r_2^n) + \exp(-r_3^n))],$$

$$r_1^{c_\parallel} = \left[\left(\frac{|X|}{x_0} \right)^{c_\perp} + \left(\frac{|Y|}{y_0} \right)^{c_\perp} \right]^{\frac{c_\parallel}{c_\perp}} + \left(\frac{|Z|}{z_0} \right)^{c_\parallel} \quad ,$$

$$r_2 = \left[\left(\frac{|X - CZ|}{x_1} \right)^2 + \left(\frac{|Y|}{y_1} \right)^2 \right]^{\frac{1}{2}},$$

$$r_3 = \left[\left(\frac{|X + CZ|}{x_1} \right)^2 + \left(\frac{|Y|}{y_1} \right)^2 \right]^{\frac{1}{2}}$$

using a generalised ellipsoid distribution for the bulge and a simple ellipsoidal X-shape aligned with the bulge that tapers off with the the same Z distribution. The parameters $\vartheta = (\rho_0, A, n, x_0, y_0, z_0, c_\perp, c_\parallel, C, x_1, y_1)$ all need to be fit to the data. We used this parametric fit as a prior (ρ_{prior}) for the maximum entropy non-parametric fit which did not enforce eight-fold symmetry. Eq. 2.25 will provide us with an intermediary model between the S and non-parametric models in the Fermi template fitting analysis to gauge the correlation between an improved VVV fit and an improved gamma-ray distribution fit. If the GCE is tracing a bulge and there are no additional unexpected features, we might expect that a model that increasingly traces the morphological features of the bulge will improve the fit.

Investigating the parting rate of the X-arms by fitting a power-law rather than the simple $X \pm CZ$ form, we found the split was still well approximated as a linear function. To avoid convergence issues from excessive parameters, the RC split was left in the linear form.

A tapering of the density at cylindrical radii greater than a cutoff radius, R_c, was applied to the density distribution via $\exp(-2(R - R_c)^2)$ with R_c fixed to 4.5 kpc in all fits, following the preferred choice in S17. We also fit the deviation from an 8 kpc distance from the Sun to the Galactic centre so that the new distance is $8\ \text{kpc} + \Delta R_0$. Additionally, we fitted α which is the angle between the bulge major axis and the line connecting the Sun to the Galactic centre.

We optimise our parametric models for parameter set ϑ using the SciPy BFGS routine[1], minimising the Poisson likelihood statistic:

$$\ln \mathcal{L} = \sum_{\{i,j,k\} \in \{K_s, l, b\}} \left(n_{i,j,k} \ln N_{i,j,k} - N_{i,j,k} \right) + \text{constant} \tag{2.26}$$

[1] SciPy 1.3.0 https://www.scipy.org/

where N_i is the corresponding model, obtained by integrating the equation of stellar statistics (Eq. 2.4) for parametric density ρ_{SX}. Our best fit likelihoods and uncertainties are listed in our tables of results (Tables 2.4, 2.5, and 2.6). The uncertainties are derived from the corresponding square root of diagonal elements of the inverse Hessian matrix produced by this routine. The SX model fit was initialised by randomly picking a starting point somewhere between qualitatively different boundaries that produce physically possible densities for the X perturbation parameters and choosing the initial S parameters from within 10% of the best fit values from the S-model.

2.3 Testing The Deconvolution Against A Simulation

We constructed a simulated Milky Way population comprised of a thin disc, thick disc, and a bulge, as is modelled in S17. To generate the synthetic population, we used

$$N(K_s,l,b) = \Delta\Omega\Delta K_s \times \sum_i \int_0^\infty \rho_i(s,l,b)\,\Phi_i(K_s - 5\log s - 10)\,s^2 ds \tag{2.27}$$

where ρ is the density and Φ is the luminosity function and the sum is over the three model components, to predict the combined star counts in each (K_s,l,b) voxel. We then simulated a population of stars by drawing a Poisson random value from the binned simulation model. We simulated the thick and thin discs using the Besançon galaxy model (Robin et al., 2003). The Besançon disc models were constructed as follows (summarising the parametric definitions in the process): The thin discs are segmented into seven sub-populations by age, from 0-10 Gyr. All these components are modelled as cylindrically symmetric holed ellipsoids using the Einasto (1979) density law,

$$\rho_{\rm thin}(R,Z_{\rm cyl}) = \rho_0 \left[\exp\left(-\sqrt{0.25 + \left(\frac{a}{h_t}\right)^2} \right) - \exp\left(-\sqrt{0.25 + \left(\frac{a}{h_h}\right)^2} \right) \right] \tag{2.28}$$

with

$$a^2 = R^2 + \left(\frac{Z_{\rm cyl}}{\varepsilon}\right)^2 \tag{2.29}$$

where R and $Z_{\rm cyl}$ are cylindrical Galactocentric co-ordinates in kpc, h_t is the scale length of the disc and h_h is the scale length of the hole in kpc. ε is the axis ratio of the ellipsoid, which had been fitted for each population age. We generated a luminosity

function for each sub-population of the thin disc, similarly to Section 2.2.2, assuming a broken power-law IMF

$$\xi(m) = \begin{cases} m^{-1.6}, & m \leq 1M_{\odot} \\ m^{-3.0}, & m > 1M_{\odot} \end{cases} \tag{2.30}$$

Within each sub-population, the metallicity takes a Gaussian distribution in [Fe/H] with mean and dispersion as given in Table 2.2. We used mass-absolute magnitude relations from the PARSEC+COLIBRI isochrones (Marigo et al., 2017).

The formation history of the thick disc was assumed to be a single burst event 12 Gyrs ago. The density profile used is distributed exponentially radially, where vertically the density is parabolic near the plane, transitioning to exponential further away from the plane

$$\rho_{\text{thick}}(R,Z) = \begin{cases} \rho_0 \exp\left(-\frac{R-R_{\odot}}{h_T}\right)\left[1-\frac{Z^2}{h_z}\frac{1}{\zeta(2+\zeta/h_Z)}\right] & Z \leq \zeta \\ \rho_0 \exp\left(-\frac{R-R_{\odot}}{h_T}-\frac{|Z-Z_{\odot}|}{h_Z}\right)\frac{2\exp(\zeta/h_Z)}{1+\zeta/h_Z} & Z > \zeta \end{cases} \tag{2.31}$$

where $(R_{\odot}, Z_{\odot}) = (8.0 \text{ kpc}, 15 \text{ pc})$ is the position of the Sun. Parameter h_T is the radial scale length, h_Z is the vertical scale height and ζ is the height where the density transitions from parabolic to exponential. The IMF for the thick disc is a simple power-law

$$\xi(m) = m^{-0.22}. \tag{2.32}$$

Both the thick and thin discs were modelled as having a warp and a flare,

$$Z_{\text{warp}} = \gamma_{\text{warp}}(R - R_{\text{warp}})\cos(\phi - \phi_{\text{warp}}) \tag{2.33}$$

where the density in Eq. (2.28) and Eq. (2.31) at Z, is instead evaluated at $Z + Z_{\text{warp}}$ when $R > R_{\text{warp}}$; ϕ_{warp} is the direction in which the warp is maximum. The flare was modelled by linearly increasing the scale height by

$$h_{\text{flare}} = \gamma_{\text{flare}}(R - R_{\text{flare}}) \tag{2.34}$$

when $R > R_{\text{flare}}$. We used the same parameters for the flare and warp as Robin et al. (2003); $\gamma_{\text{warp}} = 0.18$, $R_{\text{warp}} = 0.98R_{\odot}$, $\phi_{\text{warp}} = 90.0°$, $\gamma_{\text{flare}} = 0.0054$ and $R_{\text{flare}} = 1.12R_{\odot}$. These parameters for the density and metallicity distributions of each disc component are summarised in Table 2.2.

Table 2.2 Density and metallicity parameters for the Besançon thick and thin discs.

Component	Age	$h_{t/T}$	ε/h_Z	h_h	$\mu_{[Fe/H]}$	$\sigma_{[Fe/H]}$
Thin Disc	0.0-0.15	5.00	0.0140	3.00	-0.01	0.12
	0.15-1	2.53	0.0268	1.32	-0.03	0.12
	1-2	2.53	0.0375	1.32	-0.03	0.10
	2-3	2.53	0.0551	1.32	-0.01	0.11
	3-5	2.53	0.0696	1.32	-0.07	0.18
	5-7	2.53	0.0785	1.32	-0.14	0.17
	7-10	2.53	0.0791	1.32	-0.37	0.20
Thick Disc	12	2.36	0.535	-	-0.78	0.3

Table 2.3 Density distribution parameters for the bulge component used for our simulation. The second row gives the total number of stars in the unmasked regions of the simulation in the range $12 < K_s < 14$. In cylindrical coordinates, centred at the maximum density of the bulge, the Sun in located at $(R_\odot, Z_\odot) = (8.0 \text{ kpc}, 15.0 \text{ pc})$.

x_0(kpc)	y_0(kpc)	z_0(kpc)	$\alpha(^\circ)$	$c_\parallel$	$c_\perp$
1.61	0.69	0.48	19.16	2.50	1.86

$N_{\text{thin}}(\times 10^6)$	$N_{\text{thick}}(\times 10^6)$	$N_{\text{bulge}}(\times 10^6)$
1.35	1.87	17.04

The S-bulge model we used is the X-armless reduction of Eq. 2.25 and takes the form:

$$\rho_{SX}(X,Y,Z) = \rho_0 \text{sech}^2(r_s). \tag{2.35}$$

With a generalised ellipsoidal radial distribution r_s defined as:

$$r_s^{c_\parallel} = \left[\left(\frac{|X|}{x_0} \right)^{c_\perp} + \left(\frac{|Y|}{y_0} \right)^{c_\perp} \right]^{\frac{c_\parallel}{c_\perp}} + \left(\frac{|Z|}{z_0} \right)^{c_\parallel} .$$

The simulation parameters used for this model are listed in Table 2.3.

The normalisations we used for each of the three components were multiplied by the same constant chosen so that the total number of stars in the unmasked region and in $12 < K_s < 14$ matches the number of stars in the VVV PSF catalogue. The luminosity function we used for the bulge in the simulation is the same as the one we used in our fitting procedure to the VVV data.

To choose the values of the regularisation parameters we tested a range of choices in a $1^\circ \times 1^\circ$ region centred on $(l,b) = (0.9, -6.1)$. The test region was subdivided

into our usual voxel size of ($0.05\,\mathrm{mag} \times 0.2^\circ \times 0.2^\circ$). For this test, we did not want to use a prior that was too close to the true value, so we used the base SX (Eq. 2.25) model that had been fitted to the VVV data. We first fixed the maximum entropy regularisation parameter, λ from Eq. 2.11, to zero and applied our maximum entropy deconvolution method with a range of smoothing regularisations, η. We repeated this for $\eta = 0$ and a range of λ values. In Fig. 2.5 the deconvolved density for all choices of η follow the general shape of the true density. Small values of η give spurious oscillatory deviations from the true density, which decrease in amplitude as η increases. There is not a significant difference in the predicted star counts between the choices of η. For $\lambda \geq 1.0$, the predicted star counts deviate significantly from the simulation, which is also seen in the deconvolved density where it overestimates at distances less than 6 kpc, and underestimates from 6-8 kpc. This is because the prior density is not a good estimate of the true density for the current case. When $\lambda = 0.01$, the deconvolved density is scattered around the simulated density, and the predicted star counts are over-fitting. The results of this test suggested that a small value of λ and a large value of η would give the most accurate density deconvolution. Therefore, we used a value of $\lambda = 0.01$ and $\eta = 100 - 1000$. For the background modelling, a simulation is not needed to determine an optimal set of regularisation parameters, as the effectiveness can be determined by directly comparing to the data. Also, the prior background from the S17 model gives a good description of the background. This means we expect less deviation from the prior and so a larger value of λ can be used. The regularisation parameters used for the background determination are presented in Table 2.1.

The distribution of curvature in log-density (Eq. 2.6) for the simulated bulge in Fig. 2.6 is strictly negative. It is broadest in b, second broadest in l and narrowest in s. The ℓ_2-norm regularisation gives a minimum penalty to the likelihood when the log of the fitted density has zero curvature. We chose η_s, η_l, and η_b such that the overall curvature penalty term in Eq. 2.11 was of similar magnitude. From the distributions of the curvature term in Fig. 2.6 we chose the regularisation parameters used for fitting the simulated population as listed in Table 2.1.

We applied the maximum entropy deconvolution process to the simulated star counts, first by fitting the background including the feature behind the bar, then by fitting a parametric density model to determine a prior density estimation for the full 3-D density deconvolution. The parameters of the fitted prior density are presented in Table 2.6, labelled case A. The maximisation of the $\ln \mathcal{L}$ in Eq. 2.11 and $\ln \mathcal{L}$ in

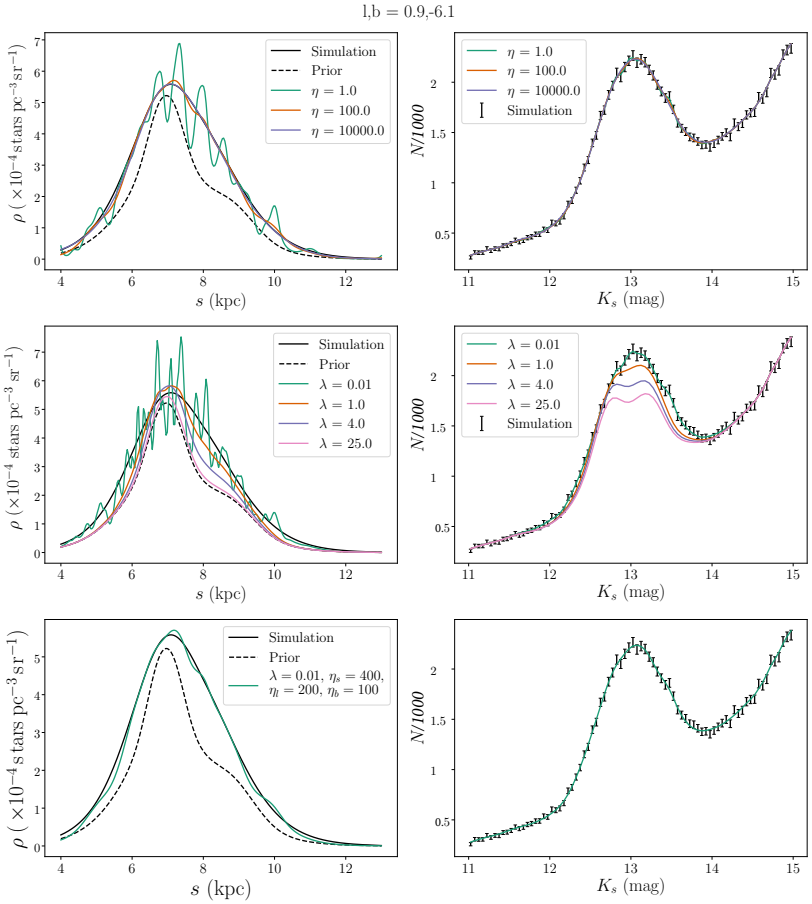

Fig. 2.5 Testing the choice of regularisation parameters. We perform our maximum entropy deconvolution to a $1^\circ \times 1^\circ$ region of our simulated population, centred on $(l,b) = (0.9, -6.1)$. In the top panels, the maximum entropy regularisation is set to zero, and a range spatial smoothness parameter values are tested. The middle panels have the spatial smoothness regularisation set to zero, and a range of maximum entropy regularisation values are tested. The bottom panels have the regularisation parameters used in our final analysis. The left panels show the deconvolved density compared to the true density in the simulation, the right show the model star counts (N) compared to the simulated population (n). For small values of η, the deconvolved density has many spurious features, which get smaller in amplitude as η is increased. The predicted star counts is not significantly sensitive to the choice of η in the range tested here. For all $\lambda \geq 1.0$, the predicted star counts do not match the simulation, where it is clear that the prior density distribution is not a good estimate of the true density.

Eq. 2.7 were both performed using the python implementation PYLBFGS[2] of the Limited Memory Broyden-Fletcher-Goldfarb-Shanno (L-BFGS) algorithm.

The density was modelled non-parametrically on a (257, 100, 50) grid of (s,l,b), in the range $4<(s/\mathrm{kpc})<13$, $-10^\circ<b<0^\circ$ and $-10^\circ<l<10^\circ$, for a total of 1.285×10^6 free parameters. The grid spacing is $(\Delta s,\Delta l,\Delta b)$ = (35 pc, 0.2°, 0.2°). To make the optimisation of so many parameters feasible, we evaluated the gradients of $\ln\mathcal{L}$ in Eq. 2.11 and $\ln\mathcal{L}$ in Eq. 2.7 analytically via the formulation in Section 2.2.6. We assumed symmetry about the Galactic mid-plane so that we could reliably extend our non-parametric density model to latitudes $b>5^\circ$, where there are no observations in the VVV sample. Making the mirror symmetry assumption forced us to position the Sun in the Galactic mid-plane ($Z_\odot=0$ kpc). We fixed the reconstructed density just outside the region of interest to the prior density by setting $\lambda=1$ in those regions. This meant that the smoothness regularisation forced the reconstructed density to smoothly transition to the parametric prior density at $|l|>10^\circ$ and $|b|>10^\circ$.

Shown in the top panel of Fig. 2.7 is the background fitted to the simulation. From the deconvolution of the VVV data shown in Fig. 2.7, we can see the simulated population lacks a splitting of the RC peak that is present in the VVV observations case shown in Fig. 2.8. In Fig. 2.9 we compare the 3-D deconvolved density to the density used in simulating the population. The deconvolved density using the maximum entropy method compares well to the density used in our simulation, even inside of the masked regions where there is no data influencing the deconvolution. However, the reconstruction displays some discrepancy at around $s=4$ kpc. Note that this is due to the low star counts in the bulge at this radius which makes an accurate reconstruction difficult. Note that Fig. 2.9 correctly does not show the X-bulge morphology that is seen in the VVV data which is displayed in Fig. 2.10.

2.4 Deconvolution of VVV

In this section, we discuss how we applied our maximum entropy deconvolution method to the VVV data sample for our base model which we label as case A. We used a fit of the parametric SX model as the prior density distribution and the values for the regularisation parameters in Table 2.1. The background was fitted using the maximum entropy method of Section 2.2.4. In Fig. 2.8 we present a breakdown of the maximum

[2] https://github.com/dedupeio/pylbfgs, version 0.2.0.12

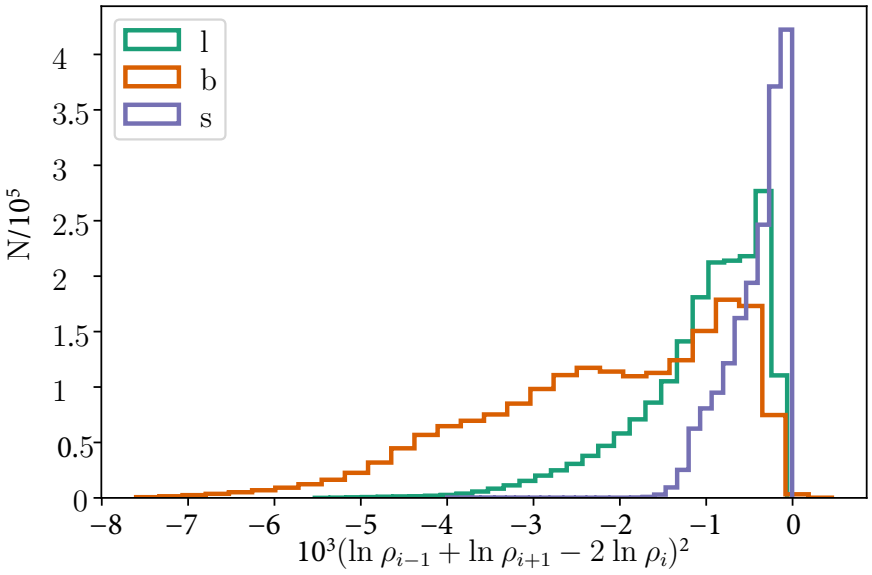

Fig. 2.6 Distributions of the curvature in log-density (Eq. 2.6) along respective density model coordinates of the simulated bulge.

entropy deconvolution model components along a single line-of-sight through the region the photometric split clump has been observed.

Displayed in Fig. 2.11 is a comparison between the predicted star counts by our maximum entropy deconvolution, the fitted parametric model we used as the prior, and the VVV data. For compactness, we show every tenth magnitude bin. At $K_s < 12$ and $K_s > 14$ the RC+RGBB stars contribute negligibly to the total star counts, so both the parametric model and maximum entropy deconvolution are dominated by the background. By construction, these regions are well described by the background model, though perhaps there is slight over-fitting in the $K_s = 14.975$ bin. The non-parametric model reproduced the data well and has smaller deviations in comparison to the parametric model, especially notable in the $K_s = 12.525$ bin at $l = 5°$ where the X-bulge is prominent. The assumption of symmetry about the Galactic mid-plane seems to be reasonable, as there is no visible bias in fitting to the mirrored contours above and below the plane.

The deconvolved density and the fitted parametric density, for fixed latitude bins, are shown in Fig. 2.10. For compactness, only 9 of the 50 bins are displayed and only for $b < 0°$, as the density is symmetric about b. Unlike the simulated bulge shown in Fig. 2.9, the density from deconvolution of the VVV data shows the arms of the X-bulge, first noticeable at $b = -8.7°$ for $(l,s) = (4.7°, 6.6 \text{ kpc})$ and $(l,s) = (-3.3°, 9 \text{ kpc})$. As

latitude decreases, the arms get closer until they merge at $b = -2.7°$. The maximum density at $b = -2.7°$, where the arms merge, is at longitude $l = -0.7°$. The maximum density of the X-bulge arms in the parametric model do not align with the maximum density in the non-parametric model, which is also evident in the star counts. Cartesian versions of the reconstructed bulge from the VVV data and the simulation are shown in the first columns of Figures 2.12 and 2.13 respectively.

2.5 Systematic Tests

In order to gain a better understanding of the robustness of our results we test systematics based on the following:

- Adding the feature behind the bar to the background (case B).
- The VVV data mask (case J).
- The determination of the background component (case C).
- The semi-analytic luminosity function (case D and I).
- The metallicity distribution (case E).
- The position of the Sun (case F, G, H, I).
- The deconvolution method used.

We tested the significance of these assumptions by systematically changing one, then repeating the maximum entropy deconvolution, including the background fitting and parametric prior density model fitting (except the deconvolution method systematic). We also repeated the deconvolution with the new assumptions on the simulated population.

The results of fitting the SX model to data and simulations are listed in Tables 2.5 and 2.6, and are plotted in Figures 2.14, 2.15, and 2.16. Except where specified, the parametric model has been fitted twice, following the prescription of the deconvolution method in Section 2.2, in which the feature behind the bar is subsumed into the background. By fitting to the S-model simulation generated by the parameters in Table 2.3, we hoped to gauge the impact on the likelihood of different background and parametric model cases used in bulge modelling. Note that in the simulation, we chose $Z_\odot = 15$ pc. As can be seen in Fig. 2.15, the range of fitted model parameters is much

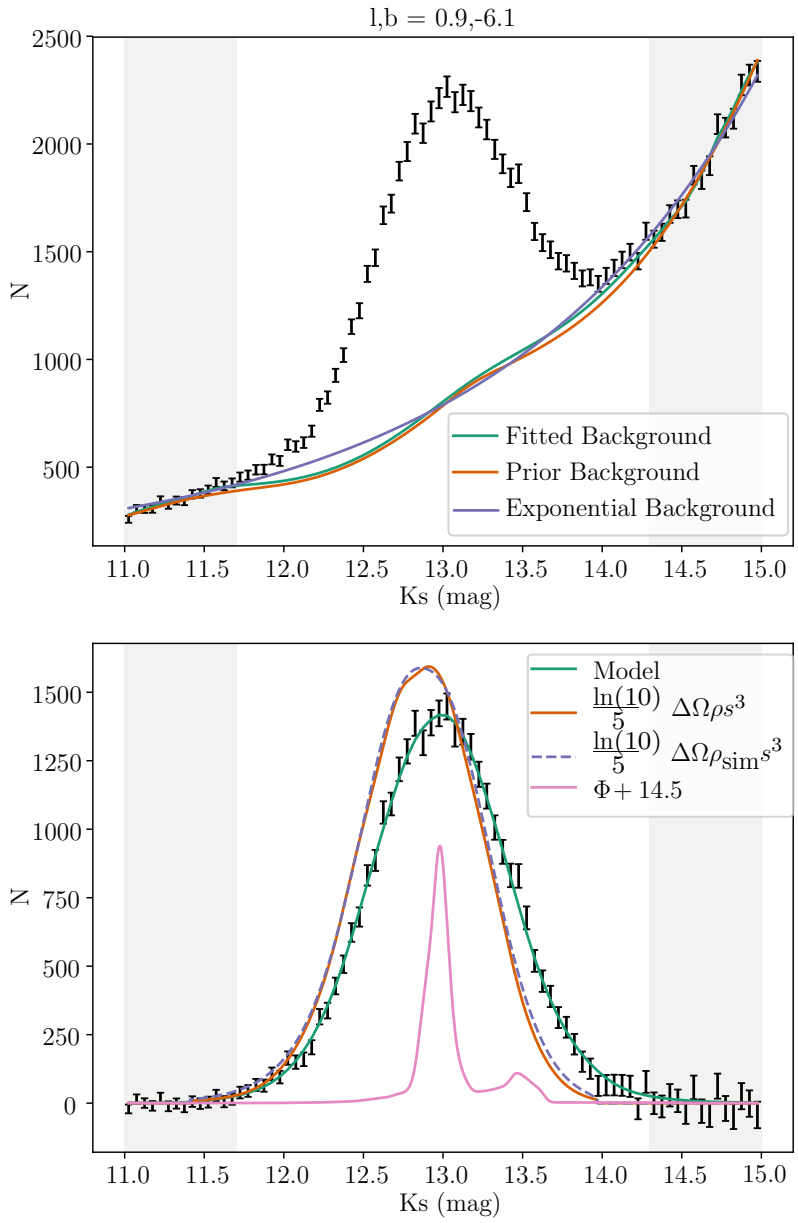

Fig. 2.7 Demonstration of the maximum entropy deconvolution method to a simulated population for a $1^\circ \times 1^\circ$ region. *Top*: The background has been fitted in the grey shaded regions using the maximum entropy method. The prior background is the background of the model used to generate the simulation. *Bottom*: Maximum entropy deconvolution of the line-of-sight star count distribution. Shown in green is the predicted number of RC star counts from the convolution of the fitted density (orange) and assumed luminosity function (pink). The density used to produce the simulation is shown as a dashed purple line. The luminosity function has been scaled and shifted for display, where 14.5 is the distance modulus added to the absolute magnitudes, M_{Ks}.

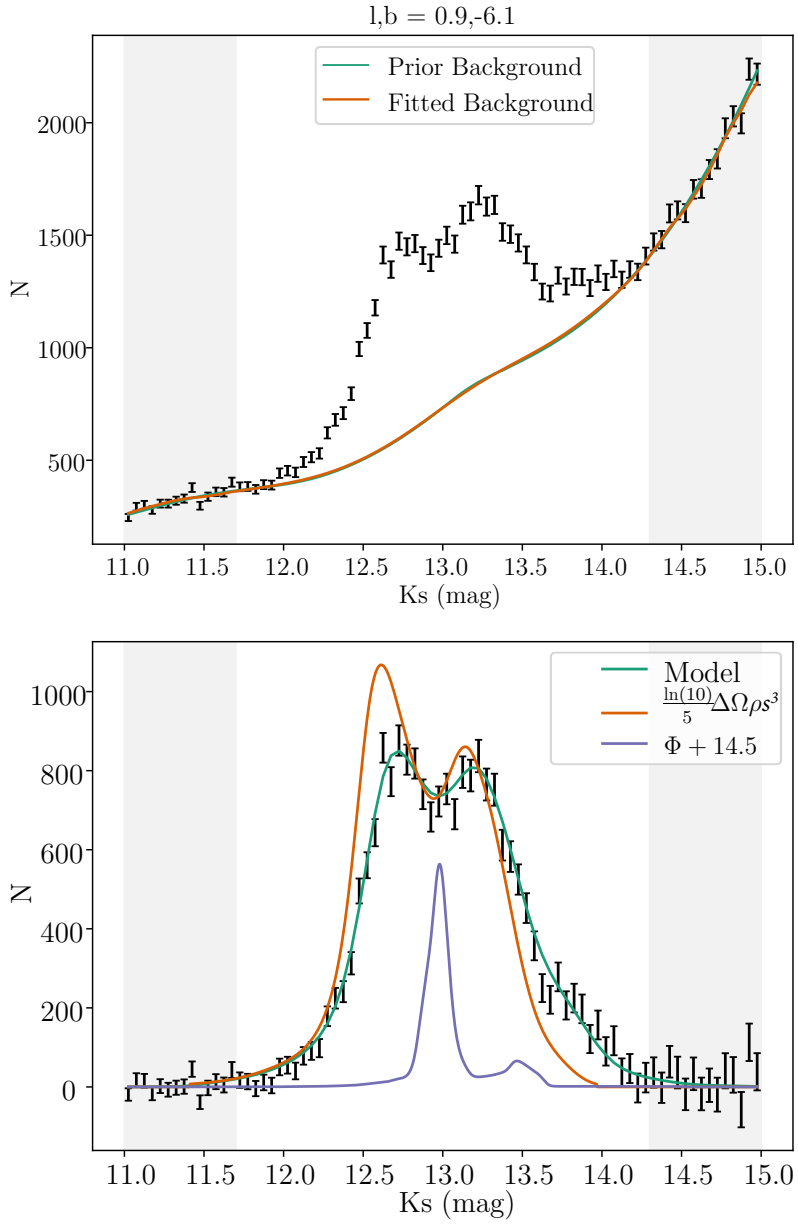

Fig. 2.8 Demonstration of the maximum entropy deconvolution method in a $1^\circ \times 1^\circ$ (5×5 pixels) region. *Top*: The background has been fitted in the grey shaded regions using the maximum entropy method. The prior background was calculated using the S17 S-model+discs, which has been scaled to match the VVV observations between $11.0 < K_s < 11.5$. *Bottom*: Maximum entropy deconvolution of the line-of-sight background subtracted star count distribution. Shown in green is the predicted number of RC star counts from the convolution of the fitted density (orange) and assumed luminosity function (purple). The luminosity function has been scaled for display.

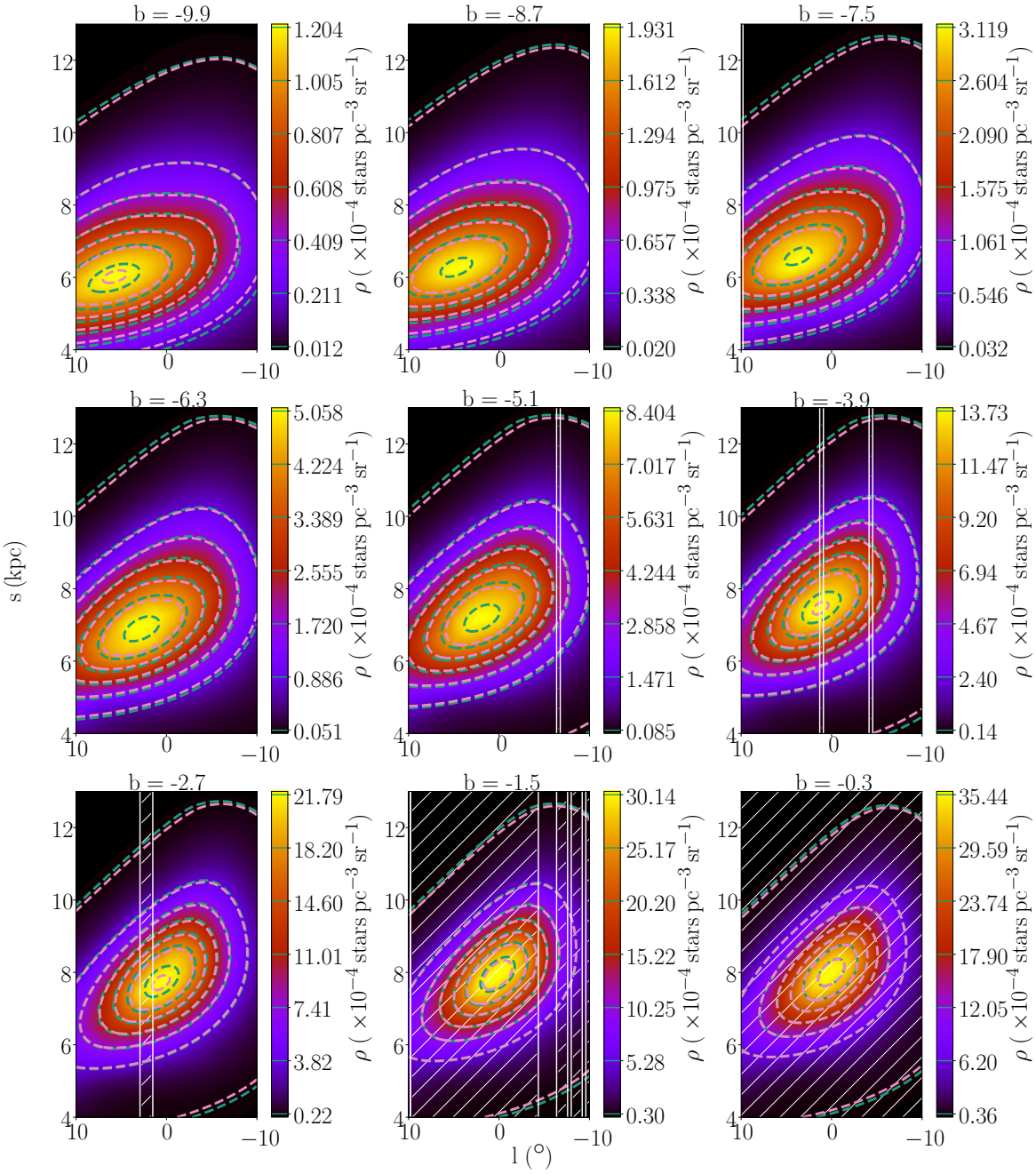

Fig. 2.9 Deconvolved RC+RGBB star density using the maximum entropy method for a simulated 10 Gyr S-model. White hatched regions were masked during the analysis, and were inpainted naturally as part of the deconvolution. Green dashed contours show the true density used in simulating the S-bulge. Pink show the parametric SX model used as the prior density.

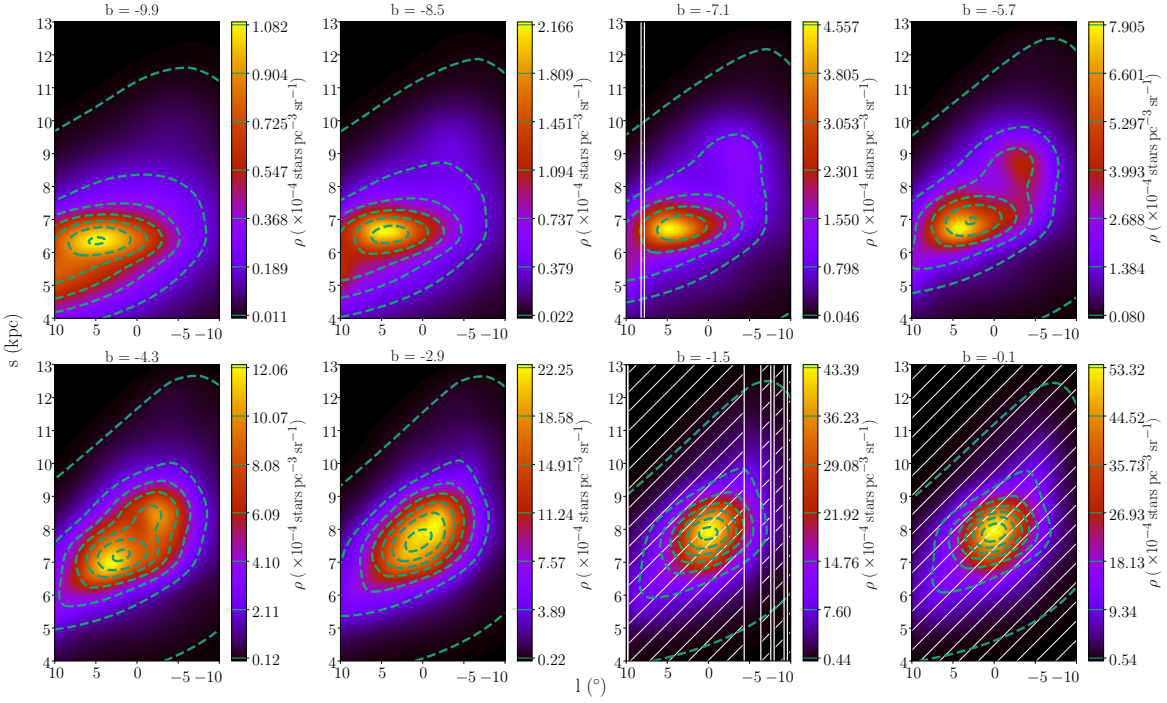

Fig. 2.10 Deconvolved RC+RGBB star density using the maximum entropy method. White hatched regions were masked during the analysis, and were inpainted as part of the deconvolution. The prior density model is shown in green dashed contours.

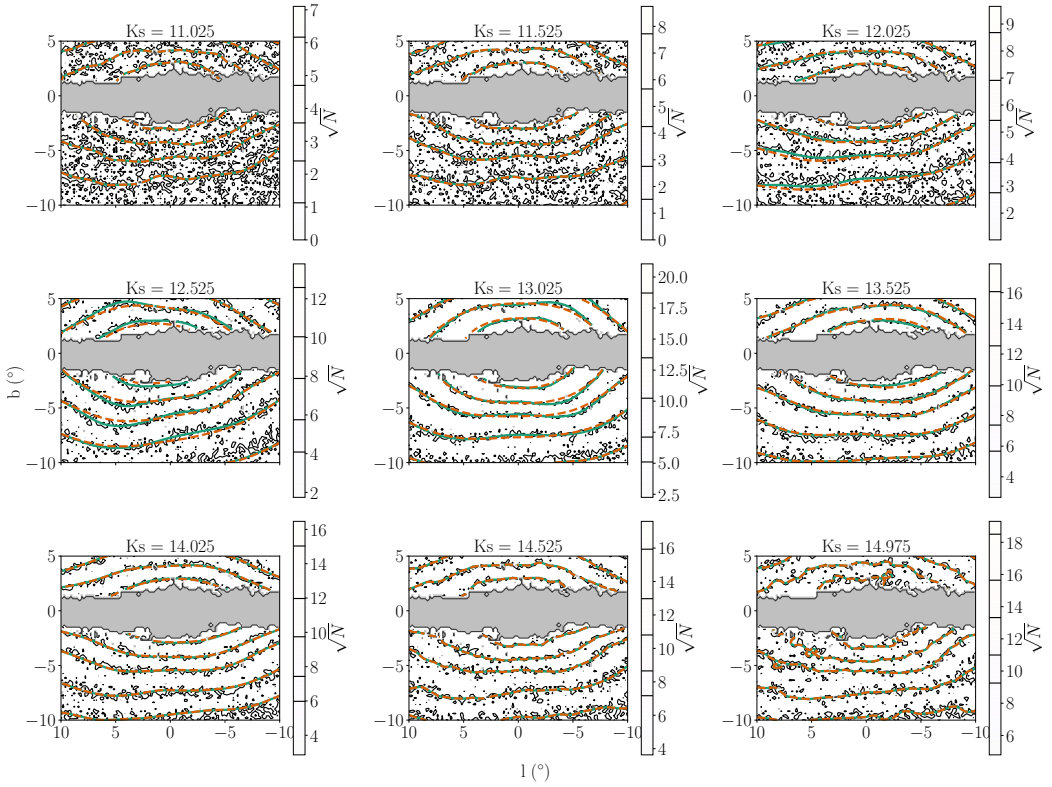

Fig. 2.11 Predicted star counts for our maximum entropy deconvolution method. Black contours show the VVV star counts, where the levels of the contours are indicated by black lines on the colour bar. Green contours show the star counts predicted by the non-parametric model, where the levels match the black contours. The orange dashed line is the parametric model used as the prior. Contours are produced using the same resolution as the data, i.e. $0.2^\circ \times 0.2^\circ$ degree grid with K_s bins of width 0.5 mag.

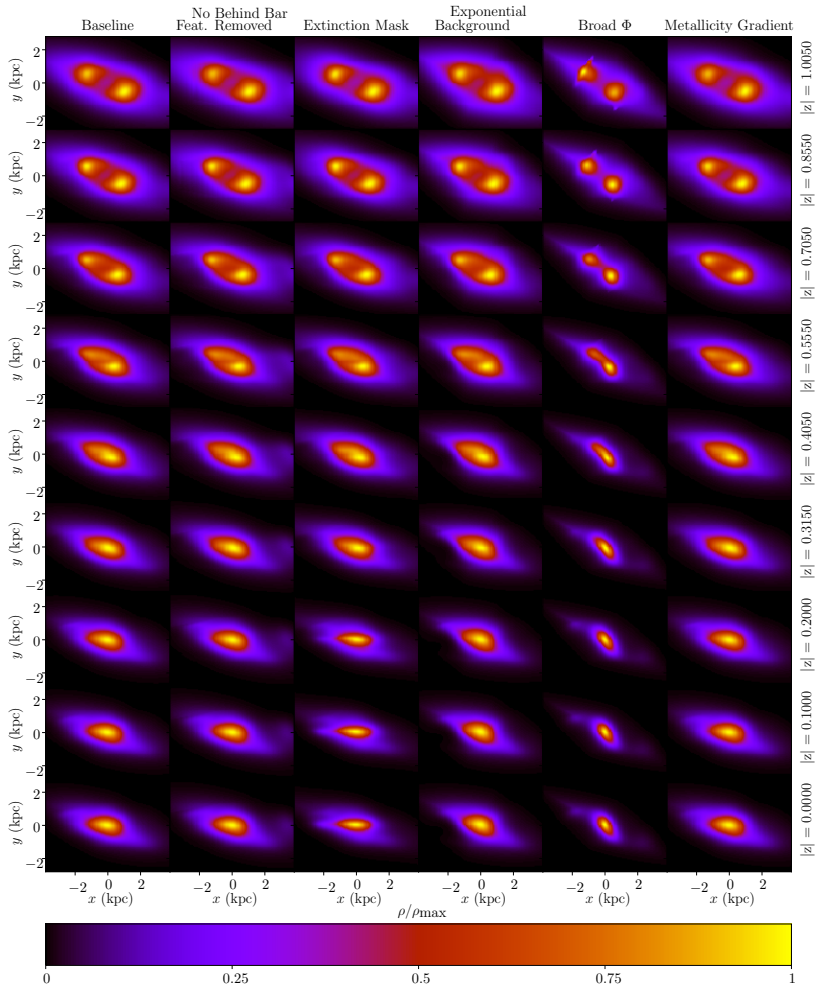

Fig. 2.12 Cartesian projections of the deconstructed density of the VVV RC stars in the bulge, for several systematic test cases. The x axis is aligned with the Sun-Galactic centre line and the z-axis is perpendicular to the Galactic plane and measured in kpc. The Galactic centre is located at the maximum bulge density. The significance of each test case is discussed in the text in Section 2.5

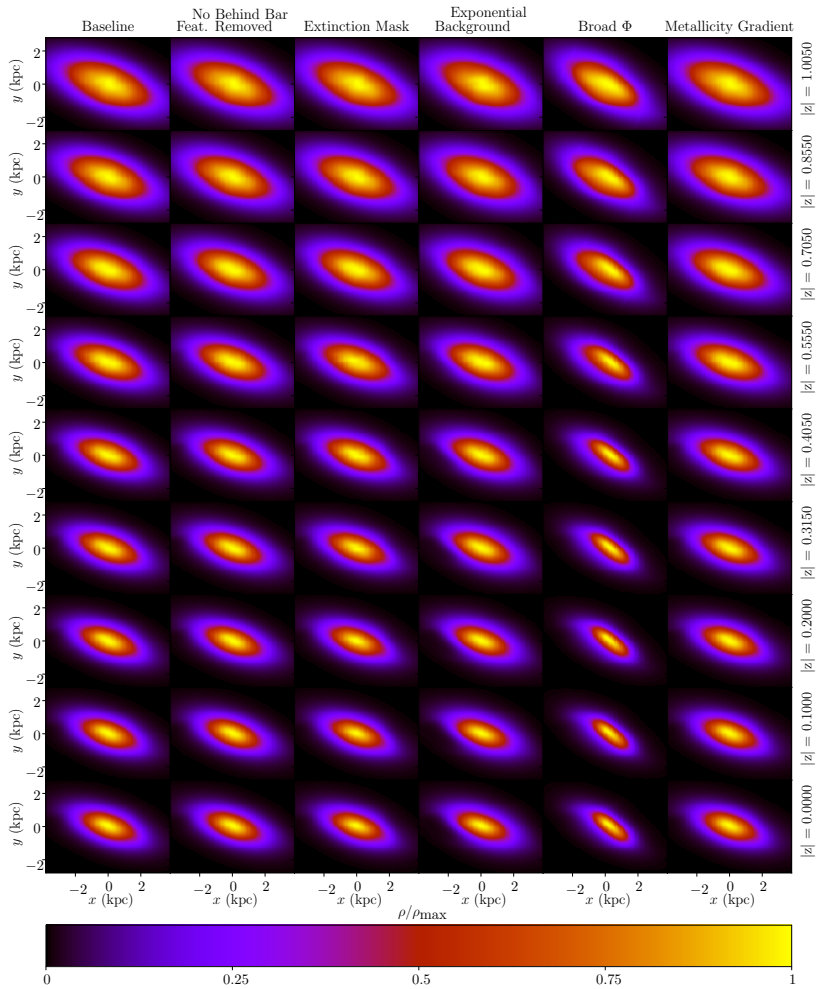

Fig. 2.13 Cartesian projections of the deconstructed density of the simulated bulge population, for several systematic test cases. The x axis is aligned with the Sun-Galactic centre line and the z-axis is perpendicular to the Galactic plane and measured in kpc. Nearly all of the cases give a qualitatively similar density to the base case. However, the exponential background gives densities that are too low at $(x,y) = (-2.5\text{kpc}, 0\text{kpc})$, especially at low latitudes. Also, the broadened luminosity function gives a larger bar angle than the base case. The two exceptions noted here are also seen in the VVV data (Fig. 2.12).

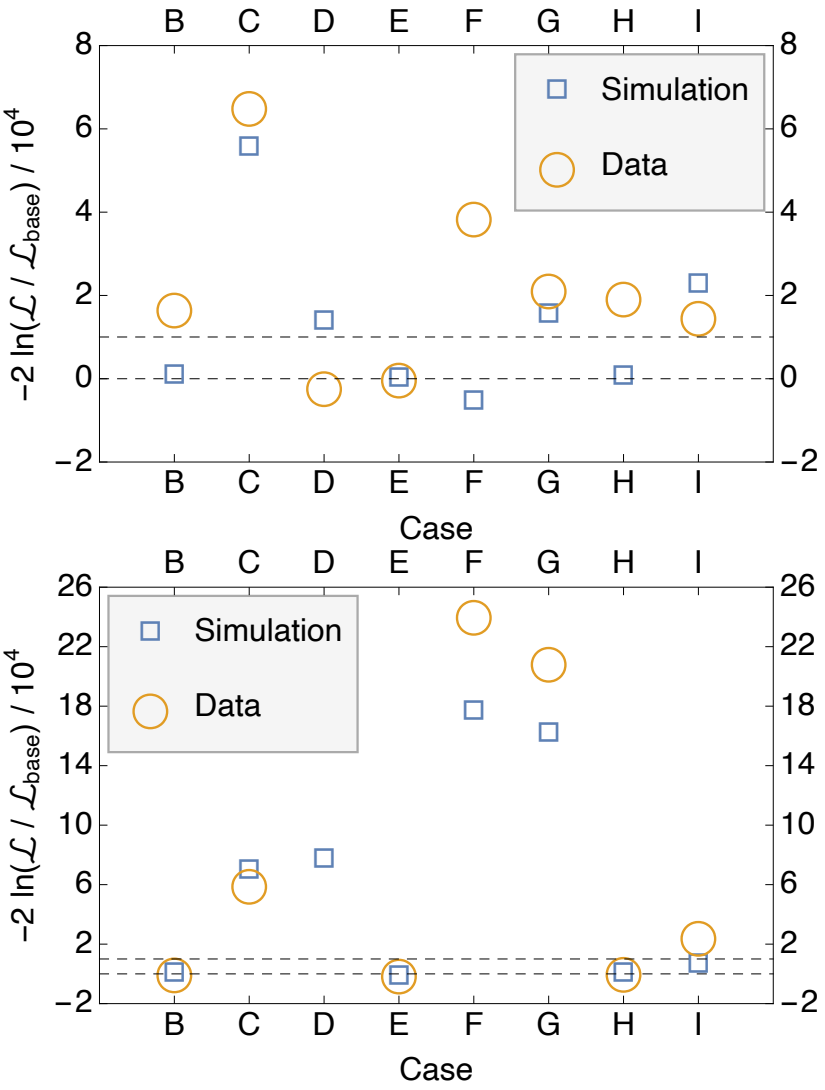

Fig. 2.14 The parametric (top panel) and non-parametric (bottom panel) likelihood ($\mathcal{L}$) for the different cases considered. The base case's non-parametric likelihood is $\mathcal{L}_{\rm base}$. Results are shown for both the simulations and the data. In the simulation case the base case and labelled case are both fit to the simulated data. In the bottom panel, Case D's data symbol is not shown due to its very low likelihood value not being in the range of the plot for the non-parametric fit. See Table 2.4 for numerical values including the one for Case D in the non-parametric fit. The dashed lines are for $\mathrm{TS} = 0$ and the median of the simulations for both the parametric and non-parametric case which is $\mathrm{TS} \approx 10^4$. The cases considered are: no behind-the-bar feature subtraction (B), exponential background (C), broad luminosity function (D), metallicity gradient (E), S-model prior with $Z_\odot = 15$ pc (F), S-model prior and broad luminosity function with $Z_\odot = 15$ pc (G), S-model prior with $Z_\odot = 0$ pc (H), S-model prior with $Z_\odot = 0$ pc with a broad luminosity function (I).

greater than the error bars in Table 2.6. This indicates the main cause of the variation is due to model assumptions rather than statistical error. We used the following test statistic (TS) to compare the different cases:

$$\mathrm{TS} \equiv -2\ln(\mathcal{L}/\mathcal{L}_{\mathrm{base}}) \tag{2.36}$$

As most of the variation between cases was due to systematic error rather than statistical error, we did not use Wilks' theorem (Wilks, 1938) which is also only suited for nested models. This means we cannot associate the TS value with a p-value in the usual way. We can get a rough measure of what a significant TS value is by comparing to the corresponding TS values seen in simulations. The median value of the simulation TSs for the combined top and bottom panels of Fig. 2.14 was $TS \approx 10^4$. We take this as our threshold above which the TS value is regarded to be significant.

2.5.1 Feature Behind the Bar

In both the top and bottom panels of Fig. 2.14, the simulation has a negligible TS when testing against case B which does not account for a feature behind the bar. This is to be expected as this feature was not present in the simulation. In contrast, for the parametric fit (top panel), the data has a high TS for case B. This indicates that the feature behind the bulge is significant. We later analysed this case in more detail, presented in Section 2.7. Also, in Section 2.7 we used a parametric background which then also revealed a feature in front of the bulge. The non-parametric background in this chapter has absorbed most of the feature in front of the bar.

However, in the non-parametric case (bottom panel) we do not find a significant change in our penalised likelihood when not removing the feature behind the bar. This can be seen in the bottom panel of Fig. 2.14 where case B has a TS very close to zero for both the data and simulation. This is to be expected as the flexibility of the non-parametric method can easily incorporate the feature behind the bar as being part of the bulge as seen by comparing column 1 and 2 in Fig. 2.12. While for the simulation, where there should be no feature behind the bar, the corresponding columns are virtually indistinguishable as depicted in Fig. 2.13.

2.5.2 Background Systematics

We changed the background in case C to one that is common in the literature, a second order polynomial in $\log(N)$, described in Section 2.5.8. We have already displayed this

background for a couple of lines-of-sight in Fig. 2.4. At high latitudes (top panel), this background tends to estimate higher counts than the maximum entropy background for $12 < K_s < 12.5$ and estimate fewer counts at $13 < K_s < 14$. At lower latitudes, this background tends to overestimate at all K_s, especially at around $K_s = 12.0$. On the simulation, the exponential background significantly over estimates in the range, $11.7 < K_s < 13.0$, as shown in the top panel of Fig. 2.7. As a result, the density is underestimated on the near side ($x < 0$) of the bulge at low latitudes when using the exponential background rather than the maximum entropy background in both the VVV data (Fig. 2.12) and simulated population (Fig. 2.13).

In Fig. 2.14, for the parametric fit (top panel), the exponential background (case C) has the worst TS both for the data and simulation, out of all of the cases considered in that panel. The TS was also high for both the data and simulation in the non-parametric case as shown in the bottom panel of Fig. 2.14. This provides further evidence that the maximum entropy method is providing a better background than the exponential model approach.

2.5.3 Luminosity Function Systematics

S17 found that the best-fitting luminosity function was significantly broader than the luminosity function they had simulated with GALAXIA (Sharma et al., 2011), using the same isochrones we have used in our analysis. We also tried a similarly broad luminosity function, by convolving our luminosity function (of approximate Gaussian width 0.06 mag) with an additional Gaussian with a standard deviation of 0.24 mag. The density slices in the "Broad Φ" column of Figures 2.12 and 2.13 are consistent with the broadened luminosity function requiring a narrower and more angled bulge. A similar relationship can be seen in Fig. 16 of S17. In the top panel of Fig. 2.14, the SX parametric model with broadened luminosity function (case D) had a slightly improved TS for the data, while it was disfavoured for the simulation. However, this broader luminosity function is not consistent with recent measured intrinsic RC magnitude dispersions in the K_s band of 0.03-0.09 mag (Hall et al., 2019; Chan & Bovy, 2019). Also, in Fig. 2.16, the X-shape parameters, n and x_1, are anomalous for case D. The consequence of this was that the broader luminosity function fit resulted in unnaturally narrow X-arms as depicted in Fig. 2.17. As can be observed in the non-parametric results shown in the bottom panel of Fig. 2.14, the broader luminosity function (case D) provided a high TS for the simulations indicating a bad fit. This is to be expected as the simulations were based on our standard narrower luminosity function. The

TS for the data was so high for the broad luminosity function that we could not accommodate it in Fig. 2.14 without making the range of the plot too great to see any of the other details. This was because the non-parametric model was being heavily penalised for deviating greatly from the prior SX model, which had converged to a physically unnatural solution, shown in the top panel of Fig. 2.17.

Since our prior for the maximum entropy deconvolution was unnatural for the broad luminosity function, we wanted to check if a different prior gave similar results. So we repeated the test, but instead we used an S-model as the prior density, shown in the bottom panel of Fig. 2.17. As can be seen in the top panel of Fig. 2.14, this S-model with a broad luminosity function (case I) was disfavoured by both the data and the simulation for the parametric case. Also, as presented in the bottom panel of Fig. 2.14, case I did have a significant TS for the non-parametric fit in the case of the data. This indicates that from a TS perspective, our non-parametric results disfavour a broad luminosity function.

2.5.4 Metallicity Distribution Systematics

Our base case assumed that the metallicity distribution is constant throughout the bulge. Several spectroscopic studies, e.g. Zoccali et al. (2017) and García Pérez et al. (2018), have observed a vertical metallicity gradient in the bulge, where stars near the Galactic mid-plane are on average more metal rich than stars on the periphery of the bulge. We used the photometric metallicity map generated by the BEAM-II calculator (Gonzalez et al., 2018) to allow the metallicity distribution function in the computation of our semi-analytic luminosity function to have a different mean metallicity for every line-of-sight. The metallicity dispersion was kept fixed at 0.4 for this test. Shown in Fig. 2.18 (top panel) is the metallicity map of Gonzalez et al. (2018), where we have filled the missing values with [Fe/H] = 0.0. From the luminosity functions in the bottom panel of Fig. 2.18, it is clear that the lower metallicity line-of-sight has a fainter RC, and is naturally broader, though the difference in brightness is only 0.03 mag between $b = -9.1$ and $b = -3.1$. Some part of the broadness is from the overlapping of the RC and RGBB, since the RGBB is brighter at lower metallicities. Qualitatively, the density which was fitted using the metallicity gradient is nearly identical to the base case as seen in the last column of Fig. 2.12. The insensitivity to the metallicity gradient can be seen in case E for the bottom and top panel of Fig. 2.14. The TS changes for the metallicity cases are negligible in comparison to the TS changes associated with the other systematics. The E case does appear to have an anomalous x_1 in Fig. 2.16.

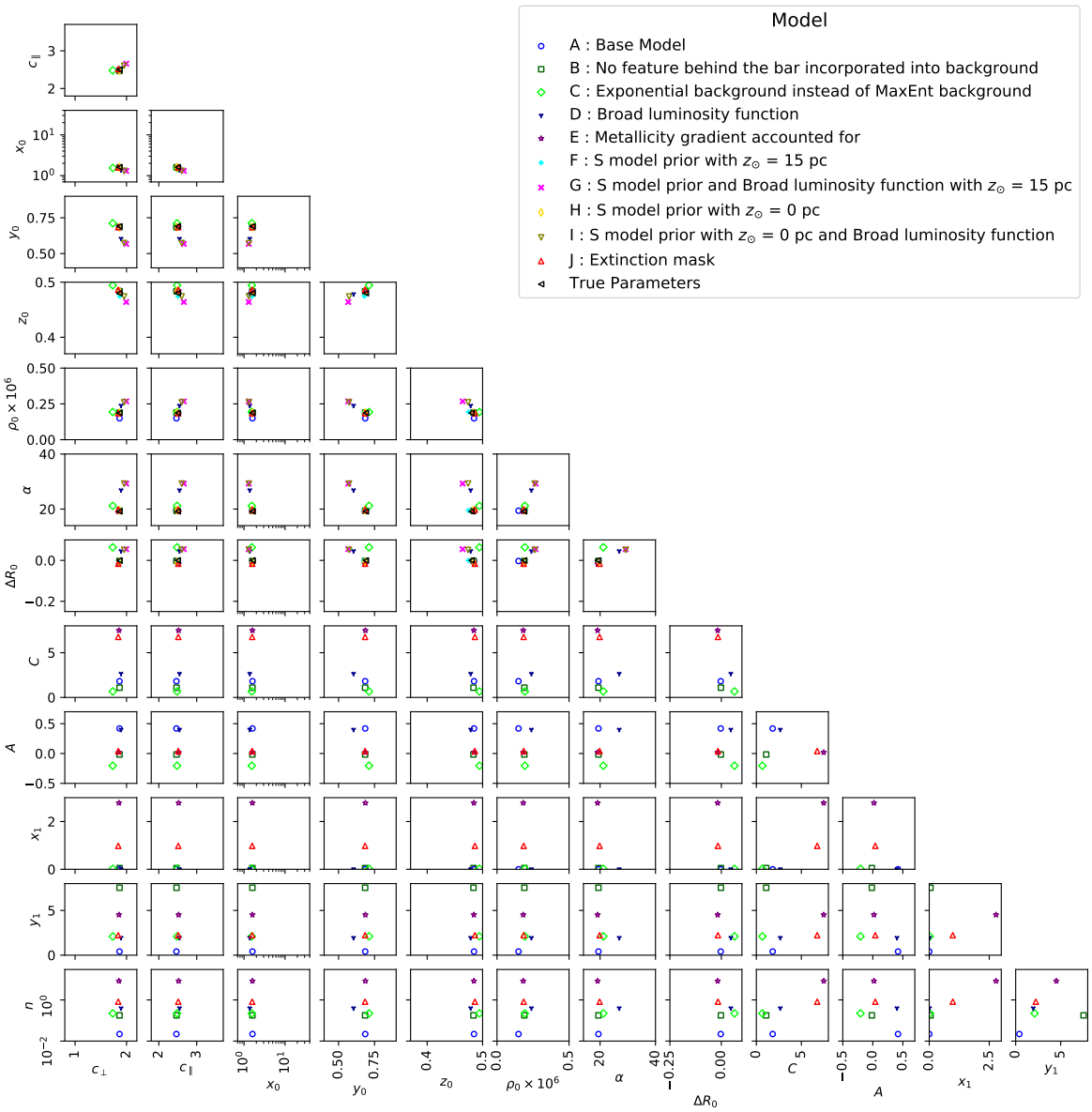

Fig. 2.15 Pair plot of parametric model parameters fitted for the base case and systematics to simulations. See Table 2.6. The n parameter has been plotted on a logarithmic scale.

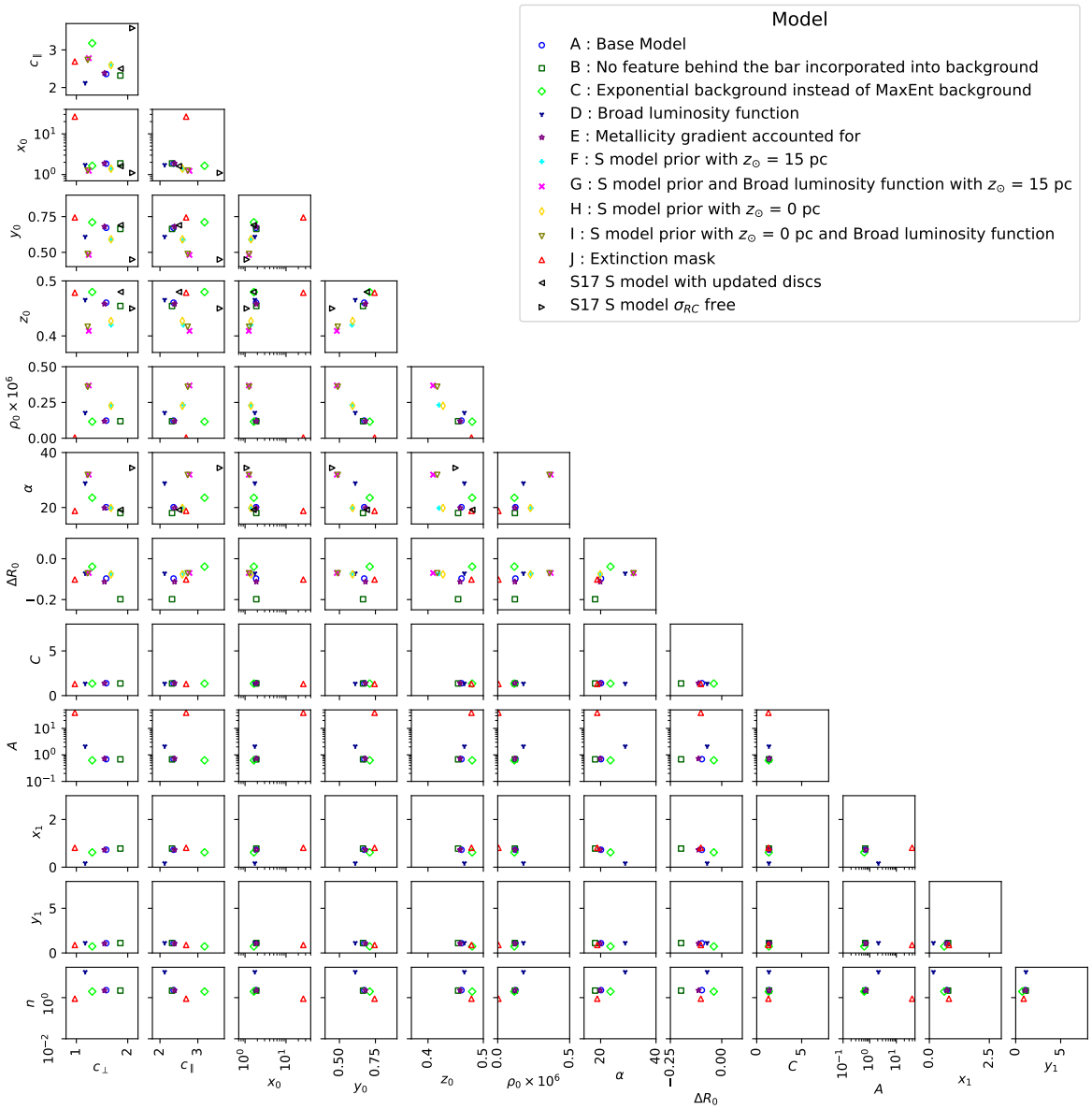

Fig. 2.16 Pair plot of parametric model parameters fitted for the base case and systematics on the VVV data. Note that the axis scaling for parameters x_0, A, and n are logarithmic. See Table 2.5.

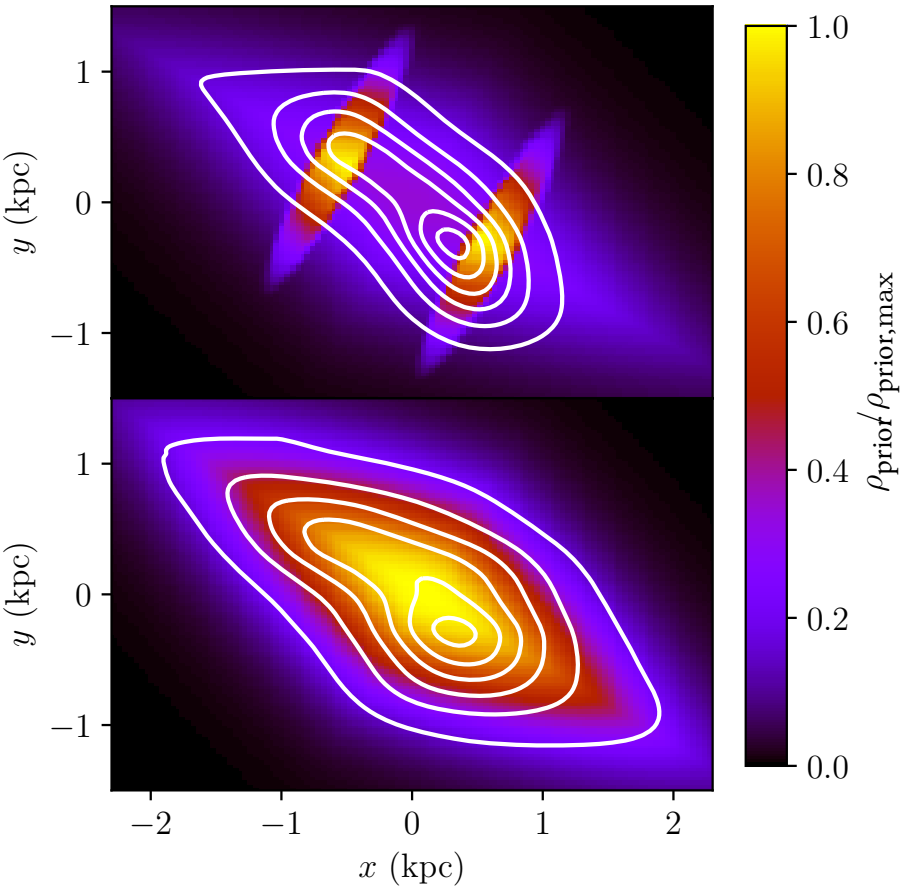

Fig. 2.17 SX (top) and S (bottom) parametric density models at $z = 0.495\,\mathrm{kpc}$, fitted to the VVV data using the 10 Gyr bulge Parsec derived luminosity function which has been convolved with a Gaussian with $\sigma = 0.24$ (case D). They are used as the prior models for a non-parametric fit. The broadened luminosity function has driven the X-component to be unnaturally contrasting to the S component, which necessitates the non-parametric model (white contours) modulate significantly from the prior density. By contrast, the S-model is still largely visible in the non-parametric solution, with the modulated X-bulge arms visible at $x = \pm 0.5$

However, as $A \approx 0$ for the E case, its X-component is negligible. We conclude from this test that the inclusion of a simple unimodal metallicity gradient does not significantly affect our results. A more sophisticated double population model, consistent with spectroscopic observations, is necessary to properly include a metallicity gradient.

2.5.5 Sun Position Systematic

Our simulated population of stars had the Sun located at $Z_\odot = 15$ pc, which is different to the $Z_\odot = 0$ pc assumed in our base model. We tested the significance of this assumption by fitting an S-model with the Sun in the same position as in our simulation (case F). We still assumed symmetry in the maximum entropy density about $b = 0°$. The top panel of Fig. 2.14 shows how parametric case F provided an improved fit to the simulation. This is to be expected as it corresponds with the model used to generate the simulation. In the case of the VVV data, it is harder to interpret the case F result in Fig. 2.14 as we have changed both the position of the Sun and the parametric form of the prior density. The difference between case F and case H is the position of the Sun, where both differ from the base case by having an S-model parametric form. The VVV data TS of case F was significantly larger than case H in the parametric case, however, there was less of a difference when fitting the parametric model to the simulation. This confirms that the VVV data prefers $Z_\odot = 0$ pc when fitting the parametric S-model as seen in the top panel of Fig. 2.14. When comparing the same cases, F and H, for the non-parametric method, case F had a significantly larger TS than case H for both the simulated population and the VVV data. It is hard to interpret this result for the non-parametric model, given that it had an assumed symmetry around the $Z_\odot = 0$ pc plane.

Case H is an S-model with $Z_\odot = 0$ pc. As can be seen from the top panel of Fig. 2.14, for the parametric fit, the data significantly prefers the SX model. Also, for the parametric fit, the F case is very slightly favoured over the SX model for the simulation. This follows in that the F case is of the same form as the model used to generate the simulation. However, case F is even more disfavoured by the data than case H. From this we conclude that, for the parametric fit, the data favours the SX model over the S-model and this conclusion is not affected by reasonable changes in $Z_\odot$.

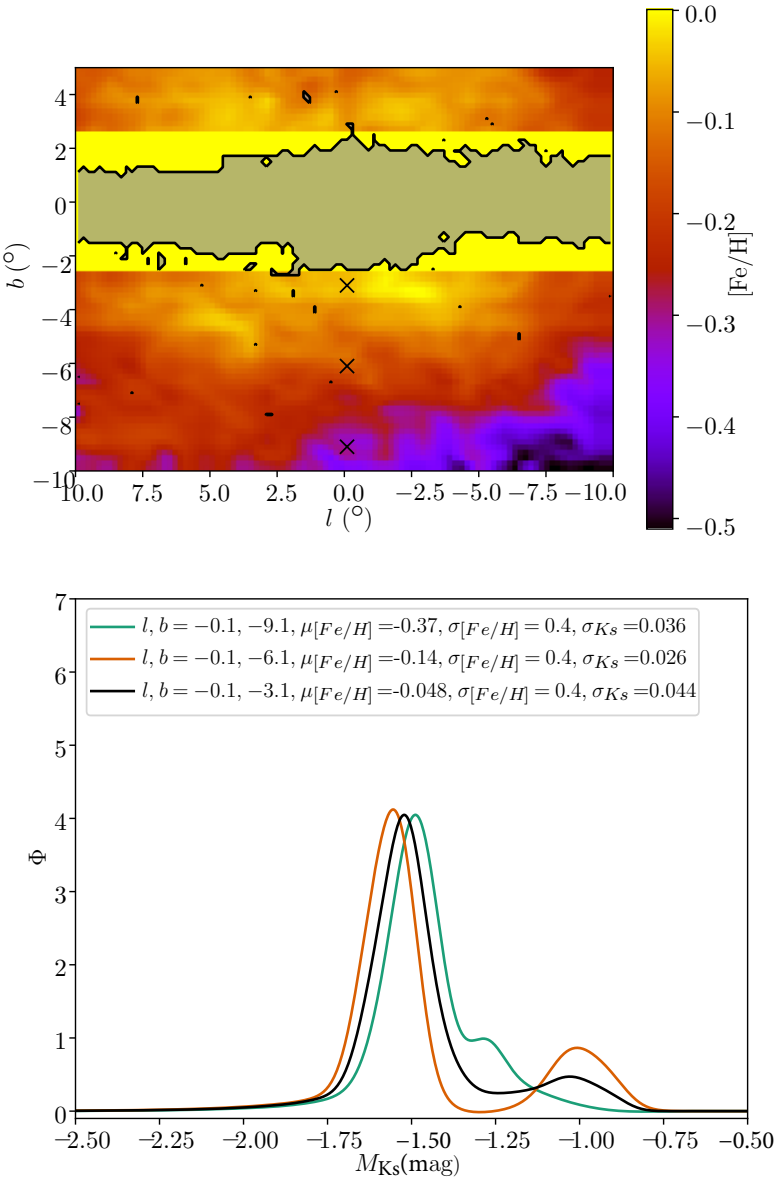

Fig. 2.18 *Top:* Mean photometric metallicity map, [Fe/H] of Gonzalez et al. (2018). Where the map does not have coverage at $|b|< 2.6$ we assume the fiducial value $[Fe/H] = 0.0$. The black crosses indicate the locations of the three luminosity functions plotted in the bottom panel. *Bottom:* The RC+RGBB luminosity functions for a range of fields of view, assuming a metallicity distribution as in the above panel. They have been convolved with a Gaussian with dispersion σ, the photometric uncertainty. In order of increasing metallicity, the mean absolute magnitude of the RC is -1.49 mag, -1.51 mag and -1.52 mag.

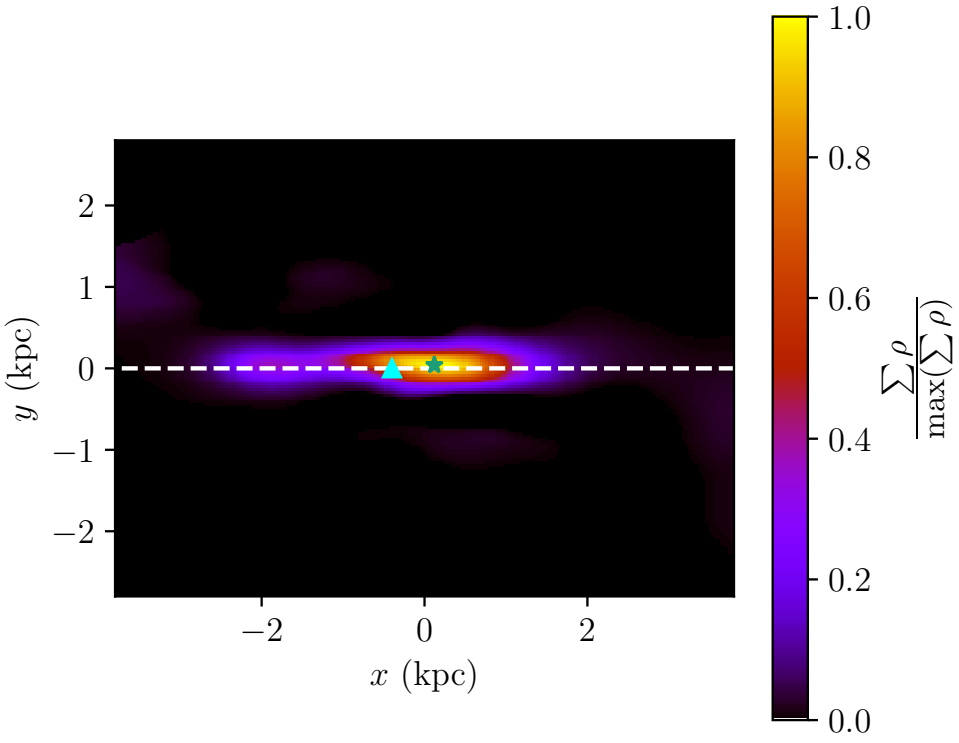

Fig. 2.19 Difference between the deconvolved density using a crowding + extinction-based mask and a extinction only mask in Cartesian co-ordinates where x is aligned with the Sun-Galactic centre line. The density difference has been summed over $|z < 1\,\mathrm{kpc}|$. The white dashed line indicates $l = 0°$. The maximum density of the difference (indicated by a green star) is 150 pc behind the maximum density location of the crowding + extinction-based mask reconstructed bulge. The cyan triangle is at the expected maximum density location for a population which would have an RC 0.1 mag brighter than our PARSEC derived semi-analytic luminosity function, such as a 5 Gyr old population or a more metal rich population.

2.5.6 Mask Systematic

We changed the region in which the data is excluded, from the combined extinction and K_s-band uncertainty boundary case ($\sigma > 0.06$), to a colour excess mask $E(J-K) > 0.9$. This systematic test changes the amount of data used in the analysis, so the likelihood is not comparable to the base case. In Fig. 2.12, the density that is reconstructed with an extinction only mask has a prominent bar-like feature at $|z| < 0.2\,\mathrm{kpc}$, that is pointed nearly directly towards the Sun. Note, that this feature is not seen in the corresponding simulation result of Fig. 2.13. We extracted this feature by subtracting the baseline case. Plotted in Fig. 2.19 is the sum of the density difference for all density with $|z| < 1\,\mathrm{kpc}$. At first glance, this apparent over-density looks similar in structure to the younger, secondary population of bulge stars in S17 (E component of the S+E model). The green star indicates the maximum density of the difference and is located at $(x,y) = (120\,\mathrm{pc}, 90\,\mathrm{pc})$. This is 150 pc behind the centre of the bulge ($(x,y) = (0\,\mathrm{pc}, 0\,\mathrm{pc})$). This suggests that the stars are unlikely to be from a significantly younger or more metal rich population than the rest of the stars in our bulge model, as they would have a brighter RC in the luminosity function than we have modelled. A 5 Gyr old population with a similar metallicity distribution to our fiducial case has an RC which is 0.1 mag brighter, which corresponds to a difference of 400 pc closer at 8 kpc, indicated by the cyan triangle on Fig. 2.19.

We argue based on the reconstructed distance from the Sun, that the apparently over-dense region is not consistent with a different population of stars. Its orientation, which is suspiciously pointed directly towards the Sun, and is distinctly different from the majority of the bulge population also makes it inconsistent with main population of the bulge stars. This was one of our motivations in using the crowding+extinction-based mask over the extinction-only-based mask. A combination of significant crowding and residual extinction deteriorates the quality of the star count catalogues, including the photometric zero-point.

2.5.7 Results Tables for Systematics

The best-fiting likelihood values we obtained for our parametric and non-parametric fits are listed in Table 2.4. The best fit parameter values are listed in Tables 2.5 and 2.6.

Table 2.4 Minimum values of $-2\ln\mathcal{L}$ for the parametric and non-parametric models. The base case (A) values of $(-1.36968, -2.35631, -1.4102015, -2.32068) \times 10^8$ have been subtracted from columns one to four respectively. The non-base cases considered are: no behind-the-bar feature subtraction (B), exponential background (C), broad luminosity function (D), metallicity gradient (E), S-model prior with $Z_\odot = 15$ pc (F), S-model prior and broad luminosity function with $Z_\odot = 15$ pc (G), S-model prior with $Z_\odot = 0$ pc (H), S-model prior with $Z_\odot = 0$ pc with a broad luminosity function (I), extinction mask (J). Note that as case J has a different amount of data, its $-2\ln\mathcal{L}$ value cannot be compared directly with the other cases.

	VVV Data		Simulation	
Case	Param.	Non-param.	Param.	Non-Param.
A	0	0	0	0
B	17086	974	733	307
C	65507	60554	55654	69758
D	-1793	2917614	13797	76778
E	266	184	109	-1641
F	38934	241421	-5523	176708
G	21665	209841	15475	161736
H	19723	1361	640	95
I	15107	25589	22740	6252
J	-2×10^7	-4×10^7	-2×10^7	-3×10^7

Table 2.5 Parametric SX and S-models fitted to VVV data used as priors in Table 2.4. The best fits and 68% errors are given for each case on alternating lines.

Label	$c_\perp$	$c_\parallel$	x_0	y_0	z_0	$\rho_0 \times 10^6$	α	ΔR_0	C	A	x_1	y_1	n
A) Base case	1.581	2.359	1.853	0.672	0.4605	0.123	20.12	-0.0968	1.386	0.69	0.731	1.090	2.31
	0.008	0.009	0.006	0.001	0.0004	0.002	0.03	0.0009	0.005	0.02	0.004	0.005	0.09
B) No feature behind the bar incorporated into background	1.856	2.319	1.88	0.664	0.4544	0.119	18.0	-0.198	1.359	0.68	0.781	1.11	2.2
	0.007	0.008	0.02	0.002	0.0007	0.003	0.2	0.001	0.004	0.05	0.007	0.02	0.2
C) Exponential background instead of MaxEnt background	1.309	3.177	1.641	0.7105	0.4798	0.1158	23.55	-0.0386	1.346	0.6246	0.621	0.734	1.981
	0.001	0.002	0.001	0.0007	0.0003	0.0001	0.002	0.0005	0.002	0.0009	0.001	0.001	0.001
D) Broad luminosity function	1.172	2.124	1.735	0.610	0.4658	0.1788	28.88	-0.0711	1.356	2.13	0.170	1.135	18.0
	0.007	0.009	0.008	0.002	0.0007	0.0009	0.06	0.0009	0.003	0.04	0.003	0.008	0.4
E) Metallicity gradient accounted for	1.546	2.383	1.884	0.6802	0.4582	0.1193	19.863	-0.1127	1.389	0.727	0.729	1.057	2.244
	0.002	0.002	0.002	0.0003	0.0002	0.0002	0.001	0.0007	0.001	0.001	0.002	0.001	0.002
F) S-model prior with $Z_\odot = 15$ pc	1.677	2.616	1.3812	0.58753	0.42	0.2322	19.7886	-0.0724	-	-	-	-	-
	0.0003	0.0002	0.0002	0.00012	0.0003	0.0004	0.0003	0.0003	-	-	-	-	-
G) S-model prior and broad luminosity function with $Z_\odot = 15$ pc	1.242	2.779	1.2332	0.4819	0.40921	0.3687	31.945	-0.0698	-	-	-	-	-
	0.001	0.003	0.0013	0.0004	0.00018	0.0005	0.005	0.0008	-	-	-	-	-
H) S-model prior with $Z_\odot = 0$ pc	1.6734	2.592	1.3921	0.5915	0.4271	0.2269	19.8241	-0.0767	-	-	-	-	-
	0.0008	0.003	0.0009	0.0004	0.0002	0.0002	0.0003	0.0008	-	-	-	-	-
I) S-model prior with $Z_\odot = 0$ pc & broad luminosity function	1.221	2.733	1.253	0.4884	0.41672	0.3596	31.851	-0.0712	-	-	-	-	-
	0.003	0.004	0.0012	0.0004	0.00016	0.0004	0.006	0.0006	-	-	-	-	-
J) Extinction mask	0.970	2.691	26.442	0.7440	0.4786	0.004990	18.768	-0.1018	1.302	38.903	0.815	0.891	0.8855
	0.002	0.001	0.002	0.0007	0.0002	0.000005	0.002	0.0006	0.001	0.002	0.001	0.001	0.0009

Table 2.6 Parametric SX and S-models, fitted to an S-model simulation. The best fits and 68% errors are given for each case on alternating lines.

Label	$c_\perp$	$c_\parallel$	x_0	y_0	z_0	$\rho_0 \times 10^6$	α	ΔR_0	C	A	x_1	y_1	n
A) Base case	1.864	2.464	1.608	0.6851	0.4845	0.1492	19.414	-0.0031	1.8136	0.42	0.0003	0.409	0.022
	0.004	0.003	0.001	0.0006	0.0002	0.0007	0.006	0.0003	0.0006	0.01	0.0002	0.005	0.001
B) No feature behind the bar incorporated into background	1.864	2.467	1.600	0.6846	0.4835	0.1897	19.405	-0.0023	1.092	-0.016	0.050	7.538	0.178
	0.003	0.004	0.001	0.0004	0.0002	0.0003	0.003	0.0006	0.003	0.003	0.001	0.005	0.002
C) Exponential background instead of MaxEnt background	1.733	2.481	1.545	0.7116	0.4943	0.1932	21.17	0.0638	0.6724	-0.205	0.020	2.10	0.222
	0.004	0.005	0.002	0.0006	0.0003	0.0007	0.02	0.0004	0.0006	0.006	0.002	0.04	0.007
D) Broad luminosity function	1.893	2.545	1.377	0.6043	0.4785	0.2386	26.90	0.0460	2.659	0.402	0.011	1.954	0.40
	0.008	0.007	0.002	0.0006	0.0004	0.0005	0.03	0.0007	0.002	0.001	0.001	0.007	0.02
E) Metallicity gradient accounted for	1.852	2.523	1.601	0.6864	0.4843	0.1817	19.10	-0.0178	7.483	0.019	2.779	4.51	8.308
	0.004	0.005	0.001	0.0005	0.0003	0.0003	0.01	0.0008	0.005	0.001	0.008	0.01	0.006
F) S-model prior with $Z_\odot = 15$ pc	1.868	2.506	1.586	0.6790	0.4746	0.1930	19.49	-0.0003	-	-	-	-	-
	0.003	0.004	0.001	0.0004	0.0002	0.0002	0.04	0.0007	-	-	-	-	-
G) S-model prior and broad luminosity function with $Z_\odot = 15$ pc	1.9941	2.6591	1.30221	0.56743	0.4640	0.2677	29.2638	0.0548	-	-	-	-	-
	0.0002	0.0002	0.00008	0.00005	0.0001	0.0002	0.0001	0.0003	-	-	-	-	-
H) S-model prior with $Z_\odot = 0$ pc	1.861	2.476	1.599	0.6841	0.4840	0.1886	19.552	-0.0065	-	-	-	-	-
	0.003	0.003	0.001	0.0005	0.0002	0.0002	0.004	0.0006	-	-	-	-	-
I) S-model prior with $Z_\odot = 0$ pc & Broad luminosity function	1.954	2.604	1.3187	0.5733	0.4740	0.2616	29.2719	0.0514	-	-	-	-	-
	0.001	0.002	0.0006	0.0003	0.0002	0.0002	0.0009	0.0006	-	-	-	-	-
J) Extinction mask	1.839	2.513	1.582	0.6844	0.4861	0.1851	19.84	-0.0164	6.76	0.041	0.98	2.23	0.82
	0.005	0.006	0.002	0.0006	0.0004	0.0004	0.02	0.0007	0.05	0.003	0.01	0.07	0.03

2.5.8 Deconvolution Method Systematic

Our last systematic check involved performing a modified Richardson-Lucy deconvolution used in the RC bulge morphology work of WG13. As our data differ from their study in several aspects, such as completeness and photometry, we attempt a faithful reproduction of their method on our own data set for comparison with our best fit MEM deconvolution bulge density. We also consider how our alternate background fitting and luminosity function choices affect this particular method substituting these into the Richardson-Lucy fit. We retain our luminosity function described in Section 2.2.2, denoted by PARSEC for this discussion, and for the WG13 comparison we implement their parametric luminosity function. Their parametric luminosity function was obtained by fitting Gaussians to Monte-Carlo samples via the BaSTI isochrone set. This entailed drawing stellar masses from a Salpeter IMF and using the Baade's window metallicity distribution measured by Zoccali et al. (2008), interpolating the α enhanced BaSTI isochrones (Pietrinferni et al., 2004) for a 10 Gyr population providing the K_s absolute magnitude distribution, then fitting the RC and RGBB with Gaussians along with an exponential to account for the remaining RGB. The RC and RGBB Gaussian parameters were: $\mu_{\mathrm{M_{K_s,RC}}} = -1.72$, $\sigma_{\mathrm{RC}} = 0.18$, $\mu_{M_{\mathrm{K_s,RGBB}}} = -0.91$, $\sigma_{\mathrm{RGBB}} = 0.19$, and relative RGBB fraction to the RC of $f_{\mathrm{RGBB}} = 0.20$ (μ and σ taking their typical meanings in a Gaussian distribution). Notably the position of the RC is shifted by nearly 0.2 mag from our PARSEC implementation, and an RC dispersion 3 times wider. In contrast to our MEM-based background fitting using Besançon disc priors, the WG13 style background fitting involves a second order exponential background of the form:

$$B(K_s) = \exp(a + b(K_s - 13) + c(K_s - 13)^2) \tag{2.37}$$

fitted for each line-of-sight. The fit is restricted to $11 \leq K_s \leq 11.9$ mag and $14.3 \leq K_s \leq 15$ mag to minimise RC influence. We retained their other considerations when fitting too. Regions of higher extinction and crowding ($|b| < 2^\circ$) had the c coefficient set to 0 and upper magnitude limit reduced from 15 to 14.5. For $l \geq 5.5^\circ$ the brighter magnitude range was reduced to $11 \leq K_s \leq 11.7$ to account for the RC being brighter in apparent magnitude due to the bulge angle. The star count model for each field of view takes the form of Eq. 2.4, converted to the form of a background plus a linear convolution via the transform of line-of-sight distance (s) to distance modulus (μ). The luminosity function was convolved with the mean combined photometric and systematic uncertainty for each K_s along each line-of-sight to account for their effects. The VVV data was re-discretised into $\sim 1.5^\circ \times \sim 0.5^\circ$ spatial bins over 0.05 mag K_s

bins. For each line-of-sight, the density distribution was initialised to a Hann window (i.e. $\sin(\pi(\mu-\mu_0)/L)^2$) for distance modulus window of width L and lower bound μ_0) function over a distance modulus of 11.2 to 17, renormalised to produce the observed line-of-sight counts. We then applied the modified Richardson-Lucy procedure of WG13, retaining their stopping criteria, for both the BaSTI and PARSEC luminosity functions.

This produced an estimate of the bulge density which depended on μ which we mapped onto a density which depends on s. We then reprojected the bulge density to Cartesian form using linear interpolation. For the low resolution data, step sizes of $(\Delta x \times \Delta y \times \Delta z) = (0.15 \times 0.1 \times 0.075)$ kpc were used. This simple reprojection only produced a noisy unsymmetrised view of the density model. For a view of the deconvolved bulge density assuming eight-fold symmetry, the appropriate frame needs to be found.

We applied a process of finding the maximally eight-fold symmetric frame following WG13. For each slice in the z direction, we carried out a simple grid search over distance to the Galactic centre R_0 and bulge angle α, in steps of 0.02 kpc and 0.5 deg. For each α fixed, we shifted the bulge centre to some value of R_0 and computed the symmetrised density

$$\bar{\rho}(x,y,z) = \frac{1}{N}\left[\rho(x,y,z) + \rho(-x,y,z) + 6 \text{ other octants}\right] \tag{2.38}$$

where octant positions without matching densities in the (l,b,s) projection were ignored from the computation. Parameter N is the number of octants with non-masked densities. Then the quantity

$$\frac{1}{\mathrm{N_z}} \sum_{z=0.4\mathrm{kpc}}^{1\mathrm{kpc}} \frac{\langle \rho_{\mathrm{rms}} \rangle_z}{\langle \rho \rangle_z} \tag{2.39}$$

was minimised, where N_z is the number of slices between 0.4 and 0.8 kpc in the chosen Cartesian grid, so the quantity is comparable between resolutions. The parameter ρ_{rms} denotes the root mean square deviation between each octant's density in the symmetrisation and the average density, $\bar{\rho}$, of those points, which was then averaged across all points in each z-slice.

Rather than minimising Eq. 2.39 directly, $\langle \rho_{\mathrm{rms}} \rangle_z / \langle \rho \rangle_z$ was minimised over individual slices of z for our R_0 grid search. This was an intermediary step in the bulge angle selection process to account for potential magnitude shifts in the model resulting from factors such as metallicity gradients, on top of the required shift in finding the maximally eight-fold symmetric frame.

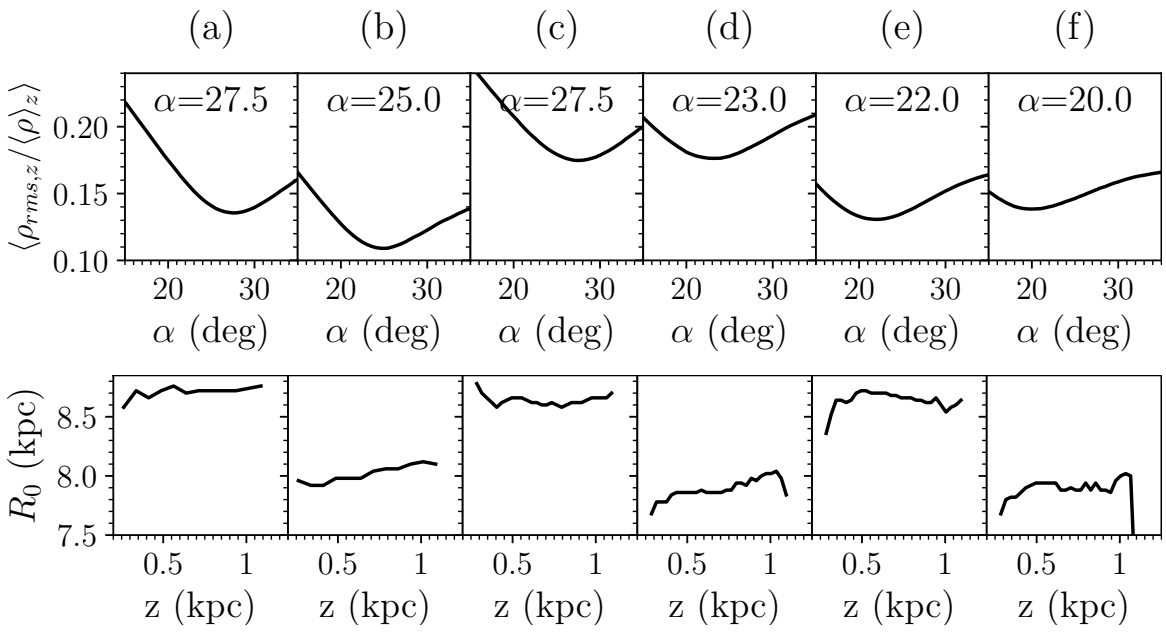

Fig. 2.20 Maximally eight-fold symmetric angle (top) and R_0 (bottom) orientation of modified Richardson-Lucy deconvolved data. From left to right: (a) BaSTI luminosity function on low resolution data (b) PARSEC luminosity function on low resolution data (c) BaSTI luminosity function on high resolution data (d) PARSEC luminosity function on high resolution data (e) BaSTI luminosity function on simulated data (f) PARSEC luminosity function on simulated data.

This process was then repeated for $0.2^\circ \times 0.2^\circ$ spatial bins using our maximum entropy derived background, described in Section 2.2.4, and Cartesian grid spacing adjusted to $(\Delta x \times \Delta y \times \Delta z) = (0.04 \times 0.04 \times 0.03)$ kpc, to accommodate the finer data resolution.

In Fig. 2.20, we recovered the relation observed in S17, in which the broader BaSTI luminosity function results in a larger bulge angle in comparison to the narrower PARSEC luminosity function. We note how the shift in R_0 for each slice to maximise eight-fold symmetry is nearly flat with a constant shift in the BaSTI cases and a much shallower gradient than found by WG13 in our semi analytic PARSEC luminosity function cases. Figures 2.21 and 2.22 show our density deconvolutions on the data using the BaSTI and PARSEC luminosity functions across the two different resolutions we considered. The region used in the maximisation of eight-fold symmetry, compatible with WG13, is bounded by a white rectangle. The X-bulge structure and features seen in WG13, such as the near-far RC density asymmetry, are visibly recovered. The K- and K_s-band RC magnitude widths being observed using *Gaia* DR2 of 0.03-0.09 mag

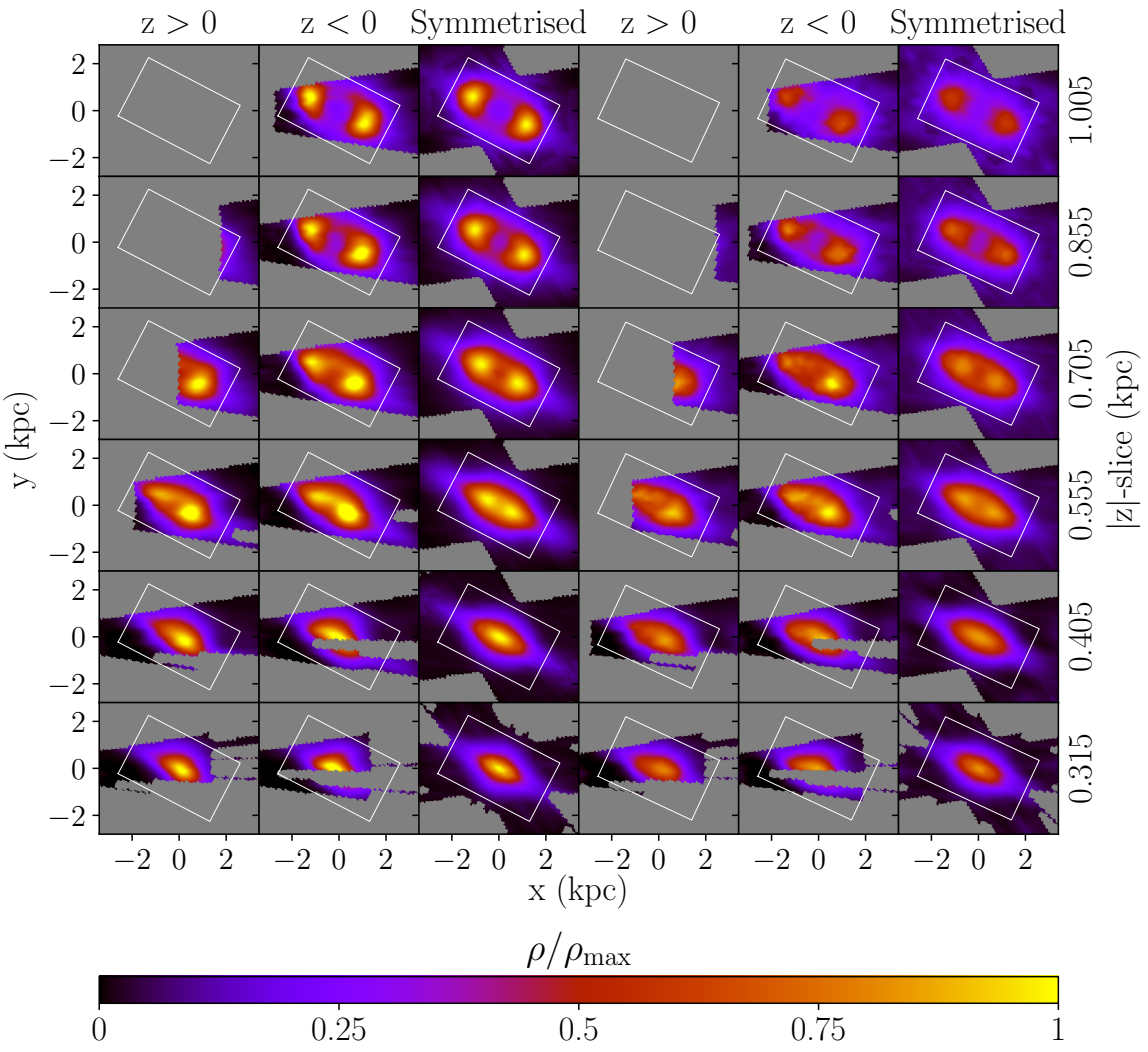

Fig. 2.21 Three dimensional reconstruction of low resolution VVV data. Columns 1-3 using BaSTI luminosity function and 4-6 using PARSEC luminosity function. Slices of $|z|$ (measured in kpc) normalised by the maximum of the BaSTI symmetrised model.

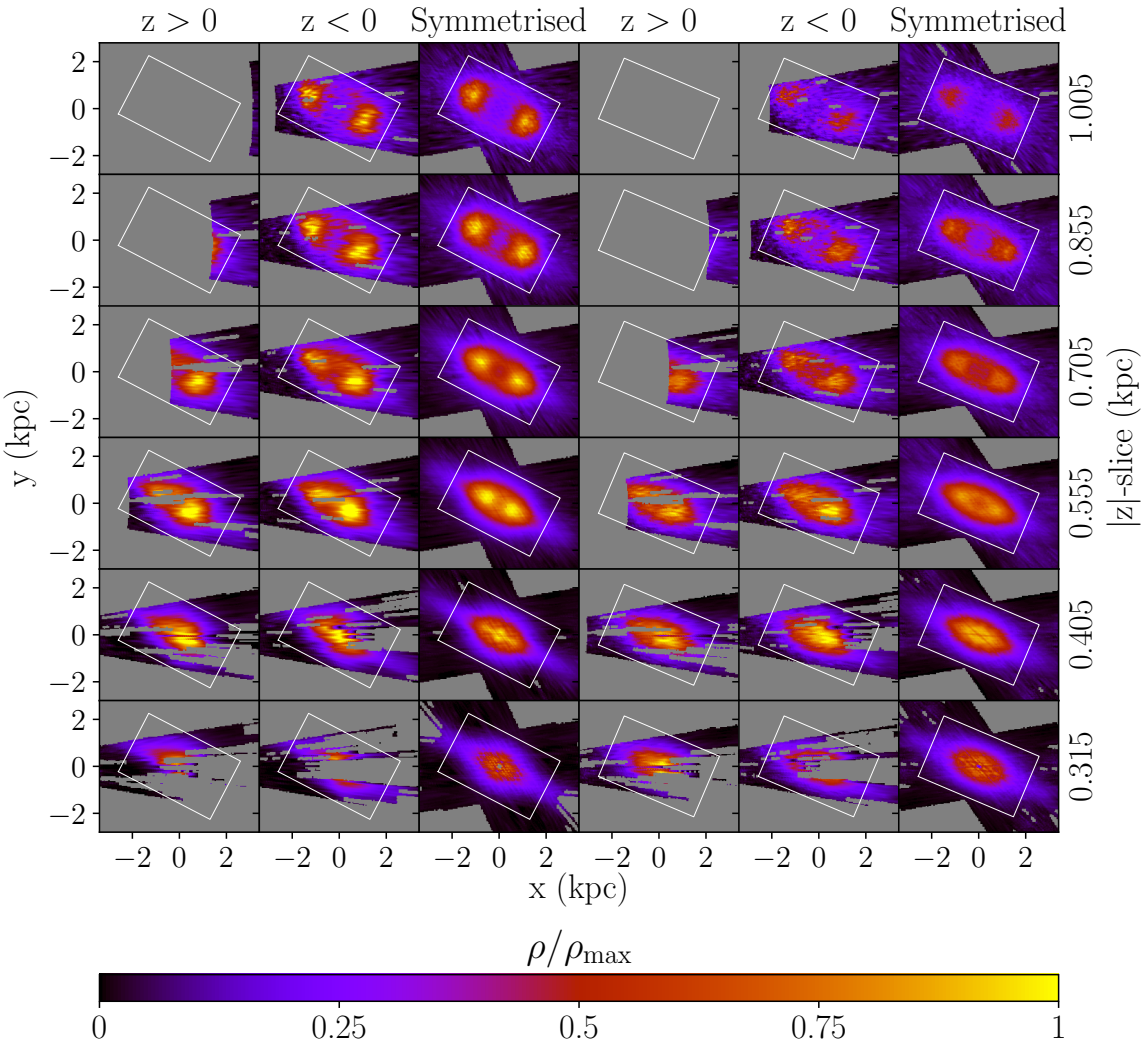

Fig. 2.22 Three dimensional reconstruction of high resolution VVV data. Columns 1-3 using BaSTI luminosity function and 4-6 using PARSEC luminosity function. Slices of $|z|$ are measured in kpc.

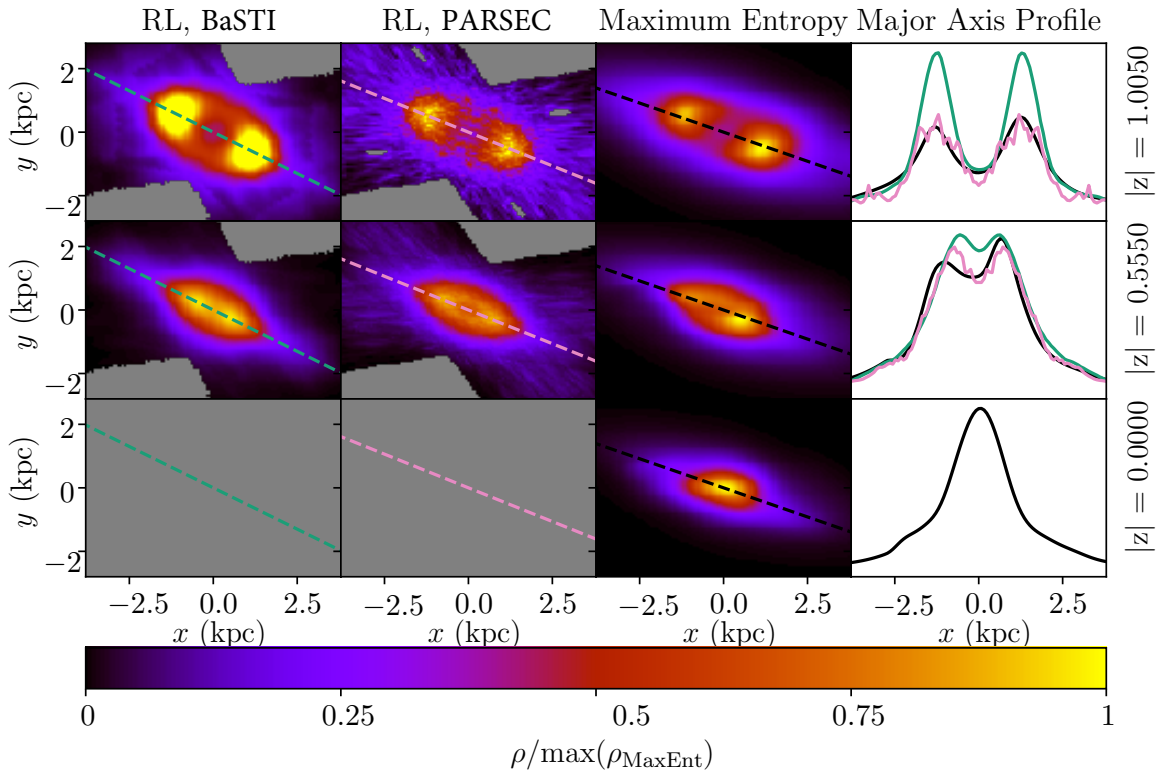

Fig. 2.23 Comparison between the modified Richardson-Lucy (RL) deconvolution and maximum entropy deconvolution. The left column implements the same method and resolution as WG13 except on our updated data set. The middle column is constructed in the same way as the left column except that the narrower PARSEC luminosity function is used instead of the BaSTI luminosity function used by WG13. Density slices have been normalised to the maximum value in the corresponding maximum entropy slice. The green, pink, and black profile plots in the fourth column are along the lines shown in column one, two, and three respectively. Slices of $|z|$ are measured in kpc.

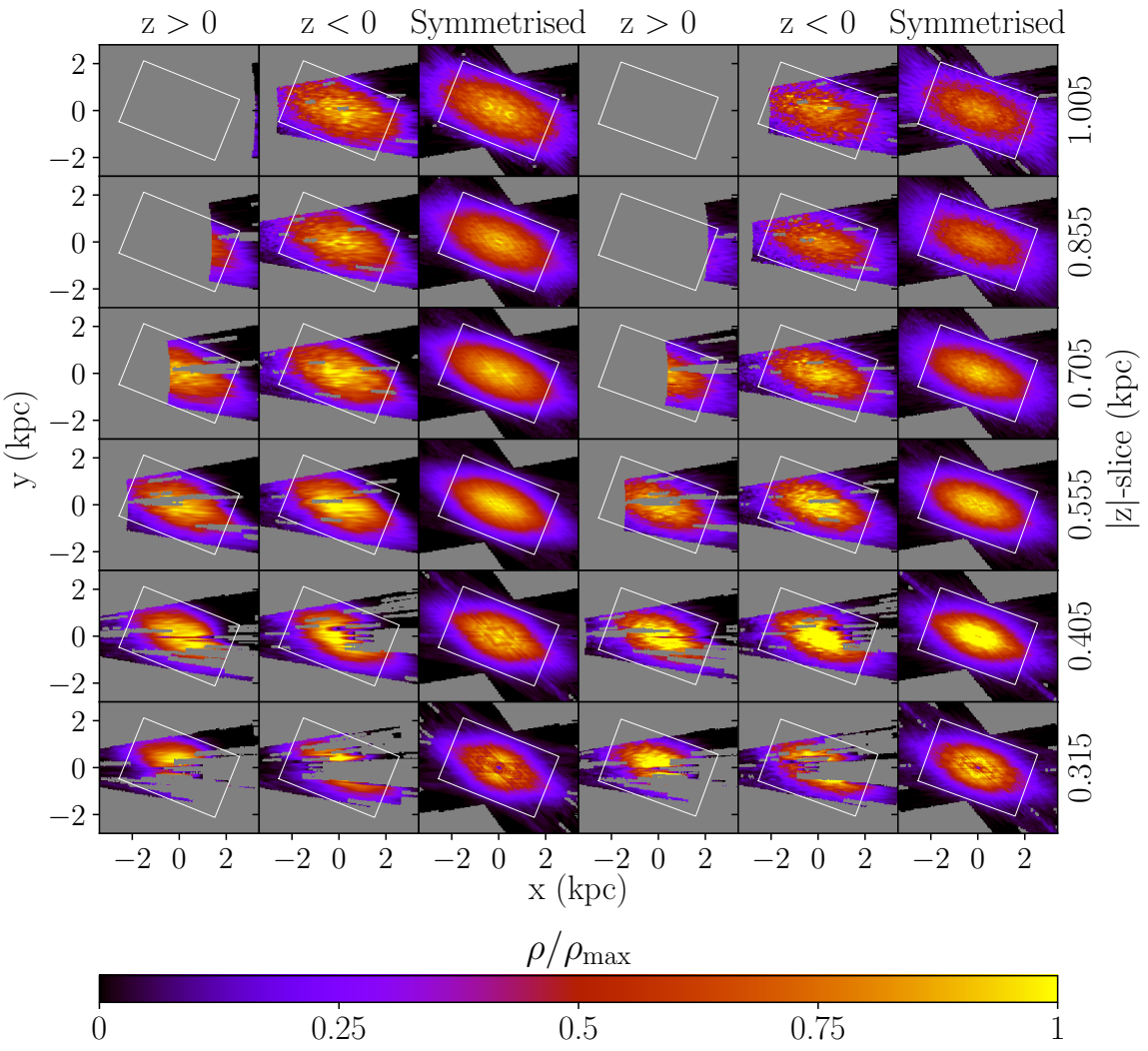

Fig. 2.24 Three dimensional reconstruction of S-model simulations. Columns 1-3 using BaSTI luminosity function and 4-6 using the PARSEC luminosity function. Slices of $|z|$ are measured in kpc.

(Hall et al., 2019; Chan & Bovy, 2019) are consistent with the PARSEC luminosity function which is narrower than the BaSTI luminosity function.

In Fig. 2.23 we show a comparison between the modified Richardson-Lucy deconvolution and our non-parametric method. As illustrated by the profile plot in the right most panel, the modified Richardson-Lucy deconvolution with the BaSTI luminosity function has significantly denser X-arms at high $|z|$. However, this is primarily due to the use of the BaSTI luminosity function rather than the PARSEC luminosity function. If the PARSEC luminosity function is used with the modified Richardson-Lucy deconvolution (as in the second column) then the peaks are similar to our non-parametric deconvolution. Whereas in the second column of the figure, when the PARSEC luminosity function is used with the modified Richardson-Lucy deconvolution, a much noisier reconstruction is obtained even though the low resolution case is being used. The PARSEC luminosity function has an intrinsic RC dispersion that is more consistent with observations (as mentioned above). It is a distinct advantage that our non-parametric model can give non-noisy reconstructions with the narrower PARSEC luminosity function at higher resolution. We checked the method against simulations for the finer resolution to examine possible shortcomings in that regime independently of the actual data.

In Fig. 2.24 we show the results of the deconvolution and symmetrisation of the simulated data with our standard $0.2^\circ \times 0.2^\circ$ resolution. The bulge angle was effectively recovered using 0.5° steps in a grid search for the PARSEC luminosity function case and a larger angle using the broader BaSTI luminosity function as seen in our earlier results and also by S17. The shift in R_0 is mostly flat across z slices in both cases with a slight negative gradient in the BaSTI case. Comparing to the gradient in the data fits, it is not apparent whether or not these comparably shallow gradients are spurious. The R_0 eight-fold symmetric maximisation on the data results in a very flat shift in R_0 across z slices between 400 and 800 pc. Above 800 pc the counts are very low at this resolution, causing excessively noisy features and below 400 pc our mask starts interfering substantially with the symmetrisation procedure. We find a negligible gradient using the broader BaSTI derived luminosity functions. It is not clear within this method how one might interpret the apparent magnitude-shift gradient depending on the broadness of the luminosity function here and how much of it is an artefact of the symmetrisation, when there is a persistent asymmetry at odds with the assumption of eight-fold symmetry. Our metallicity distribution systematic in Section 2.5.4 for comparison, found unimodal corrections driven by observation were negligible.

2.6 Derived Properties of the Bulge

2.6.1 Mass of the bulge

From the fitted density and IMF we can estimate the total mass of the bulge. Integrating the RC+RGBB stellar density over the entire bulge region gives us a total of 19.1×10^6 (RC + RGBB) stars. Based on our luminosity function, 0.062% of all stars are in either the RC or RGBB, so the total number of stars in the bulge is $N_{\rm total} = 30.7 \times 10^9$. Stars in the 10 Gyr bulge with a mass $\gtrsim 1 M_\odot$ have evolved into stellar remnants, so the normalisation of the IMF is then given by

$$\xi_0 = \frac{N_{\rm total}}{\int_{0.15 M_\odot}^{1 M_\odot} \xi(m)\, {\rm d}m}, \tag{2.40}$$

where ξ is the IMF and ξ_0 is the normalisation of the IMF. We use the Chabrier IMF, which was also used to generate our luminosity function. With the IMF correctly normalised, the mass of the bulge is then calculated by integrating the IMF multiplied by the final mass of the star, over the range $0.15 M_\odot < m < 150 M_\odot$. Stars with an initial mass $< 1 M_\odot$ have not yet evolved into remnants, so the final mass is equal to the initial mass. Stars with initial mass $1 M_\odot < m < 8 M_\odot$ have evolved into white dwarfs, where the final mass is related to the initial mass by $m_f = 0.48 + 0.077 m_i$ (Maraston, 1998). To determine the final mass stars with initial mass $> 8 M_\odot$, which have evolved into neutron stars or black holes, we use the results of the numerical population synthesis code SEVN (Spera et al., 2015). Therefore, the total stellar mass of the bulge (assuming a Chabrier log-normal IMF) is $M_{bulge} = 1.64 \times 10^{10} M_\odot$. This includes the mass of the stellar remnants, which make up 30.1% of the total mass.

Parametric modelling of VVV bulge stars in S17 found a total stellar mass of the bulge assuming a Chabrier IMF of $2.36 \times 10^{10} M_\odot$, with the stellar remnants making up 49% of the total mass. Both the total mass and remnant fraction of S17 are larger than we are reporting. However, if we were to have the same remnant fraction as S17, then our total mass would be $2.24 \times 10^{10} M_\odot$ which would be consistent with S17 once our systemic uncertainties have been incorporated.

A dynamical estimate of the bulge mass by combining the VVV bulge stellar distribution of WG13 with kinematic information from BRAVA in Portail et al. (2015a) found a bulge stellar mass of 1.3-1.7$\times 10^{10} M_\odot$, which is consistent with our estimated mass. They also provide a mass-to-clump ratio, which is used to estimate the total stellar mass of the bulge from the number of RC+RGBB stars. For a Chabrier IMF,

Table 2.7 Total stellar mass estimate for the Galactic bulge for all test cases. A Chabrier IMF was assumed, which gave a remnant fraction of 30.1% The cases considered are: base (A), no behind-the-bar feature subtraction (B), exponential background (C), broad luminosity function (D), metallicity gradient (E), S-model prior with $Z_\odot = 15$ pc (F), S-model prior and broad luminosity function with $Z_\odot = 15$ pc (G), S-model prior with $Z_\odot = 0$ pc (H), S-model prior with $Z_\odot = 0$ pc with a broad luminosity function (I), and extinction mask (J). The mass of the simulated stellar population is $\mathrm{Mass}^{\mathrm{Sim}}_{\mathrm{Bulge}} = 1.92 \times 10^{10} M_\odot$.

Case	$\mathrm{Mass}^{\mathrm{VVV}}_{\mathrm{Bulge}}$ ($\times 10^{10} M_\odot$)	$\mathrm{Mass}^{\mathrm{Sim}}_{\mathrm{Bulge}}$ ($\times 10^{10} M_\odot$)
A	1.64	1.89
B	1.70	1.92
C	1.33	1.84
D	1.61	1.90
E	1.63	1.89
F	1.52	1.91
G	1.58	1.93
H	1.53	1.92
I	1.57	1.93
J	1.71	1.90

there are approximately $905 M_\odot$ of bulge mass for each RC+RGBB star. So for our estimated 19.1×10^6 (RC+RGBB) stars the estimated mass was $1.73 \times 10^{10} M_\odot$. This is remarkably similar to our value, considering Portail et al. (2015a) used different isochrones, metallicity distribution and treatment of the compact remnants to those used in our estimation. Additionally, we list the bulge mass estimates for all of our systematic test cases in Table 2.7. The mass estimates tabulated for the simulated data encompass the mass of the model used for the simulation with a spread of a few percent. As the systematic error is much greater than the statistical error, we use the range of best fit bulge mass estimates for our different cases to get an estimate of the uncertainty in our mass estimate. The mass estimates for the bulge from the VVV data are in the range 1.33-1.71 $\times 10^{10} M_\odot$, which is in agreement with the results of Portail et al. (2015a).

2.6.2 Distance to the Galactic centre

As mentioned previously, we associate the Galactic centre with the location of the maximum density of the bulge. In all cases we examined, this maximum bulge density was in the same location for the parametric and non-parametric fit. According to

Table 2.8 Ratios given by the X component of each corresponding model integrated in all directions down to a scalar divided by overall integrated SX model, for data and simulation fits.

	A	B	C	D	E	J
Data	0.23	0.23	0.18	0.25	0.24	0.92
Simulations	0.20	-0.0062	-0.048	0.012	0.018	0.016

our base non-parametric model, the distance from the Sun to the Galactic centre is 7.9 kpc, where the assumed mean absolute magnitude of the RC is $\mu_{M_{Ks},RC} = -1.53$. WG13 found the main effect of changing $\mu_{M_{Ks},RC}$ was to change the distance to the Galactic centre. If we had instead used the observed local RC mean magnitude of $\mu_{M_{Ks},RC} = -1.62$ (Chan & Bovy, 2019; Hall et al., 2019), then all distances would be increased by a factor of 1.04. With the brighter RC, the distance to the Galactic centre would then be 8.24 kpc, which is consistent within the 2σ boundary of a recent measurement of 8.18 ± 0.04 kpc calculated using parallax observations of Sgr A* (Gravity Collaboration et al., 2019).

2.6.3 Estimating the X-component proportion

The X component was obtained by setting the 1 in $(1+A)$ from the SX model definition in Eq. 2.25 to 0. The X-component proportion was then computed by integrating the X component and SX model over all coordinates and then taking the ratio of them. These ratios are listed in Table 2.8.

A partial degeneracy in the SX model, due to allowing the X-arm power-law exponent (n) to vary, turns up in our extinction mask parametric fit (case J) to the data. The additional density unveiled by the extinction mask depicted in Fig. 2.19 may be the main driving factor in this behaviour which only showed up in that model case. The result of this is visible in Fig. 2.16, where the J case is an outlier in the A and n parameters. With an exponent, n, less than 1, the X-arms become very broad. This case is not shown in Fig. 2.14 because it involves a different amount of data, so the change of likelihood will be on a different scale to that in the other cases. Another case of A and n replacing the bulk of the S component of the SX model is in parametric case A on the simulations. A slice near the edge of the Galactic plane data mask, at 310 pc, is displayed in Fig. 2.25.

As the parameter n approaches 0, the perturbation tends towards a constant with a cusp at the X-arm origins from the exponential term. Although this model can appear

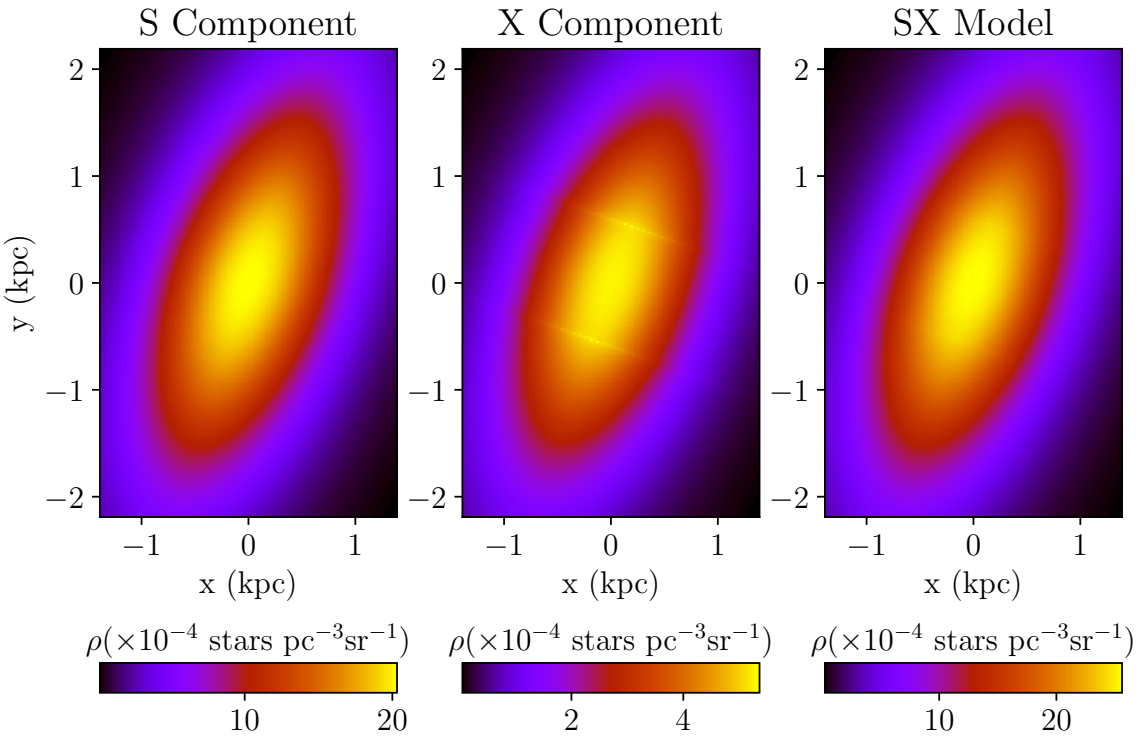

Fig. 2.25 Sample slice at $z = 310pc$ of the parametric model in case A, fitted to simulations. A simple ratio of the X component to the full SX model can imply there is a significant X-arm component when there is no X component. Due to the very small exponent $n \sim 0.02$, the X component has effectively the same shape as the S component only with small cusps at the origins of the exponential functions.

to have a strong X component, the fact we have $n \ll 1$ tells us that this component is near constant, so it is effectively adding to the normalisation of the S component rather than giving an X shaped perturbation. This result could in principle have come out for any of the simulation cases, so this behaviour is not particular to the A model, just the random model initialisation that resulted in a convergence to a model that has the X component trace the bulge rather than, for example, fall below the mask by having a large X-arm parting factor C.

Based on the above arguments we discard the A case parametric estimate for the simulation and the J case parametric result for the data in Table 2.8. It follows that our simulation results are consistent with a negligible X-component which is correct as the model used to generate the simulation had no X-component. Additionally, we can conclude that our parametric fit to the data has the X-component contributing a range of 18% to 25% to the bulge mass. This estimate of the X-bulge component contribution is consistent with that found for the WG13 model used by Portail et al. (2015a) which was 24%.

2.6.4 Bulge angle

As can be seen from Table 2.6 our bulge angles with respect to the Sun-Galactic centre line (α) for the simulation ranged from 19.1° to 29.3° which encompasses the simulated value of $\alpha = 19.2^\circ$. From Table 2.5 we can see that our parametric fit to the VVV data had bulge angles in the range of 18° to 32°. This is consistent with previous estimates. E.g. WG13 obtained a best fit of 27° and S17 obtained a best fit of 20°. The dependence of the viewing angle on the intrinsic RC luminosity dispersion for triaxial features was observed by Stanek et al. (1997) and S17. As σ_{RC} broadens, the depth of the bar needs to decrease along each line-of-sight. For a triaxial density, an increase in angle relative to the Sun-Galactic centre position will directly lead to a smaller depth through the bar for each line-of-sight.

2.7 Features In Front of and Behind the Bulge

In our non-parametric reconstruction with planar symmetry, we observed a feature behind the bar which has been associated with the spiral arm on that side of the Galaxy. Consequently, we later decided to relax some of our assumptions we had made for the purpose of application in Chapter 3 so we could explore any additional features more clearly that were not part of the RC model of the bulge. Here we re-trace the steps

of extracting stellar density features we observe and checks on the robustness of the features. We relaxed our assumption of North-South symmetry about the Galactic plane, added explicit disc modelling, and included all non-RC red giant components into our luminosity function. An update to the equation of stellar statistics in Eq. 2.4 to account for these changes takes the form:

$$N(K_s,l,b) = N_{\rm thin}(K_s,l,b) + N_{\rm thick}(K_s,l,b) + \Delta\Omega\Delta K_s \int_4^{13} \rho(s,l,b)\,\Phi(K_s - 5\log s - 10)\,s^2\,{\rm d}s, \quad (2.41)$$

where Φ is the combined luminosity function of the Red Giant Branch with Branch Bump, the Red Clump, and the Asymptotic Giant Branch Bump. $N_{\rm thin}$ and $N_{\rm thick}$ are the disc models described in Section 2.3 integrated into apparent magnitude form, with normalisation free. ρ is the red giant traced bulge density distribution. We used model H as the prior for ρ here.

Examples of our model fit broken down into its components are displayed in Fig. 2.26. In the high latitude example in the top panel, the VVV data set is noisy from low star counts. The reconstruction with these additional components still recovers the RC splitting through smoothing regularisation with neighbouring voxels in the 3D density grid. A consequence of this smoothing displayed in the lower panel of Fig. 2.26, where the high counts better constrains the distribution, but the total predicted counts appears to fall short of the observed distribution. Even though the non-parametric method can be adjusted to fit through the data-points much more tightly, the smoothing with neighbouring lines-of-sight that may differ significantly constrain this to give a more globally consistent reconstruction. This is depicted in Fig. 2.27, where the reconstruction within a latitude slice traces through the noise in the contours of the data set.

In Fig. 2.28 we plot a Cartesian projection of our density reconstruction, centred on the maximum density, in slices of z about the Galactic plane. The solid black line in the figure is the bulge angle of 19.8° that our parametric prior produces, close to the 19.6° angle in S17 with similar conditions. The X-arms remain visible at $|z| > 0.319$ kpc as in our earlier reconstruction. In addition, we observed towards the Galactic plane features in front of and behind the bulge at $x \sim \pm 3$ kpc.

The apparent spiral arm structures are consistent with the gas distribution simulated by Renaud et al. (2013)[3], displayed together in Fig. 2.29. Also plotted over top are

[3] http://www.astro.lu.se/~florent/mw_large.php

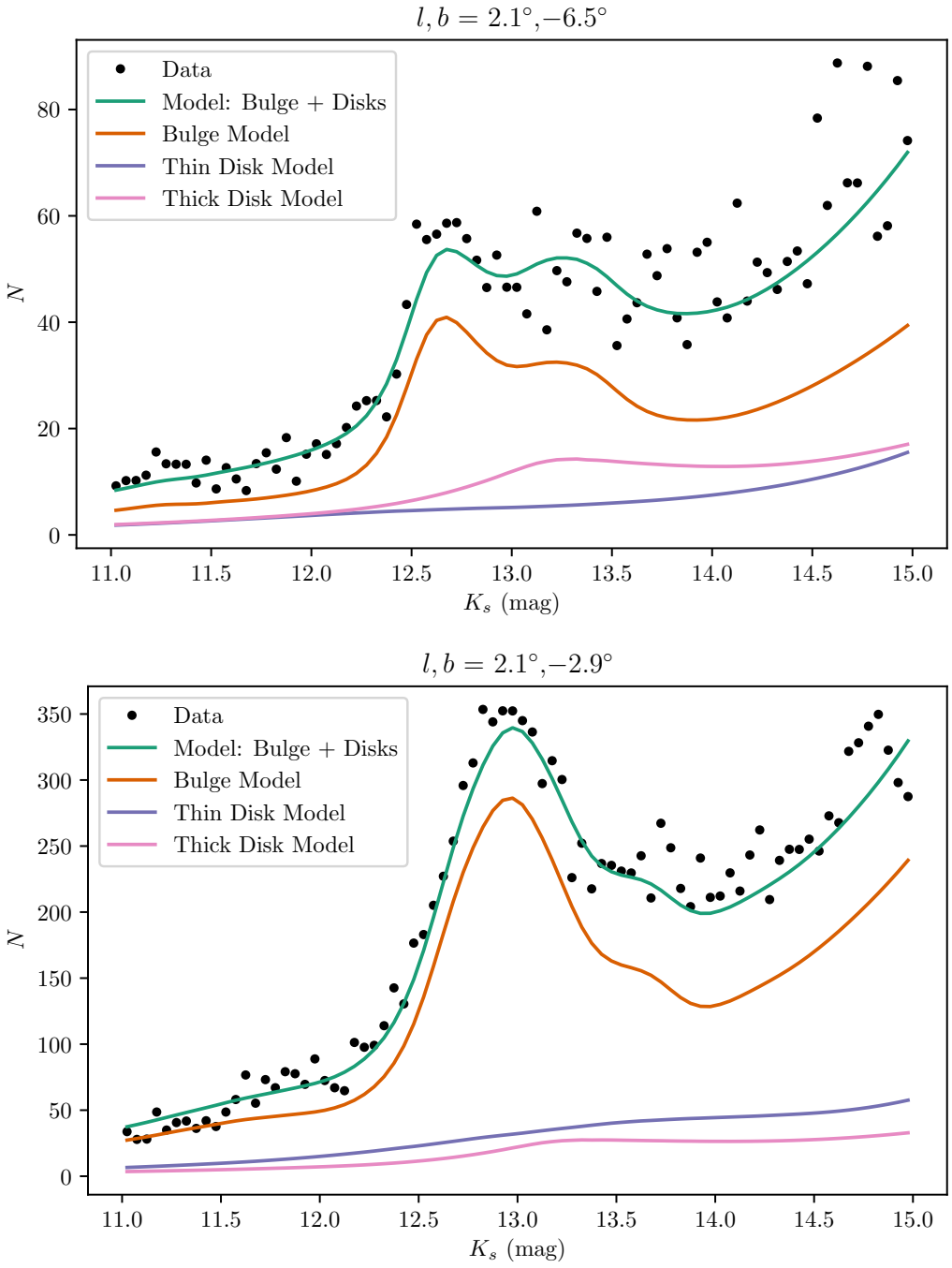

Fig. 2.26 Demonstration of the fitted model for a line-of-sight which displays a splitting in the RC (Top panel) and a line-of-sight which is near the edge of the masked mid-plane region (Bottom panel).

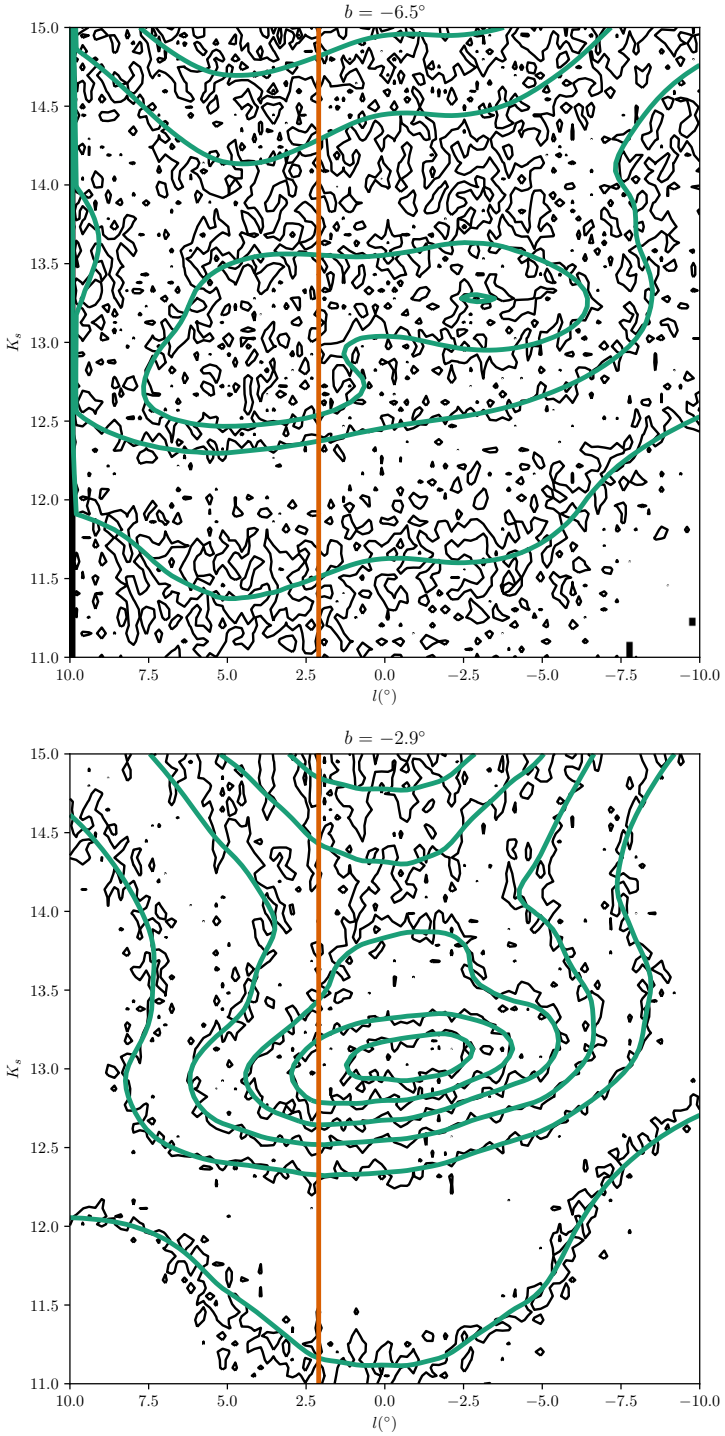

Fig. 2.27 Fitted model (green contours) as compared to the VVV data (black contours) for two representative latitude slices, one that shows the split RC at $b = -6.7°$ (top panel), and one that is near the Galactic mid-plane mask at $b = -2.9°$ (bottom panel). The line-of-sights in Fig. 2.26 are shown in orange.

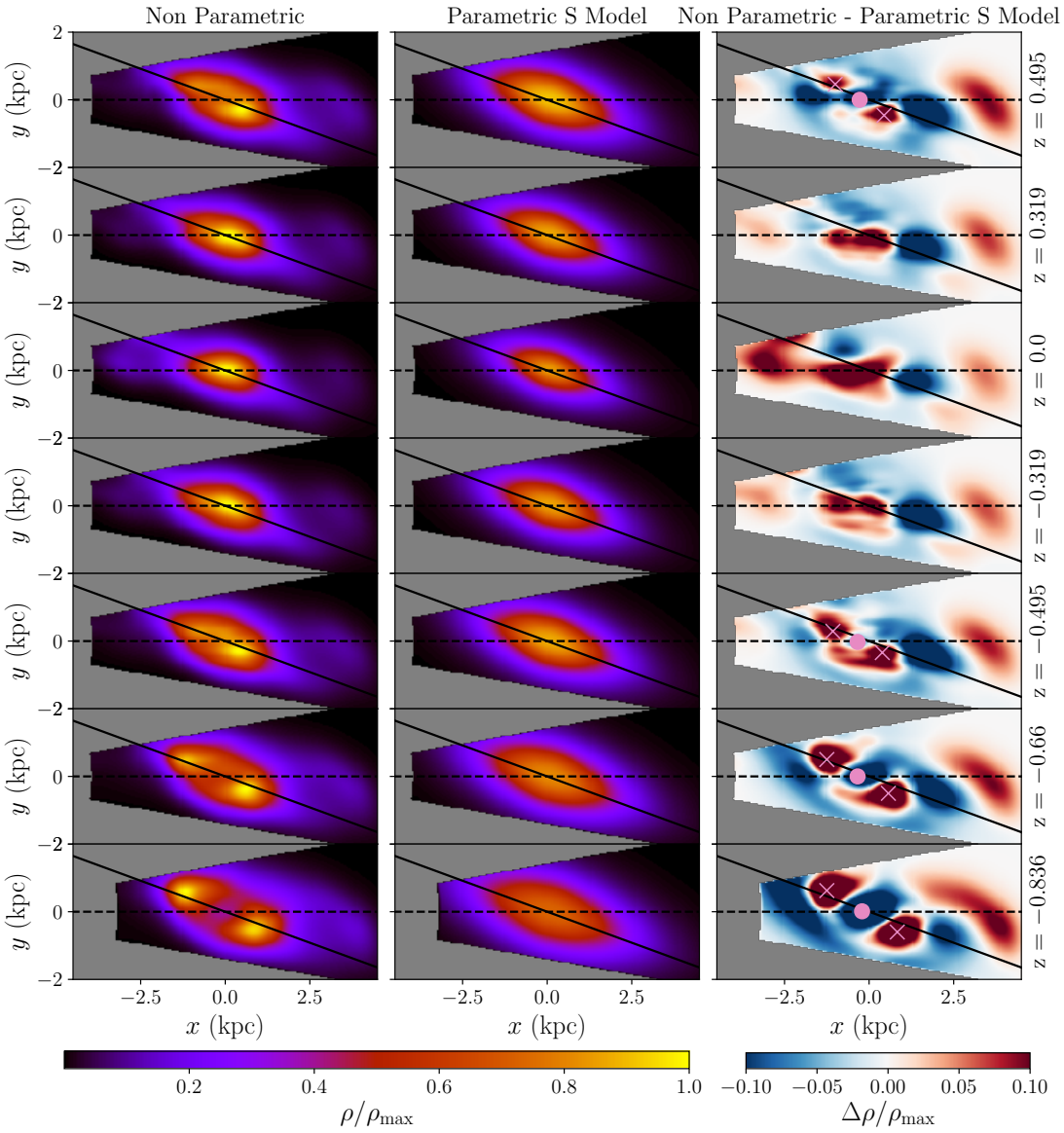

Fig. 2.28 Cartesian projections of the bulge density from the maximum entropy deconvolution (left column) and the parametric prior density of model (middle column). The Sun is located at $(x,y,z) = (-8.0, 0.0, 0.0)$. The dashed black line indicates $l = 0°$ and the solid black line is the major axis of the bulge in the parametric model which is at an angle of $19.8°$ from the $l = 0°$ line. The z coordinate is measured in kpc. At $x \sim \pm 3$ kpc the spiral arm structures at both ends of the bulge are visible, most clearly in the residuals (right column), which has had the colourbar clipped at $\pm 10\%$. The pink crosses indicate the maximum density of the X-arms, and the pink circle is the midpoint between the two arms.

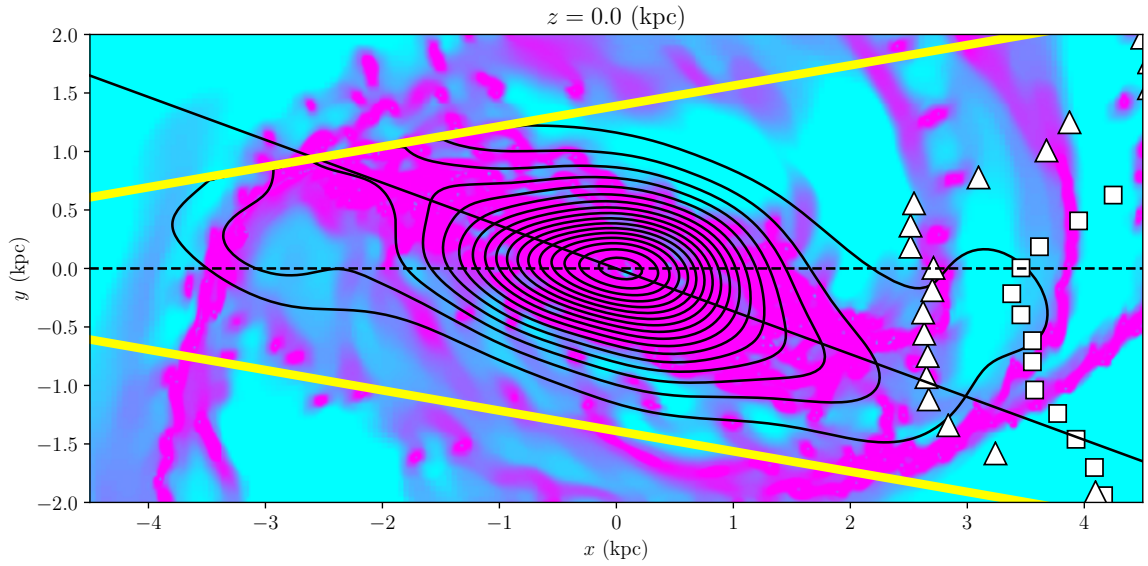

Fig. 2.29 VVV deconvolved stellar density (black contours) as compared to the simulated inner galaxy gas distribution of Renaud et al. (2013). The Sun is located at $(x,y,z) = (-7.9, 0.0, 0.0)$. The location of the spiral arm structure behind the bulge falls between the simulation (white squares) and VVV data analysis predictions (white triangles) of Gonzalez et al. (2018). The yellow lines show $l = \pm 10°$. The spiral arm structure at the end of the bulges are offset from the bulge major axis (black solid line).)

locations tracing the spiral arm structure of Gonzalez et al. (2018), which are closer to the Sun than our model predicts. This is likely due to our model only using fields of view which are not affected heavily by crowding and extinction, where zero-point calibration impact in K_s is more severe (Hajdu et al., 2019). Taking the RC peak from our luminosity function, $M_{K_s} \approx -1.53$ mag, and the distance from the Sun to this feature of 5 kpc, we obtain an apparent magnitude of $K_s \approx 11.96$ mag for the feature in front of the bar. Gonzalez et al. (2018) only used data with $K_s \gtrsim 12$ mag, which would not have been sensitive to this feature.

Gonzalez et al. (2018) noted that the RGBB of the bulge has a similar K_s to the feature behind the bulge. A mismodelling of the RGBB component could explain some of the density at high z from the Galactic mid-plane, shown in the right hand side panels of Fig. 2.28, where the spiral-arm-like density may not be expected.

We investigated the impact of the AGBB and RGBB contributions in Fig. 2.30. Doubling and zeroing the AGBB peak in our luminosity function, we see the respective decrease or increase expected for the size of the feature in front of the bulge. Likewise, we find a decrease and increase on the far end for doubling and zeroing the RGBB

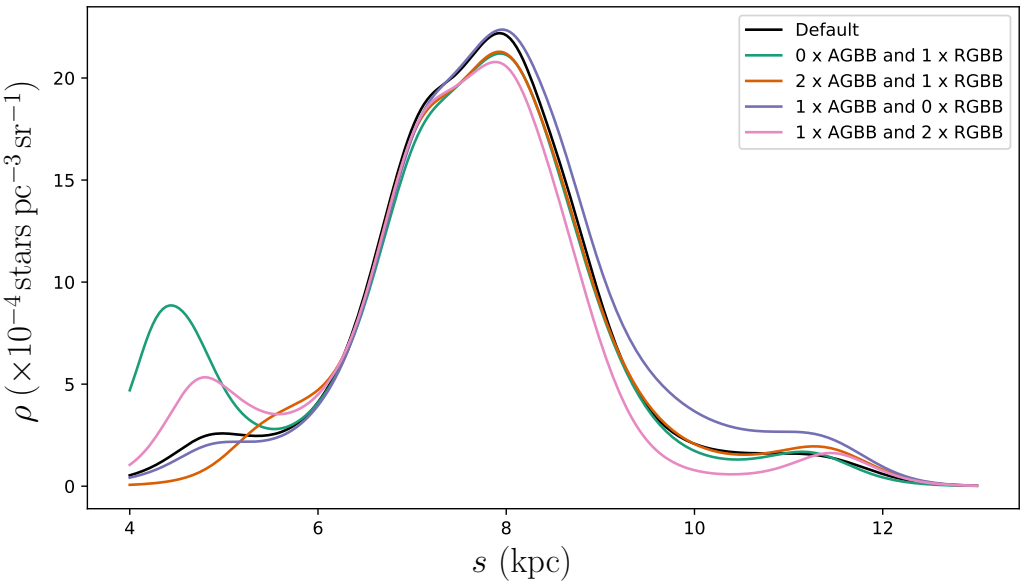

Fig. 2.30 Line-of-sight plots for $(l,b) = (-0.1^\circ, -2.9^\circ)$ of the reconstructed density for different luminosity functions. The 'Default" case is the reconstructed density from the VVV data, when our luminosity function shown in Fig. 2.2 is used. The other cases correspond to the default luminosity function but with either the AGBB or RGBB component multiplied by zero or two.

peak in our luminosity function, acknowledging the non-linear effect of varying this multi-component luminosity function. This indicates that the features in front of and behind the bulge are sensitive to the amplitudes assumed for the AGBB and RGBB. Though the extreme variations in amplitude are mainly for illustrative effect. Using a variation in RGBB and AGBB contributions of 20% and 30% respectively for example (approximately the RGBB and AGBB uncertainties in Nataf et al. (2011)), rather than a 100% variation as performed here, produced a much more negligible effect.

At low $|z|$ slices in Fig. 2.29 we see that the spiral-arm-like morphology behind the bar is mirrored by a similar form in front. We infer from this rotational symmetry at low $|z|$ and consistency with realistic N-body simulation that some amount of the density in the RGBB contaminated region is from a spiral-arm-like feature.

We examined the impact of mask choice, applying a $|b| < 1^\circ$ masking region. Again this produced a prominent finger to Sun feature near the Galactic plane with an over-density comparable to Fig. 2.19. This feature being a likely artefact of high photometric error, in addition to requiring the greatest zero-point offset when matched to 2MASS.

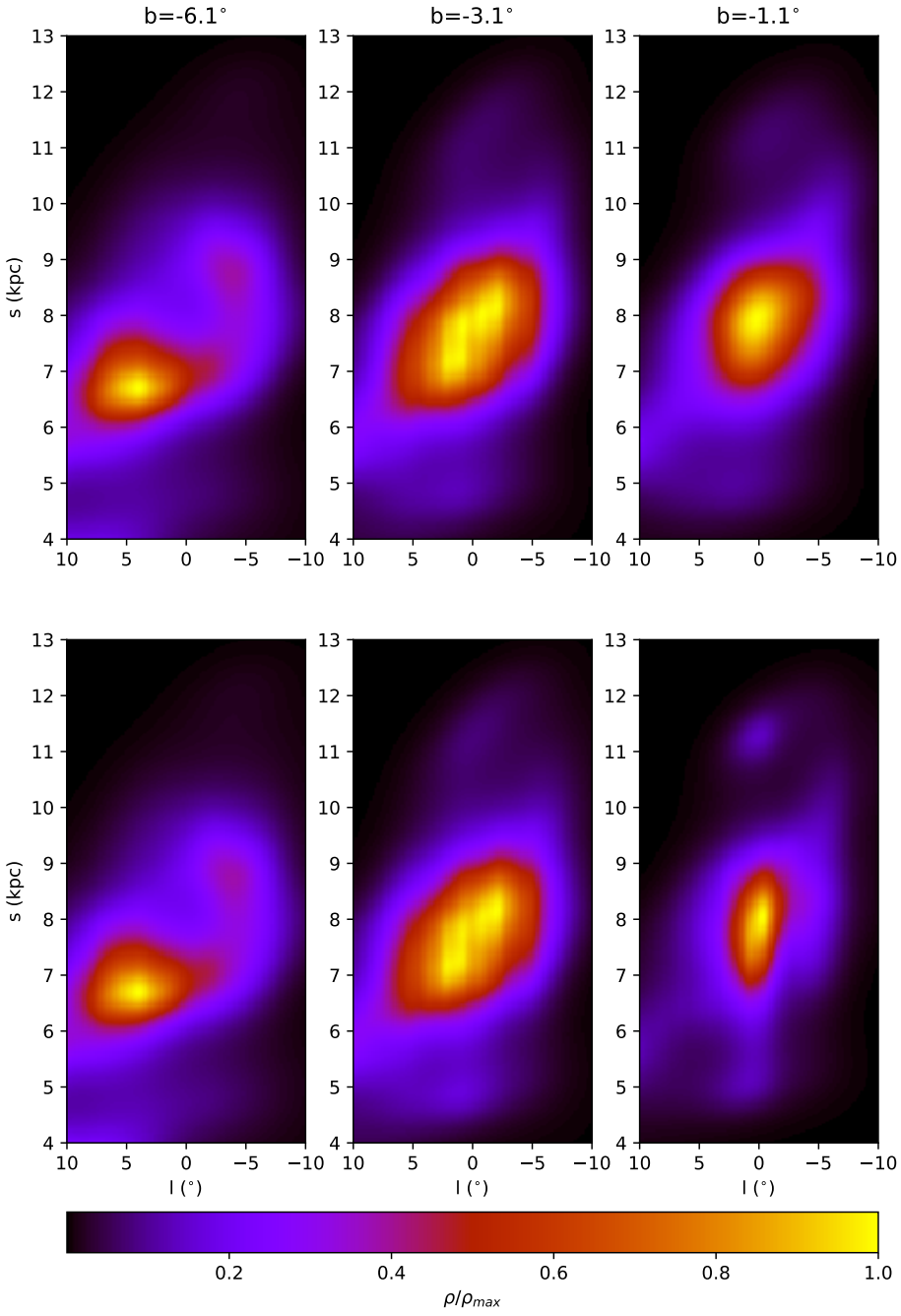

Fig. 2.31 Density reconstruction plots. The top three panels are for our standard mask shown in the right hand panel of Fig. 2.1 and the bottom three panels are for an alternative which masked out $|b| < 1^\circ$.

2.8 Conclusions

We have used a non-parametric method incorporating maximum entropy and smoothness regularisation to deconvolve the density distribution of bulge stars in the VVV MW-BULGE-PSFPHOT catalogue. We have also proposed a maximum entropy method for determining the background non-RC+RGBB stars, based on prior estimates using parametric models. Reasonable values for the regularisation parameters were found by testing the deconvolution method on a simulated stellar population of the Galaxy made of a 10 Gyr old eight-fold symmetric bulge, thin disc, and thick disc. Testing our maximum entropy deconvolution and background fitting method on a simulated population, we were able to nearly perfectly reconstruct the density even in the heavily extincted and crowded regions which had been masked in the analysis.

Applying the deconvolution method to the VVV data we found many of the features previously observed in the literature, including the X-shaped bulge from the split RC peak, the dependence of the viewing angle on the intrinsic RC luminosity dispersion, and the feature behind the bar. The R_0 gradient was not clearly seen in the MW-BULGE-PSFPHOT star counts when using the modified Richardson-Lucy deconvolution method assuming eight-fold symmetry.

We performed extensive systematic tests of the maximum entropy deconvolution method to test our assumptions regarding the choice of background model, metallicity distribution, intrinsic dispersion of the RC, position of the Sun above the Galactic mid-plane, and the deconvolution method itself.

The maximum entropy background was significantly preferred over the widely used exponential background by both the parametric models we fitted and the maximum entropy deconvolution method. Future studies of bulge star counts should be wary using the exponential background, as we have shown it has a tendency to over estimate the background star counts at the bright end of the luminosity function, causing the density of stars to be significantly underestimated at nearby distances.

A broad, unimodal metallicity distribution with spatially varying mean metallicity did not significantly affect the bulge stellar density. A bimodal metallicity distribution or greater is likely needed, which will become possible as the coverage of bulge spectroscopic surveys grows.

Qualitatively our results were broadly consistent with the modified Richardson-Lucy deconvolution of WG13. However, we were able to obtain less noisy and higher resolution reconstructions with our maximum entropy method when using the narrow RC dispersion which recent observations with *Gaia* have favoured (Hall et al., 2019;

Chan & Bovy, 2019). This resulted in somewhat less dense X-arms. Unlike this previous non-parametric approach, our method has built in inpainting for regions where the data was masked. This meant that we did not need to assume eight-fold symmetry to obtain a reconstruction of the whole bulge area.

From our fits to several different model cases, we found our bulge angle was in the range $[18°, 32°]$, our bulge mass was in the range $[1.3 \times 10^{10},\ 1.7 \times 10^{10}]M_{\odot}$, and our X-bulge contribution to the bulge was in the range $[18, 25]\%$. These are all compatible with other recent bulge estimates using the VVV data.

Our non-parametric method allowed us to inpaint masked regions and smoothly join onto a parametric model outside the region of the VVV data. This made it suitable for providing a template to be used in fitting the Fermi GeV Galactic centre excess. So our method both retains the broad trend as the bulge tapers as captured in a parametric model, while enhancing structural details present in the data at higher star count locations.

Relaxing the constraints applied to produce this model we investigated additional density features beyond the main bulge region. We observed a new morphological feature ~ 3 kpc in front of the bulge as a counterpart to the structure ~ 3 kpc behind the bar observed by Gonzalez et al. (2018) which they associate with the spiral arm. Though these features connect on opposite ends of the major axis of the bar/bulge, we found they were sensitive to the amplitudes of the AGBB and RGBB peaks, the impact of which we examined with strong systematic changes. There is room for further work on the characterisation of this feature within the current catalogues available. If we were able to simultaneously fit the luminosity function this would give us more confidence in the morphology of that feature by facilitating the data driven building of the AGBB and RGBB as represented by stars within the bulge. Future work may also include the application of deconvolution techniques to future surveys, which may recover this feature.

Chapter 3

Towards an Improved Model of the Galactic Centre Excess

3.1 Introduction

The Fermi GeV Galactic centre excess had previously been observed to present a spherically symmetric distribution attributable to origins such as the spherical distribution of dark matter (Goodenough & Hooper, 2009). In this chapter we present our working on improved modelling diffuse emission, determine the data driven preference for an excess that traces the stellar bulge rather than a spherical dark matter like model, then later improve on the stellar bulge modelling using the results of Chapter 2.

Gamma-ray emission above 100 MeV is dominated by diffuse emission, the main contributors of this emission are due to processes such as bremsstrahlung, inverse-Compton scattering and the decay of secondary particles such as π^0 from hadron collisions (Casandjian, 2015). The modelling of these components are crucial to the resolving of the GCE, where uncertainties in these diffuse emission mechanisms are significant in resolving the excess (Ackermann et al., 2017).

The interaction of cosmic-rays with the interstellar radiation field (ISRF) can lead to an up-scattering in energy of photons into the gamma-ray energy regime, called inverse-Compton scattering (ICS). For the purpose of ICS modelling, the ISRF may be broken into three main components: the cosmic microwave background, infrared light from dust, and starlight (Strong et al., 2000). The standard approach to modelling this component is solving the transport equation for cosmic-rays propagating through the ISRF. A popular code base for computing this component along with several other cosmic-ray emission components is the GALPROP code (Strong et al., 2010), which

solves the partial-differential-equation using the Crank-Nicolson method accounting for convection, diffusion, energy loss, nuclear fragmentation, and decay for cosmic-ray propagation (Strong et al., 2011). Their ISRF model was constructed using a composite construction of infrared emissivity distributions, spectral distributions, and luminosity functions drawn from several sources since no full ISRF function of the Galaxy was available before then (Strong et al., 2000). At the outset of the work in this chapter the only the ISRF models used in GALPROP were cylindrically symmetric, which was used in the construction of the Fermi Galactic Interstellar Emission Model. The GALPROP team later moved to 3D spatial models to account for Galactic structure such as the spiral arms (Porter et al., 2017). We refrained from attempting to improve on the GALPROP ICS modelling, and instead focused on improving the modelling of the the interstellar gas distribution.

The gas distribution in the Interstellar Medium (ISM) plays a dominant role in the production of π^0 particles decaying to produce gamma-rays, in addition to providing a medium through which cosmic-rays may produce gamma-rays via bremsstrahlung. Hydrogen accounts for 70% of the ISM mass, or 90% of the atomic content, in the form of neutral atomic and molecular, and ionised hydrogen, most of the remainder is helium with 28% mass contribution and heavier elements making up about under 2% of the mass (Ferrière, 2001).

Molecular hydrogen (H2), observable in the optical and UV bands is obscured by dust reddening, and unfortunately lacks emission lines in the radio spectrum (Ferrière, 2001). The 2.6 mm emission line of ^{12}C monoxide (CO) is used as a tracer molecule of H2 instead. The effectiveness of CO as a tracer of H2 is built on the established agreement between several methods of calibration based on different observations and physical principles resulting in relatively consistent conversion factors X_{CO} of $\sim 2\times10^{20}$ cm^{-2}(K kms^{-1})$^{-1}$ between the H2 gas column density and CO integrated line intensity, W_{CO} (Solomon & Barrett, 1991). However, X_{CO} has been observed to have a radial variation in the Milky Way, with an increasing X_{CO} with distance from the Galactic centre (Sodroski et al., 1995). Additionally, the X_{CO} conversion has been observed to vary with metallicity and the ambient radiation field intensity per nucleon, as observed in external galaxies (Israel, 1997), in which the metal content [O/H] has an observable radial dependence (Shaver et al., 1983; Smartt et al., 2001). In subsequent review, evidence of a conversion factor of order 3-10 times smaller than the recommended global value of $\sim 2\times10^{20}$, and physically motivated increase in the conversion factor in the outer Galaxy remains firm (Bolatto et al., 2013). On the assumption that cosmic-rays can freely penetrate molecular clouds, the gamma-ray regime has been used to fit X_{CO}

radially within a wider framework of gamma-ray modelling as constraints (Strong et al., 2004). By breaking our CO maps into Galactocentric annuli, we may implicitly fit the X_{CO} radial distribution as part of our gamma-ray analysis similar to Ackermann et al. (2012b). In regions of intermediate extinction $0.4 \lesssim A_V \lesssim 2.5$, CO becomes a weak tracer of H2, where CO is destroyed through photodissociation by far-ultraviolet radiation (Bolatto et al., 2013). This so-called "dark gas" component may be accounted for through fitting to dust thermal emission along with atomic hydrogen, as performed by Ackermann et al. (2012b).

The distribution of atomic hydrogen (HI) column density is typically traced by its 21 cm hyperfine emission line, its only ground state transition in the radio spectrum (Dickey & Lockman, 1990). Inferring the column density of HI requires a so-called spin temperature, T_S, the excitation temperature of the emission line defined by the Boltzmann equation (in which the rate of collision with other particles affects the defined temperature) (Field, 1959). The 21 cm absorption line has been used to estimate T_S and kinetic temperature T_k in the ISM, the result of the cold neutral medium (CNM) and warm neutral medium (WNM) kinetic temperature differential is spin temperatures ranging from about 25-70K in the CNM to ~ 1000 K in the WNM (Heiles & Troland, 2003). A T_S of 125K had frequently been adopted as the global constant temperature in 21 cm line, while Ackermann et al. (2012b) argue for a T_S of at least 150K to match the peak brightness temperature of the LAB survey. The impact of a globally adopted spin temperature is that bias is introduced for lines of sight where the spin temperature deviates from this value. These deficiencies are ameliorated through the dark gas modelling with dust reddening templates along with the molecular gas deficiencies as noted previously.

The less abundant helium and heavier elements which are not as easily observed, are assumed to be well mixed uniformly with the hydrogen distribution by the Fermi team in their diffuse emission models (Acero et al., 2016).

Ionised hydrogen (H_+) may be an important consideration in the modelling of gamma-ray emission, though is tricky to model due to the lack of direct observational markers. A template based on a warm ionised medium model by Gaensler et al. (2008) had previously been used by the Fermi team due to the apparent significance at high latitudes for diffuse gamma-ray emission (Ackermann et al., 2012b). By exploiting the dependence of radio pulsar dispersion measures and free electron density and the tracing of interstellar gas via extinction. He et al. (2013) found ionised atoms make up 10% of the atomic hydrogen column density in the ISM. However, Acero et al. (2016) found that in the construction of the Galactic Interstellar Emission Model (GIEM)

for point source analysis, the addition of an H_+ template did not improve their fit. Subsequently this template was dropped from the gamma-ray modelling pipeline. In our analysis, only atomic and molecular hydrogen distributions are directly modelled. The distribution of hydrogen in gamma-ray analyses is typically broken into Galactocentric annuli to be fitted separately. This approach assumes a uniform cosmic-ray (CR) density in each annulus. Fitting each annulus separately is implicitly accounting for radial variations in the CR density.

To create a comprehensive photon counts model of the Fermi-LAT observations with energy dependence, we employed the template fitting approach to modelling the GCE used by Casandjian (2015). The predicted counts of the total model for energy bin E takes the form:

$$\begin{aligned} N_{\rm pred}(E) = \sum_{\rm i=H\ templates} & N_{\rm H_i}(E)\widetilde{I}_{\rm H_i} + N_{\rm IC}(E)\widetilde{I}_{\rm IC_p}(E) + N_{\rm iso}(E)\widetilde{I}_{\rm iso} + N_{\rm LoopI}(E)\widetilde{I}_{\rm LoopI} \\ & + \sum_{\rm i=extend\ src} N_{\rm ext_i}(E)\widetilde{I}_{\rm ext_i} + \widetilde{I}_{\rm sun\_moon}(E) \\ & + \sum_{\rm i=point\ src} N_{\rm pt_i}(E)\widetilde{\delta}(i) + \sum_{\rm i=new\ templates} N_{\rm new_i}(E)\widetilde{I}_{\rm new_i}. \end{aligned} \tag{3.1}$$

Listed above are the components that will take part in our analysis. The tilde notation (e.g. $\widetilde{I}$) denotes an intensity map, I, which has been convolved with the energy dependent LAT point spread function (PSF) and corrected for instrument exposure and pixel solid angle for the time-frame and photon count binning used. The intensity maps remain constant, while the normalisations, N, for gamma-ray sources are fitted in the analysis. From beginning to end, these components correspond to the hydrogen gas distribution templates, inverse-Compton scattering, isotropic emission, Loop I, extended sources from the 3FGL, Sun and Moon contributions, point sources, and new extended emission templates. These new emission templates we discuss later include a nuclear bulge, a boxy Galactic bulge, an X-shaped bulge, the Fermi bubbles (FB), and dark matter.

With the template based approach we distinguish between the spherical dark matter morphology and stellar bulge morphology rather than make a ruling on the specific dark matter or bulge emission model itself. The interpretation of our results stems from the implications of the proposed spatially distributed structure best describing the excess in our analysis. A boxy stellar bulge distributed preference would be indicative of gamma-ray emitting sources such as MSPs spread through the Milky Way bulge and unlikely to be from the more spherically distributed dark matter annihilation scenario. We present our model preparation and results in this order: In Section 3.2 we present

our DFGB models constructed for the custom purpose of our Fermi excess analysis. We briefly describe the production of our dust correction templates in Section 3.3. Our Fermi Galactic centre excess analysis pipeline is outlined through Section 3.4. In Section 3.5 we apply our best fit parametric and non-parametric bulge models extracted from the VVV data in Chapter 2 using a similar analysis pipeline, following some methodology updates in Macias et al. (2019).

3.2 Modelling the Diffuse Galactic Background

We take two different approaches to modelling the gas distribution which gives us our large scale DFGB emission model for processes like bremsstrahlung and π^0 decay. First we have our faithful recreation of the diffuse interstellar emission annuli model assuming circular motion used by Ackermann et al. (2012b), allowing the adjustment of T_S and Galactocentric annuli segmentation as required (annuli construction is discussed further in Section 3.2.3).

This method has been used at least as early as Westerhout (1957) to reconstruct the hydrogen distribution in the Milky Way. We then construct a compatible annuli model using an iterative hydrodynamic gas deconvolution as in Pohl et al. (2008). For our molecular hydrogen model we use the CO emission line composite survey of Dame et al. (2001) in both annuli template constructions. For our atomic hydrogen model we use the Leiden/Argentine/Bonn (LAB) 21 cm line emission survey (Kalberla et al., 2005).

3.2.1 The Tangent Point Method

The crux of this deconvolution is converting the velocity of the gas tracer with respect to the local standard of rest ($V_{\rm LSR}$) with a Galactocentric distance R through the assumption of circular motion about the Galactic centre:

$$V_{\rm LSR} = \left(V(R)\frac{R_\odot}{R} - V(R_\odot) \right) \sin(l)\cos(b), \tag{3.2}$$

for orbital velocity $V(R)$, from an assumed rotation curve, observed in the direction (l,b), where $R_\odot$ is the distance of the Sun to the Galactic centre and $V_\odot$. The rotation curve used here was obtained from Clemens (1985), specifically the curve fitted for $R_\odot$=8.5kpc and $V_\odot = 220$km/s. The velocities from the measurement of Doppler shift in the emission lines of HI and CO are substituted into Eq. 3.2 and the equation is

solved for R. For this circular motion case there is no more than one radial solution for each $V_{\rm LSR}$. The non-circular motion of gas in the data sets results in some of the emission having forbidden velocities relative to the circular velocity curve. This was corrected for by placing gas of a velocity with an incorrect sign (relative to circular motion in that direction) in the local annulus, while gas exceeding the terminal velocity, given by V at $R = R_{\odot}\sin(l)$, is placed in the annulus containing this tangent point. Gas placed at a height too far above the Galactic plane, i.e. above the typical scale height of the gas distribution, is assumed to be local. Towards the Galactic centre and anti-centre Eq. 3.2 flattens out, resulting in a lack of the kinematic resolution required to place gas with this method. The solution in this method is to interpolate across $|l| < 10^{\circ}$ and $|180 - l| < 10^{\circ}$ for each latitude and annulus, using the average of gas in a range of 5° on either side of the 10° boundaries as the points with which the interpolation is performed.

The innermost annulus is entirely within the $|l| < 10^{\circ}$ boundary, so the column density distribution is estimated through velocity and interpolation-based prescriptions as performed in Ackermann et al. (2012b).

For CO, high velocity gas is placed in the innermost annulus using the limits:

$$V_{\rm LSR} < (-50 + 3l)\ {\rm km\,s^{-1}}, \tag{3.3}$$

and

$$V_{\rm LSR} > \begin{cases} 25\ {\rm km\,s^{-1}} & l < 0 \\ (10 + 3l)\ {\rm km\,s^{-1}} & l >= 0 \end{cases} \tag{3.4}$$

Whereas for HI, the distribution of the neighbouring annulus, of width $1.5 - 3.5$ kpc, is placed in the inner annulus ($0 - 1.5$ kpc) with 60% more gas content as a conservative estimate based on the observation of gas depletion in the $R \sim 1.5 - 3$ kpc Galactocentric annular region (Ferrière et al., 2007). The extent of the neighbouring annulus to the innermost one changes between works while retaining the 60% increase in the inner annulus (Ackermann et al., 2012b; Acero et al., 2016), we use the annuli extent used for *rbands_hi12_v5_hdeg_zmax1_Ts125.fits* packaged with GALPROP (Strong et al., 2011) (also used as a cross-check of our reproduction of this method).

For HI, the temperature brightness bins are converted to column density for an assumed spin temperature via:

$$N_{\rm H\,I} = -C\ T_S \int \ln\left[1 - \frac{T_B(v)}{T_S - T_c}\right] dv \tag{3.5}$$

using a constant microwave background brightness temperature for the continuum background $T_c = 2.66$ K, and truncating T_B to $T_S - 5$ K when $T_B > T_S - 5$ K. $C = 1.83 \times 10^{18} \mathrm{cm}^{-2} (\mathrm{K\ kms}^{-1})^{-1}$ is the line intensity to column density conversion factor (Wilson et al., 2009).

For H2 column density we have:

$$N_{\mathrm{H}_2} = X_{\mathrm{CO}} \times W_{\mathrm{CO}} \tag{3.6}$$

where the conversion factor X_{CO} is incorporated into our likelihood fit later. After deconvolution and interpolation, the annuli construction is renormalised so each line-of-sight preserves the total column density.

3.2.2 Hydrodynamic Method

By assuming circular motion everywhere, significant known features are missed in the placement of gas.

The Milky Way has a rotating bar with its major axis rotated from the Sun-Galactic centre line, and spiral-arm densities unwinding out through the Galaxy. If we have a model of the gaseous velocity distribution with non-circular motion induced by these structures, the forbidden velocities relative to circular motion should have an increased incidence of velocity-distance matches. By introducing these features to the gas deconvolution, the simplicity of the one-to-one relation between Galactocentric radius and Doppler shift velocity is lost. Although ultimately the reconstruction will be reduced to Galactocentric annuli, the radial placement, especially in the inner Galaxy, will likely be affected at a larger scale by non-circular effects. The approach we explore here and use for constructing our DFGB, pioneered by Pohl et al. (2008), involves the combination of Smoothed Particle Hydrodynamics (SPH) and iterative placement of gas at multiple distance solutions.

The velocity-distance relation for each longitude used as the basis of the deconvolution model applied later was the velocity field extracted from a SPH simulation performed by Bissantz et al. (2003). The potential used in this simulation was based on the three dimensional non-parametric model fitted to the COBE/DIRBE L-band data by Bissantz & Gerhard (2002) using dereddened maps produced by Spergel et al. (1996). This non-parametric model involved initially fitting parametric bulge, disc and spiral arm components to the L-band data. This parametric prior was subsequently voxelised and every voxel allowed to vary in a penalised likelihood fit to the same L-band data.

This cube was then embedded in the initial parametric model and decomposed in the Galactic plane into separate components via multi-pole expansion in Bissantz et al. (2003) to produce a spiral arm and bulge rotating potential in 2D. A SPH simulation was performed within this rotating potential, and best fitting models were decided based on the performance of their (l,v) diagrams compared to observations.

Armed with a Cartesian grid of particle velocities distributed about the Galactic centre, the non-circular motions of the barred inner Galaxy can be employed in an alternative deconvolution method, accounting for the multiple velocity-distance solutions that may turn up in the hydrodynamic model.

Circular motion was assumed outside the solar circle with a velocity V_0 of 210km/s. This was taken as a compromise between the faster velocities of approximately 220km/s as in Levine et al. (2006) for $R_0 = 8.5$kpc and a V_0 of 184km/s in Olling & Merrifield (1998). In addition, the velocity of the Sun relative to the LSR was subtracted from the LSR velocity, giving an effective velocity:

$$V_{\rm eff}(l,b,P) = V_{\rm LSR}(l,b) - V_{\rm LSR,\odot} \tag{3.7}$$

where $V_{\rm LSR}$ is taken to be:

$$V_{\rm LSR,\odot} = (10.\cos l\cos b + 5.2\sin l\cos b + 7.2\sin b)\ \ {\rm km\,s^{-1}}, \tag{3.8}$$

where the velocity was obtained by fits using main-sequence stars in the *HIPPARCOS* catalogue by Dehnen & Binney (1998).

The simulation velocity field was linearly interpolated onto the circular velocity outside the solar circle with a transition buffer between 7 and 9 kpc radially from the Galactic centre to construct our effective velocity field in Eq. 3.7.

Here, the molecular hydrogen specific deconvolution is discussed, while changes for atomic hydrogen mentioned afterwards.

A Gaussian with velocity dispersion about that of individual gas clouds, $\sigma_{\rm CO}$, centred at the peak velocity of the line signal is constructed:

$$I(v) = \frac{\delta W_{\rm CO}}{\sqrt{2\pi}\,\sigma_{\rm CO}} \exp\left[-\frac{(v-v_0)^2}{2\,\sigma_{\rm CO}^2}\right] , \tag{3.9}$$

which is subtracted from the line signal and placed in best fitting distance bins. Since the simulation can provide many distance solutions to the placement of gas of a given velocity, the gas was distributed over the eight best fitting locations, which were

determined using three weighting factors. A scale-height-based weight is employed:

$$w_z = \exp\left(-\frac{(z-z_c)^2}{2\,\sigma_z^2}\right) , \tag{3.10}$$

where z_c introduces a disc warping for distant radii from the Galactic centre, and σ_z accounts for flaring in the disc. For the molecular disc warp, Eq. 9.18 of Binney & Merrifield (1998) was used, while for flaring, an analytic approximation fitted to various observations by Pohl et al. (2008) was used. A Galactocentric Gaussian distribution w_r with a full-width half-maximum of 16.6 kpc was used to discourage gas being placed at very large distances from the centre. This limits excessive placement of gas at kinematically allowed distances that are unlikely. Lastly a Jacobian-based weighting, w_J, from transforming velocity into distance is used. We may define a distance interval from the Jacobian describing the spread over which distance bins the line signal should be placed:

$$\Delta_v D = \left|\frac{dv}{dD}\right|^{-1} \delta v , \tag{3.11}$$

where δv is the velocity interval. If the spread is less than the distance bin width, δD, that bin receives the entire portion, otherwise it is spread over the neighbouring bins. The Jacobian-based weight factor for these two cases may be defined as:

$$w_J = \frac{\delta v}{\delta D} \cdot \begin{cases} 1 & \text{for } \Delta_v D \leq \delta D \\ \frac{\delta D}{\Delta_v D} & \text{for } \Delta_v D \geq \delta D \end{cases} . \tag{3.12}$$

Gas with forbidden velocity is placed in the nearest match, except for significant deviation (more than 10 km/s) which is placed in the best matching distance in the Galactic centre region where non-circular deviations from the bar are expected to be significant.

For the 21-cm HI deconvolution, minor adjustments to this procedure were made, such as accounting for the broader line-width of individual clouds, and the more broadly distributed gas in scale, disc flare, and warp (Kalberla & Kerp, 2009; Delahaye et al., 2011). Absorption, self-absorption, and continuum were not corrected for in this modelling. As an extension of this method, we are currently working on accounting for continuum emission and apparent absorption lines in the HI 21-cm line.

For the HI gas distribution, a global spin temperature of 170 K was assumed for the Galaxy in deconvolution. There was also some minor interpolation of the distribution in the direction of Cassiopeia A and the Galactic centre.

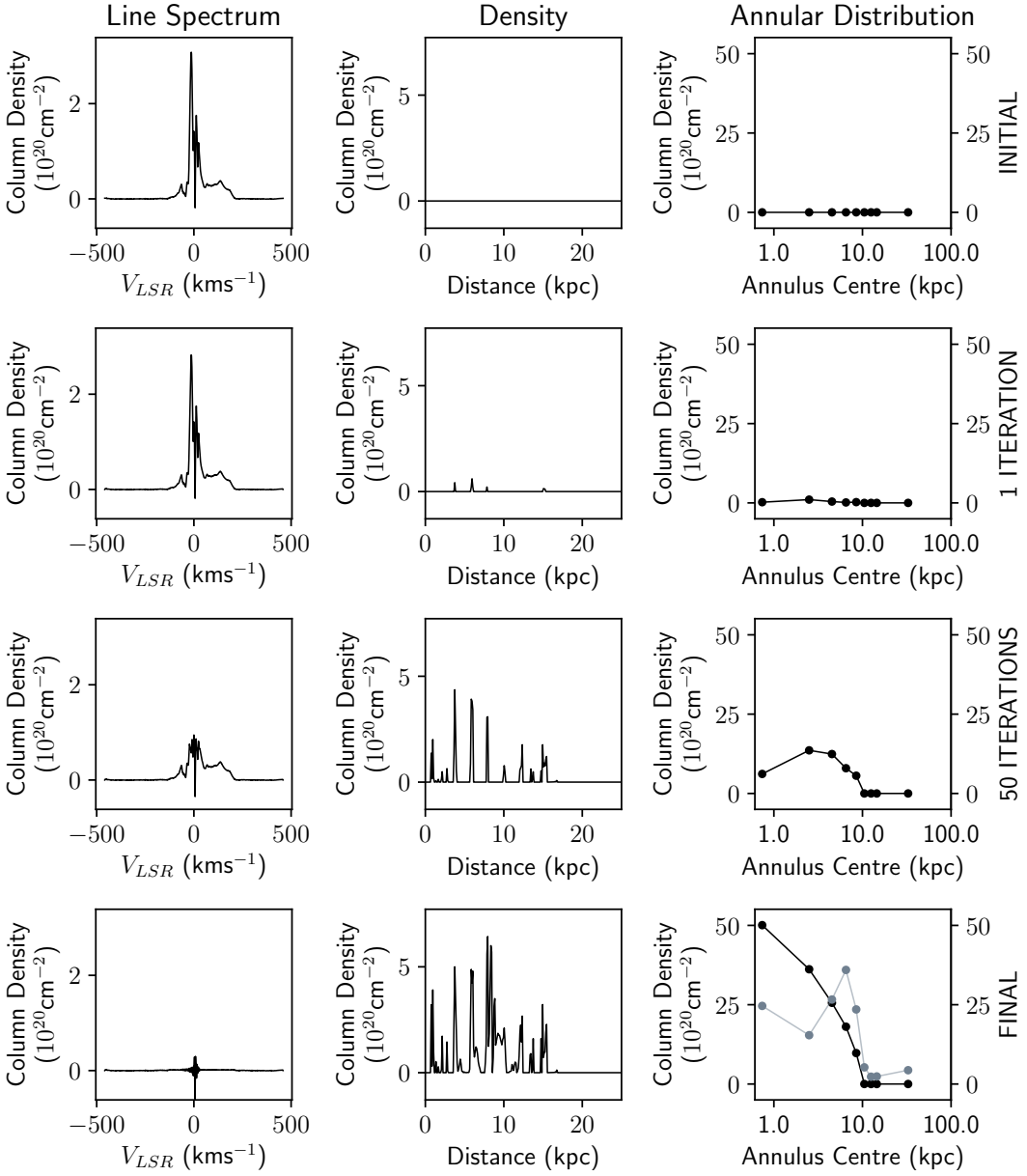

Fig. 3.1 Example deconvolution towards the Galactic centre, (l,b)=(0.5°,0°). The left column shows the line spectrum (converted to column density) at each step of the deconvolution, velocity in 1.03 kms^{-1} bins. The middle column is the placement of the line spectrum along the line-of-sight, in 100 pc bins. The right column is the distribution of the column density across annuli, unlike the middle column, this distance is cylindrical radius from the Galactic centre position. The grey data plotted in the bottom right corner over the annular distribution is the 9 annuli distribution packaged with GALPROP.

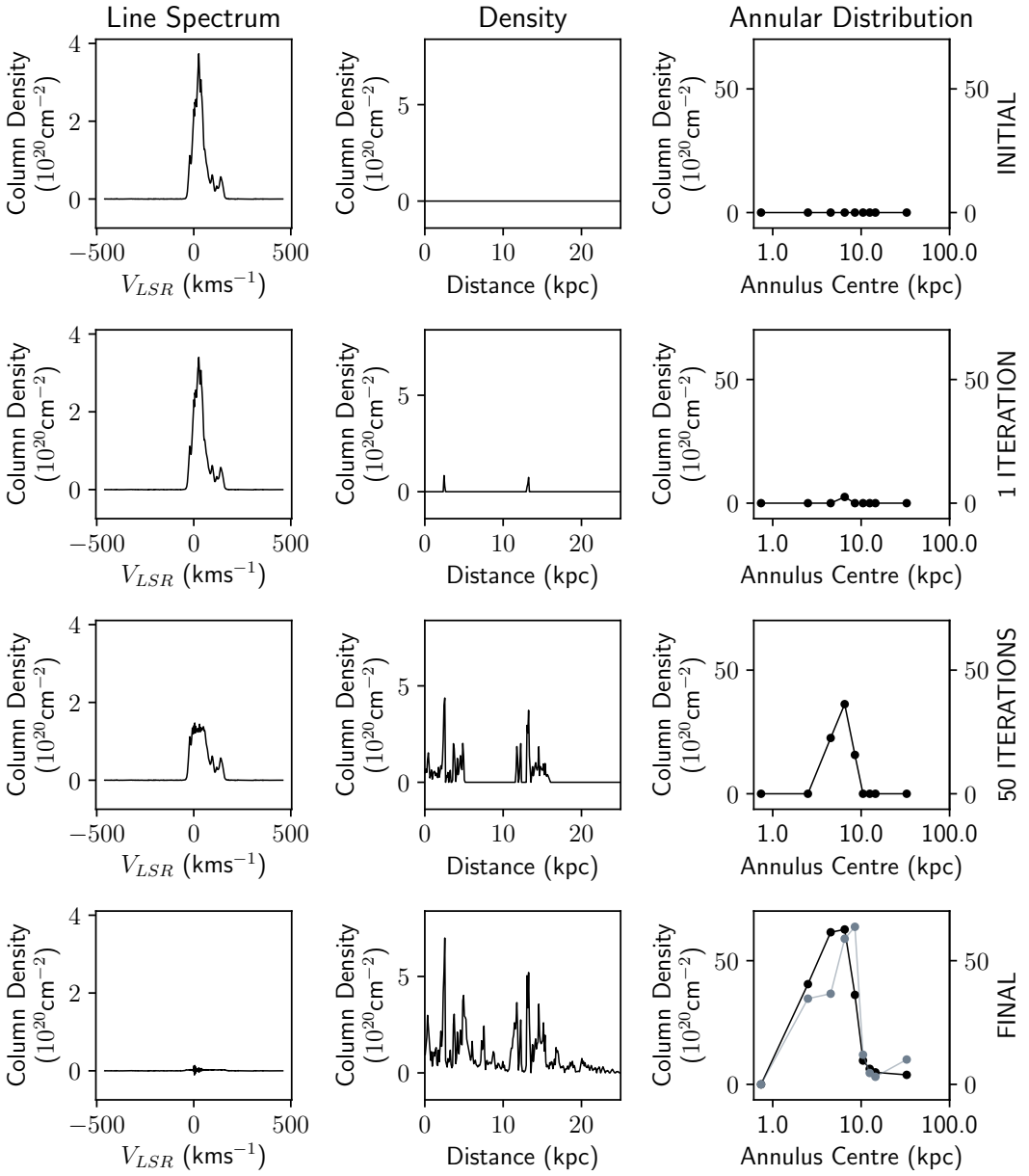

Fig. 3.2 Example deconvolution towards the Galactic centre, (l,b)=(15°,0°). The left column shows the line spectrum (converted to column density) at each step of the deconvolution. The middle column is the placement of the line spectrum along the line-of-sight. The right column is the distribution of the column density across annuli. The corresponding GALPROP HI annuli data is overlaid in grey on the bottom right.

In Fig. 3.1 and Fig. 3.2, example line deconvolutions are displayed. Though the gas placement is relatively sharply peaked, as can be seen in Fig. 3.3, the distribution, once pieced together, provides large scale structures resembling a barred spiral galaxy like the model of the Milky Way from which the velocity-distance relation was built. From Fig. 3.1 we can also see the distribution produces a fairly smooth decreasing density as a function of radius from the centre when binned into broad annuli. In Fig. 3.1, there is an apparent absorption feature near 0 kms^{-1}. This deconvolution method in the form presented here cannot handle absorption features, though we are currently working on modelling these features for a spatial column density reconstruction. Initial indications from this work are that these features do not have a particularly strong effect on the DFGB distribution relative to the bulge component. Fig. 3.2 shows how the method can select approximately two distance solutions which as a function of radius fall into effectively the same annulus, then proceeds to distribute the remainder of the signal across the line-of-sight with many different solutions. These two solutions may be two intersections of a spiral-arm-like component as may be seen in Fig. 3.3.

As a cross-check with other works, the HI annuli distribution packaged with GALPROP (Strong et al., 2011) (*rbands_hi12_v5_hdeg_zmax1_Ts125.fits*) using the tangent point method, is plotted over the final annular distribution from the iterative deconvolution method. The line-of-sight distribution in the GALPROP file was renormalised with the LAB data for a T_S of 170 K as done by Ackermann et al. (2012b) for comparable display. The nine annuli bins are defined by the boundaries (0, 1.5, 3.5, 5.5, 7.5, 9.5, 11.5, 13.5, 15.5, 50) in kpc. The bin mid-points are used for display. The distributions are reassuringly relatively similar away from the Galactic centre, such as in Fig. 3.2 between the two methods. While significant deviation in the inner annuli in Fig. 3.1 between the iterative hydrodynamic and tangent point methods occurs. The GALPROP maps exhibit a radial gas deficit in the $\sim 1.5 - 3.0$ kpc region as discussed by Ferrière et al. (2007). In these maps as in the Section 3.2.1 description, the innermost annulus is given the gas distribution of the neighbouring annulus across its extent, with a 60% increase in gas, acknowledging this deficit. From Fig. 3.3 some gas depletion around this region is visible, particularly in the HI figure. However, the gas placement due to non-circular motions from the bar and spiral arms, as towards the Galactic centre, place greater density proportions within this region that might otherwise end up being placed in more local annuli. The relatively large gas density in the inner two annuli in the hydrodynamic method compared to the GALPROP maps for the particular line-of-sight displayed in Fig. 3.1 would appear to be the result of this feature. The plotted annuli distributions are before any interpolation has been

applied, visible in Fig. 3.1 as a faster drop in gas near the local annulus and beyond due to a lack of kinematic resolution, while the GALPROP template has already been interpolated and renormalised there.

The Cartesian projection to surface density of the CO and HI deconvolutions are displayed in Fig. 3.3. The bar at an angle of ~ 20 deg to the Sun-Galactic centre line and winding spiral arms are clearly visible in this top down view. Marked with a dashed circle are the extrema of line-of-sight velocity if circular motion were assumed. As discussed by Pohl et al. (2008), this is where gas with high forbidden velocities will be matched to the nearest solution. These artefacts visibly diminish for longitudes $|l|< 20$, traced by the solid white lines, where larger velocity deviations line signal are distributed through best inner Galaxy distance solutions instead. Our ROI for our likelihood analysis with the Fermi data remains within this boundary so remains essentially unaffected by these artefacts in the density reconstruction for our work.

3.2.3 Annuli Maps

The anti-centre and outer annuli in the Galactic centre direction still lacked kinematic resolution in the iterative hydrodynamic method. Interpolation for $|l|> 160^\circ$ was applied to the anti centre, and in the Galactic centre direction interpolated for $|l|< 15^\circ$ for the outermost annulus in the CO case with the addition of the local annulus for HI which produced a significant gas deficiency in that annulus too. Since the iterative deconvolutions apply a prior weighting on the gaseous disc extent with warp and flaring for atomic and molecular hydrogen distributions, we leave gas positions as assigned rather than reassigning the gas if it falls outside certain limits as in the tangent point method.

We began our analysis with a division of our gas models into five annuli partitions bound by: (0, 1.5, 3.5, 8,10, 50) kpc, following the work of Ackermann et al. (2017). Our template analysis below resulted in unrealistic $X_{\rm CO}$ conversion factors for the innermost annulus. Combining the two innermost annuli to a single 0 to 3.5 kpc annulus returned equivalent results while giving more reasonable $X_{\rm CO}$ values for the inner Galaxy. These gas partitions are displayed in Fig. 3.4 for atomic and molecular hydrogen (via CO) for the two deconvolution methods we considered. The tangent point method based deconvolution approach constructed as in Section 3.2.1 was labelled "Interpolated" based on the innermost HI annulus morphology being entirely from interpolation as a significant feature, while the iterative deconvolution labelled "Hydrodynamic" after the SPH basis of its velocity-distance placement.

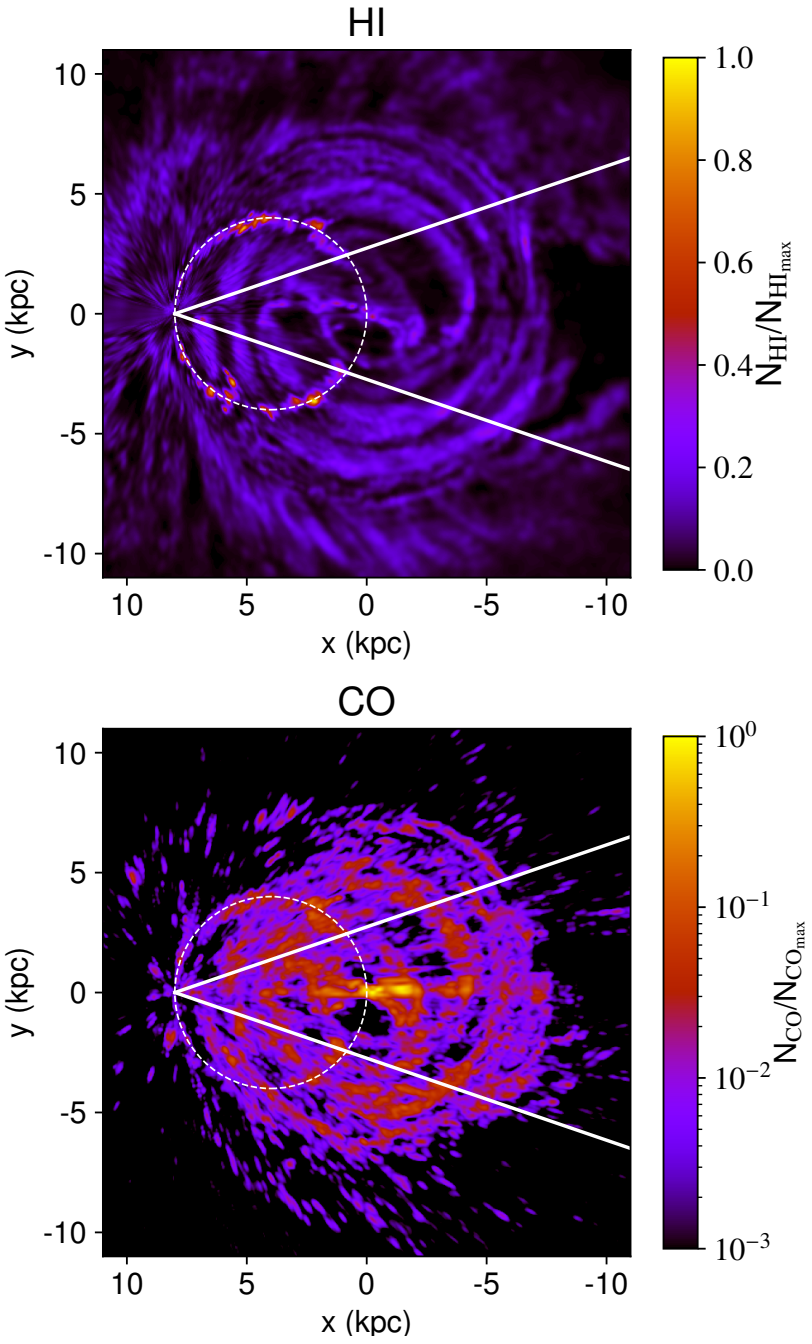

Fig. 3.3 Normalised surface density of the hydrodynamic maps. The density in the Galactic plane zeroed on the Galactic centre. The dashed circles trace the gas at forbidden velocities placed at approximately $R_0/2$. The solid lines enclose the $|l|<20$ region of the Milky Way in this projection. As the CO-H2 conversion is fitted radially in our gamma-ray analysis later, the relative CO density rather than H2 is displayed for reference.

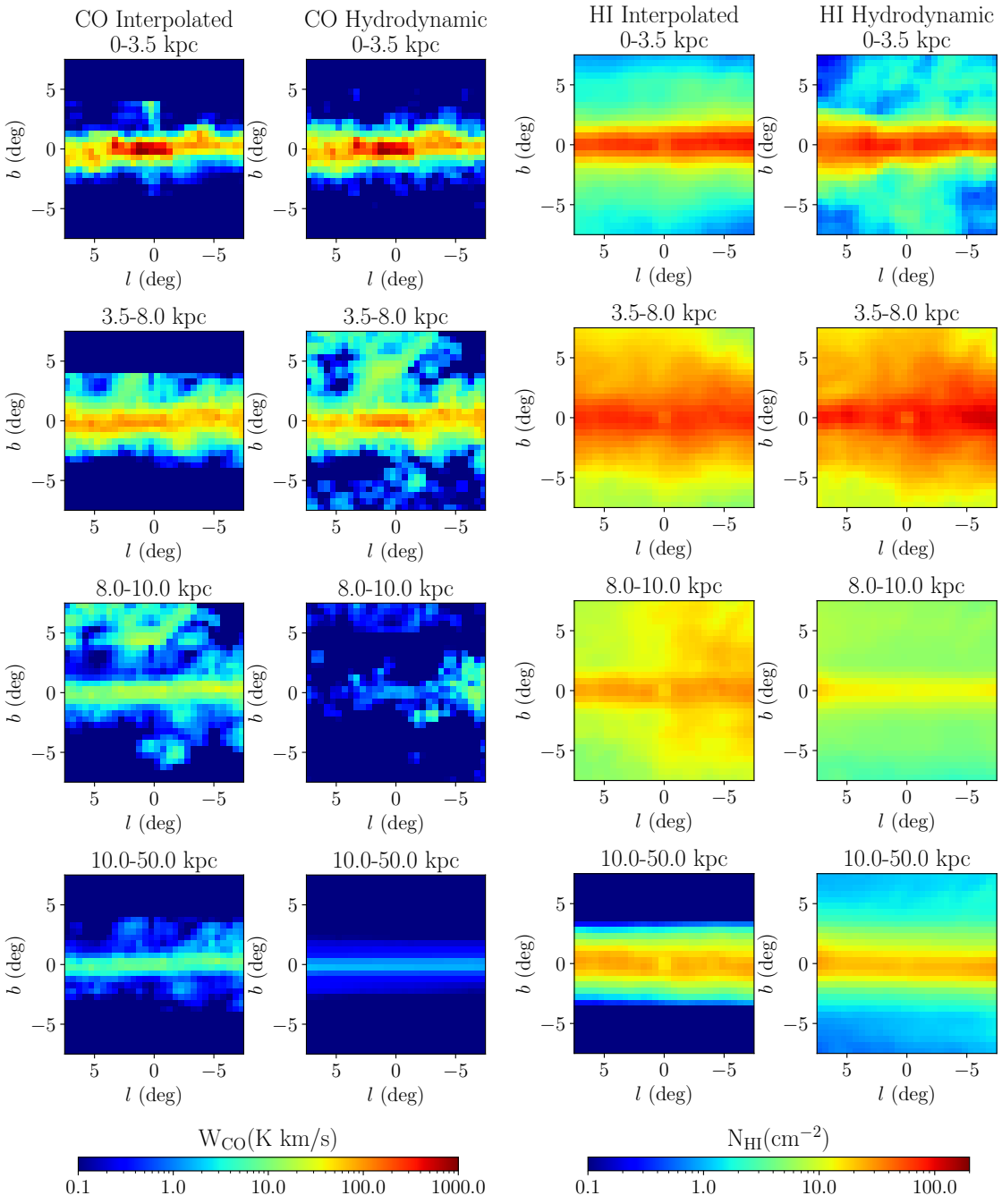

Fig. 3.4 Column density maps for the interpolated and hydrodynamic methods over our ROI. The minimum and maximum radii of each annulus is listed.

3.3 Dust Templates and the Dark Neutral Medium

Our HI and H2 maps can fail to account for hydrogen gas content due to several reasons (Grenier et al., 2005). When molecular hydrogen is not well mixed with carbon monoxide it will not be traced by the 2.6 mm CO emission, variation in the X_{CO} conversion factor can also contribute to mismatch in H2. Whereas the assumption of a constant spin temperature of $T_S \sim 170$ K for atomic hydrogen can result in significant deviations from the true spin temperature which varies spatially through the Milky Way. An alternative tracer of hydrogen is thermal emission from dust, provided as $E(B-V)$ reddening maps by Schlegel et al. (1998). Following the methods employed by Acero et al. (2016), we extracted the dust residuals resulting from the subtraction of a linear combination fit of N_{HI} and W_{CO} to the dust reddening map.

Fig. 3.5 displays the resulting hydrogen excesses and deficits along respective lines of sight for our hydrodynamic and interpolation-based gas models.

Negative residuals may be interpreted as an overestimate in T_S and X_{CO}, while positive residuals may be either an underestimate of these values or dark neutral medium. We employ a magnitude cut of 5 mag and higher to exclude regions that would contain a high density of emission from infrared point sources, to avoid overestimation of the dust correlated column density. The positive and negative residuals are split into separate templates to be fitted in the Fermi likelihood analysis.

3.4 Application of Bulge and Diffuse Models to the GeV Excess

3.4.1 Data Selection

We examined ~ 7 years of Fermi-LAT data Atwood et al. (2009) from August 4, 2008 to September 4, 2015 selecting Pass 8 ULTRACLEANVETO class events. We restricted our analysis to the 667 MeV to 158 GeV energy range and used the P8R2_ULTRACLEANVETO_V6 instrument response functions. To avoid contamination from terrestrial gamma-rays, we used events with zenith angles smaller than 90°. We restricted our ROI to $15^\circ \times 15^\circ$ centred about $(l,b) = (0,0)$ in Galactic coordinates and made no distinction between *Front* and *Back* events. Employing the `gtmktime` tool we selected the recommended data filters (DATA_QUAL>0)&&(LAT_CONFIG==1). Spatial binning was performed with the `gtbin` utility with which we divided the LAT

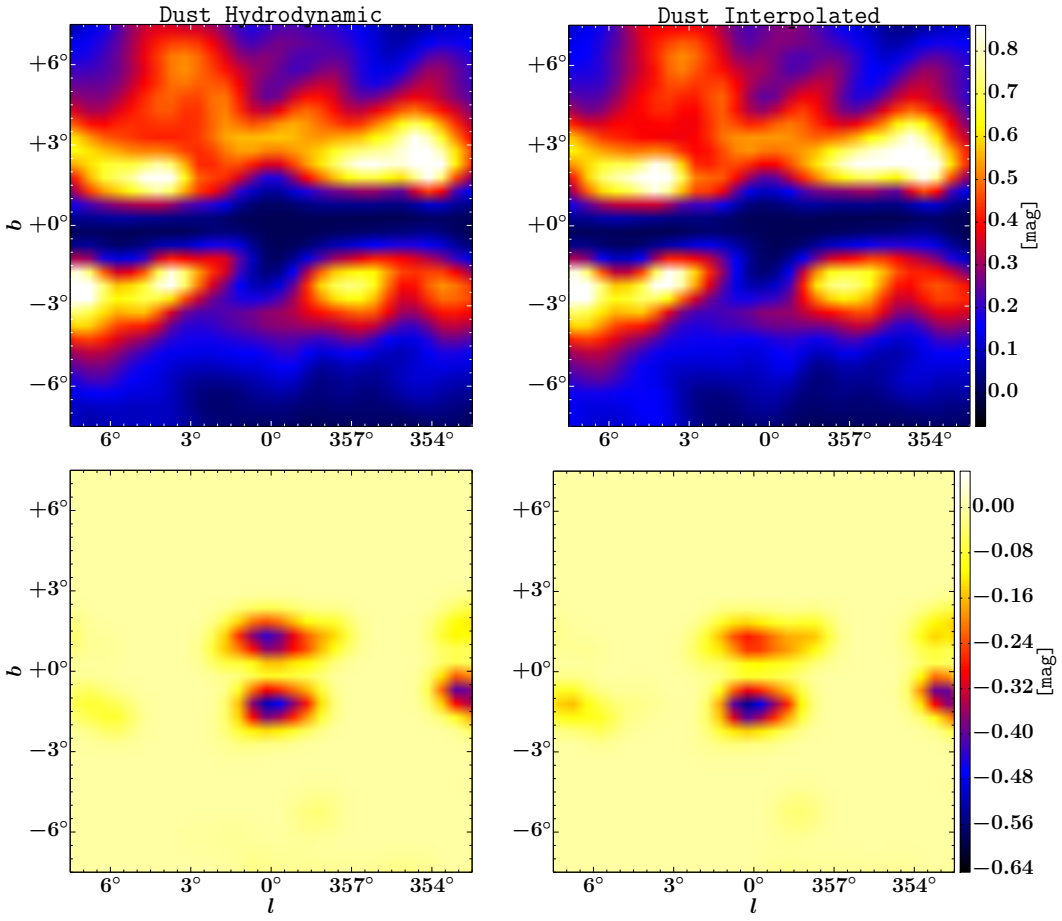

Fig. 3.5 Dust reddening E(B-V) positive (top) and negative (bottom) residual maps. The left (right) hand side maps were based on fitting the hydrodynamic (interpolated) HI and CO maps to the E(B-V) reddening map which had be a magnitude cut of 5 mag and higher. For display purposes, Gaussian smoothing with a radius of 0.5° was performed.

data into 150×150 angular bins of size 0.1° in a `CAR` sky projection. For all analyses in this chapter we used version `v10r0p5` of the Fermi Science Tools package.

3.4.2 Emission Templates

Our atomic and molecular hydrogen templates with corresponding dust correction templates can adequately describe bremsstrahlung and π^0-decay components of our Fermi template fitting. In addition to these, we employed a range of templates and point source contributions to describe potentially significant gamma-ray contributors. For

our baseline analysis we fitted an inverse-Compton template, Sun and Moon emission templates, an isotropic component, the 3FGL sources in the ROI, and a model for the Loop I structure described later in this section. After determining the statistically preferred gas modelling approach (performed in Section 3.4.4), the hydrodynamic gas templates and corresponding positive and negative dust residual templates were added to this baseline.

For our analysis which compares the two hydrogen gas distribution approaches, we utilised an ICS template generated by the authors of Ackermann et al. (2012b) using GALPROP v54.1 (Strong et al., 2011). In particular, we used the model generated by the GALDEF file `galdef_54_Lorimer_z10kpc_R20kpc_Ts150K_EBV2mag` for this analysis. This diffuse emission model generated provided an energy dependent spectrum for ICS we could interpolate to our energy binning scheme. The morphological distribution narrows in height and broadens along the plane with increasing energy as the proportion of IRSF contributions change. The ICS distribution around the GCE energy peak, using ~ 3 GeV is displayed in Fig. 3.6, along with the ICS distribution around the upper limit of our energy bin range.

To account for the large scale non-thermal diffuse emission structure dubbed Loop I investigated in Wolleben (2007), we generate a template using their parametric description. This structure proved to be important in the modelling of the Fermi bubbles by Ackermann et al. (2014) due to the overlap of these two features. We adopt the same parametrisation as their work in our analysis. The geometric model of Loop I assumes uniform synchrotron emission from a foreground feature takes the form of two spherical shells with a prescribed wall thickness, located relatively nearby for this work, at distances of 78 and 95 pc. Line-of-sight integration of these uniform shells results in an overall non-uniform emission on the sky. The integrated intensity from these shells is displayed in Fig. 3.6.

To account for diffuse emission originating from the Sun and Moon we used the `gtsuntemp` tool (Johannesson & Orlando, 2013), generating models for the data selection we made.

For isotropic emission, we use the model provided by the Fermi team for our photon selection and data set (`iso_P8R2_ULTRACLEANVETO_V6_v06.txt`).

Once our baseline templates were selected (via Sections 3.4.3 and 3.4.4), we fitted several additional extended emission templates through our likelihood analysis: an X-bulge, a boxy bulge, Fermi bubbles, nuclear bulge, and a dark matter model. We also consider new point source candidates which are combined in the later template fitting procedure to gauge their likelihood impact.

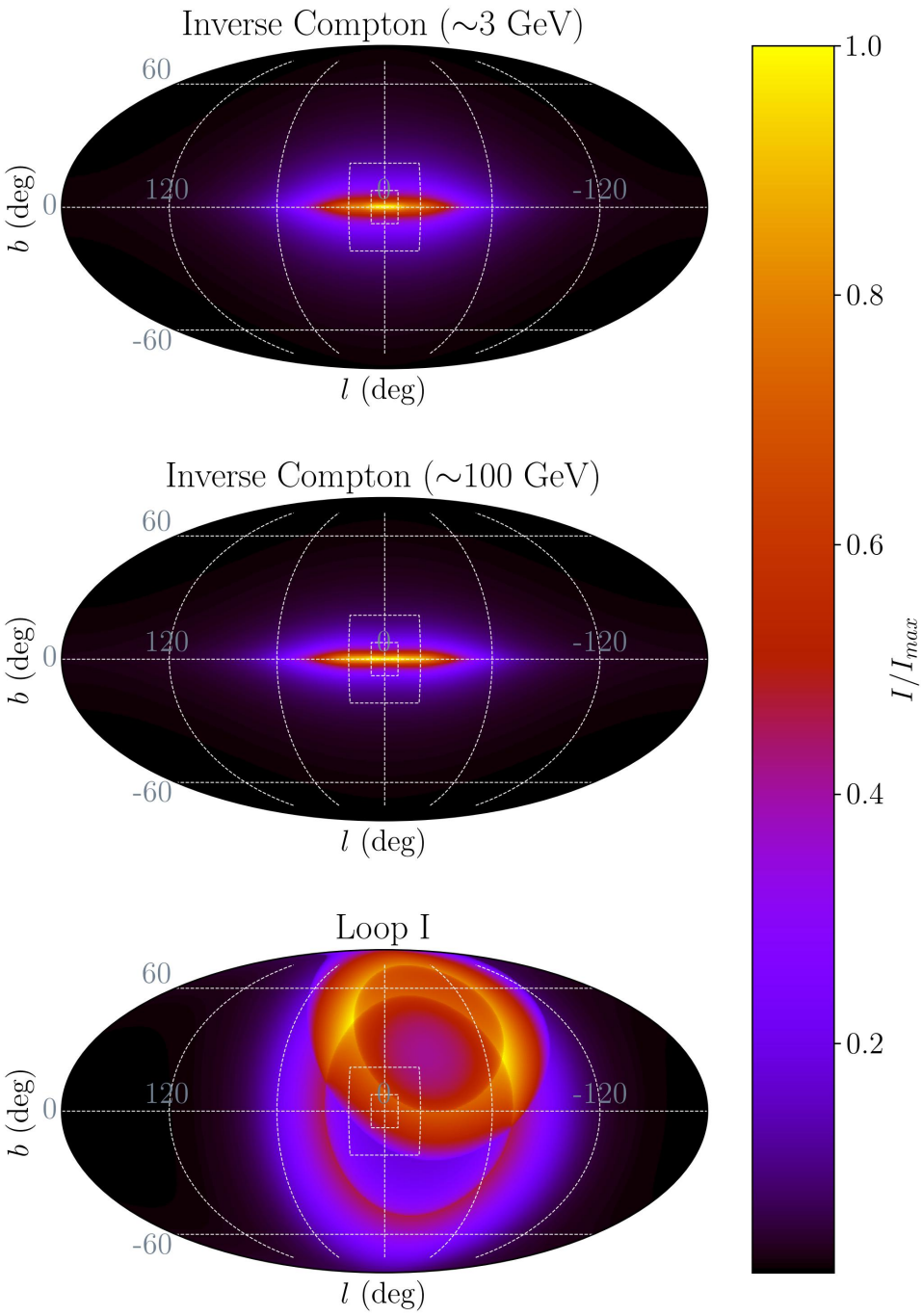

Fig. 3.6 Mollweide projection of the Loop I and inverse-Compton models, normalised to the peak values of the intensity before exposure and PSF correction is applied. Marked by dashed boxes in the central region are the $15^\circ \times 15^\circ$ and $40^\circ \times 40^\circ$ regions of interest used in this section and the following section respectively.

The X-bulge was extracted from the WISE data by Ness & Lang (2016) producing two maps corresponding to the two WISE bands (3.4 micron $W1$ band and 4.6 micron $W2$ band). We reproduced their model by fitting and subtracting an exponential disc model from each image, masking negative flux and applying a median filter of radius 1.7° for smoothing. Values below zero were set to zero and the average of the two maps was taken to produce our template.

For our boxy bulge template we integrate the best fit S-model (Eq. 2.35) from Freudenreich (1998) which had $R_0 = 8.5$ kpc and used their primary mask. This model was obtained by fitting parametric dust, disc, and bulge models to dereddened J, K, L, and M band COBE/DIRBE emissivity images simultaneously. We refer to this template as F98S from here.

To account for the Fermi bubbles we used the catenary curves fitted in Acero et al. (2016). These curves trace the boundary of the bubbles, taking the form $10.5° \times (\cosh((l-1°)/10.5°)-1°)$ and $8.7° \times (\cosh((l+1.7°)/8.7°)-1°)$ for the Northern and Southern bubbles, respectively. In this model the integrated intensity within these bounds is assumed to be uniform, as displayed in 3.7 for our ROI.

Our nuclear bulge model was constructed by Nishiyama et al. (2013), where a best fit Galactic disc component was subtracted from the near-infrared stellar density measured by the SIRUS camera, producing a central nuclear bulge component for the Galactic centre region of $|l| \leq 3°$ and $|b| \leq 1°$. All pixels with fewer than 15 stars per arcmin^2 were set to zero to remove artificially sharp boundaries caused by survey patches.

We use the generalised NFW profile for our dark matter template:

$$\rho(r) = \frac{\rho_\odot}{\left(\frac{r}{R_\odot}\right)^\gamma \left(\frac{1+r/R_s}{1+R_\odot/R_s}\right)^{3-\gamma}}, \tag{3.13}$$

with profile slope $\gamma = 1.2$, scale radius $R_s = 23.1$ kpc, local density $\rho_\odot = 0.36$ GeV/cm^3, and Sun to Galactic centre distance $R_\odot = 8.25$ kpc. The square of the halo profile was integrated along the line-of-sight to produce the needed flux template. This model has proved to be a good fit in previous works, (Hooper & Linden, 2011; Abazajian et al., 2014; Daylan et al., 2016), so we consider this parameterisation of dark matter to be a fair representation in our analysis.

Lastly, we constructed a model of potential new point sources not in the 3FGL, this component of our work predating the release of 2FIG (Fermi-LAT Collaboration, 2017). The computational feasibility within this pipeline relied on our ROI being limited at

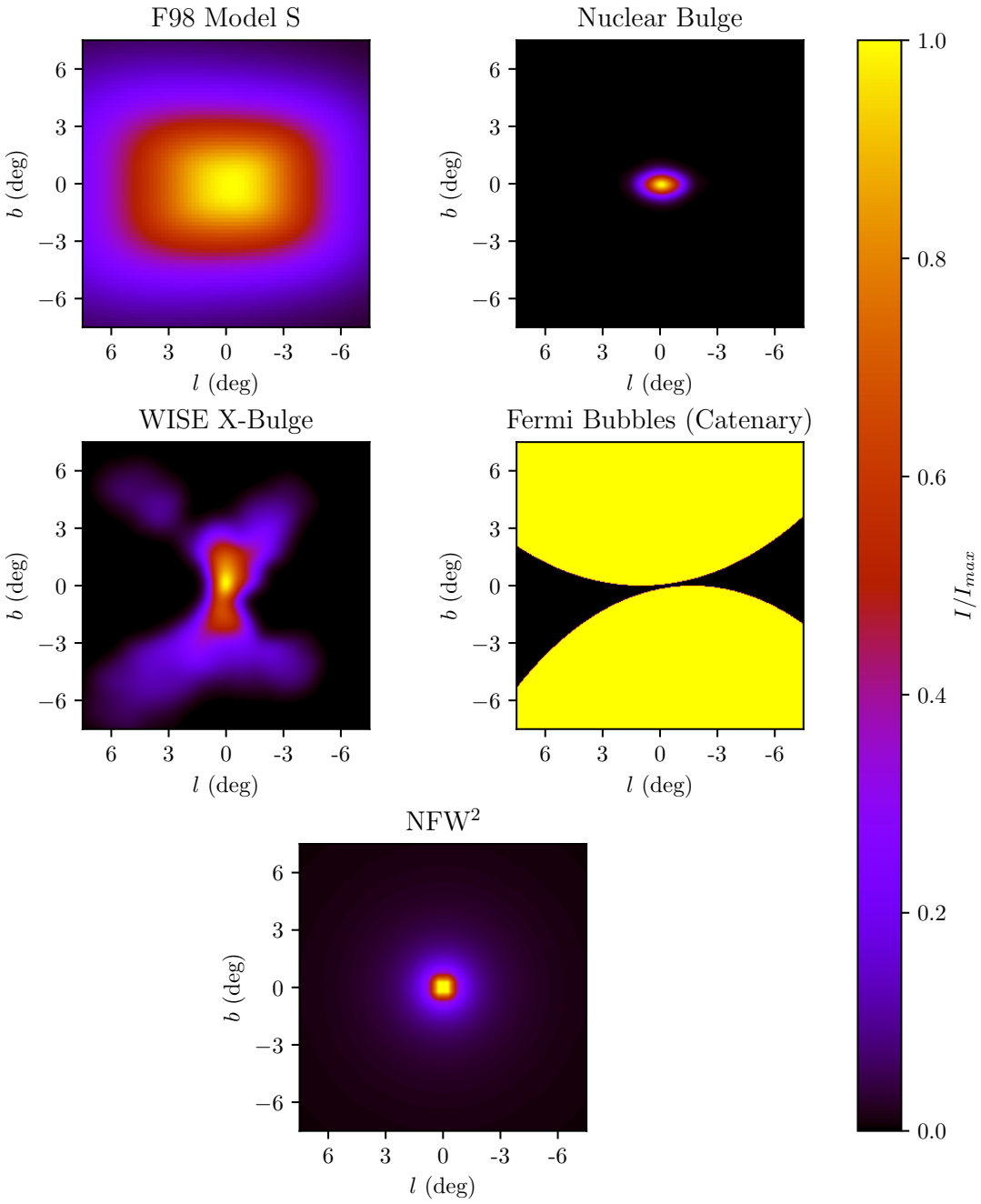

Fig. 3.7 Extended emission templates compared in our likelihood analysis. The F98S model uses the best fit parameters from Freudenreich (1998) for $R_0 = 8.5$ kpc and "primary mask". The nuclear bulge and X-bulge have been smoothed with a Gaussian of 0.3° for display. The FB template is a bounded region enclosed by catenary curves so everywhere within the region normalises to 1 here. The dark matter profile was produced from integrating the square of the dark matter halo density.

$15^\circ \times 15^\circ$. Starting with the baseline model, a trial point source was placed in the centre of each pixel of the binned data, with power-law spectrum with a slope of two. A test statistic (TS) map for each energy bin was computed and combined to produce a total TS map.

We enforced a 4σ detection threshold on these point source candidates. For a global analysis with three parameters for the spectrum and position, this would correspond to a threshold of TS=25. However, for a bin-by-bin analysis with non-negativity conditions on the amplitude, the equivalent p-value in computing the σ detection takes on a mixture distribution as we shall derive here, in the process we also acquire the mixture distribution form later applied for our extended emission templates.

Wilks' theorem states that the asymptotic distribution of a TS is given by the Chi-squared distribution (χ^2_q), where q is the number of new parameters. This can be used to evaluate a p-value $[1 - p(\mathrm{TS} > \mathrm{TS}_{\mathrm{thresh}})]$ of some threshold TS value, above which the new parameters are accepted as being statistically significant. However, this theorem does not hold if any of the null values of the new parameters are on the boundary of the allowed parameter space. This is problematic in the case of deciding whether or not there is a new source in the data which can only have a non-negative amplitude. This limitation can be alleviated using the Chernoff theorem of Chernoff (1954), which implies that if the new parameter is the proposed source's amplitude then the TS distribution will be given by a mixture distribution:

$$p(\mathrm{TS}) = \frac{1}{2}(\delta(\mathrm{TS}) + \chi^2_1(\mathrm{TS})). \tag{3.14}$$

where δ is the Dirac delta function. This formula just states that under the null hypothesis, half the time the evaluated amplitude will be negative (in which case TS is assigned) and the other half of the time (when the amplitude is non-negative) the distribution will follow from Wilks' theorem. This method was shown to work well for simulations of EGRET data by Mattox et al. (1996). They also proposed that an extension which includes parameters for the two dimensional position of the source has a distribution of

$$p(\mathrm{TS}) = \frac{1}{2}(\delta(\mathrm{TS}) + \chi^2_3(\mathrm{TS})) \tag{3.15}$$

which they checked is correct by comparing to simulated EGRET data.

In some cases, sources have been found to significantly prefer a curved spectrum (Acero et al., 2015). For example, pulsars generally have an exponential cut-off spectrum. Therefore, it may be preferable to test for some new source with a non-parametric

spectrum so as not too cause any bias by using a spectrum different from the spectrum the source has. This can be done by doing a bin-by-bin analysis where the energy range is broken up into a number of bins. If the bins are made sufficiently small, then a power-law with Γ set to some fixed value (such as 2) can be used in each bin without loss of generality. Although, the bins should not be too small otherwise one starts to get correlations between the different energy bins due to the finite energy dispersion of the Fermi-LAT instrument (Ackermann et al., 2012a). For the case of testing for a new source with fixed position, we can use $\mathrm{TS} = \sum_{i=1}^{n} \mathrm{TS}_i$ where TS_i is the TS for bin i and there are n bins. We can then utilise the formula given in case 9 of Self & Liang (1987), which translates to:

$$p(\mathrm{TS}) = 2^{-n} \left(\delta(\mathrm{TS}) + \sum_{i=1}^{n} \binom{n}{i} \chi_i^2(\mathrm{TS}) \right) \tag{3.16}$$

where the amplitude in each energy bin needs to be non-negative, and $\binom{n}{i}$ is a binomial coefficient. This equation has a simple interpretation in terms of mixture distributions. The 2^{-n} term is equal to the number of distinct ways n bins could have a non-negative or negative best fit amplitude. As there is only one way they could all have a negative amplitude, that is the weight of the δ function. While if the there are i non-negative amplitudes, they would have $\binom{n}{i}$ distinct configurations and each of these configurations would have a χ_i^2 distribution. We used Eq. 3.16 in estimating the TS significance of our extended emission templates.

When testing for new point sources, the two position variables of the proposed new point source should also be included. They are not on the boundary of the allowed range under the null hypothesis. Case 9 of Self & Liang (1987) also covers the case where n of the new variables are restricted and two are not:

$$p(\mathrm{TS}) = 2^{-n} \left(\sum_{i=0}^{n} \binom{n}{i} \chi_{i+2}^2(\mathrm{TS}) \right), \tag{3.17}$$

where χ_{i+2}^2 is a χ^2 distribution with $i+2$ degrees of freedom. However, this formula is not quite the one we are looking for, as when all the bins have non-positive best fit amplitudes we need to have $\mathrm{TS} = 0$ regardless of the values of the position variables. Therefore, in order to modify Eq. 3.17 for our case of interest, we need to subtract off $2^{-n}\binom{n}{0}\chi_2^2 = 2^{-n}\chi_2^2$ and add on a $2^{-n}\delta(\mathrm{TS})$ term. This produces the following equation

for gauging our point source significance:

$$p(\mathrm{TS}) = 2^{-n}\left(\delta(\mathrm{TS}) + \sum_{i=1}^{n}\binom{n}{i}\chi^2_{i+2}(\mathrm{TS})\right) \tag{3.18}$$

To work out the number of σ of a detection we evaluate the equivalent p-value for one new point source as per Wilks' theorem (Wilks, 1938):

$$\text{Number of } \sigma \equiv \sqrt{\mathrm{InverseCDF}\left(\chi^2_1, \mathrm{CDF}\left[p(\mathrm{TS}), \hat{\mathrm{TS}}\right]\right)} \tag{3.19}$$

where CDF and InverseCDF are the cumulative and inverse cumulative distribution functions respectively. For a 4σ detection, the TS threshold is now 41.8, using this distribution. Pixel clusters above this detection threshold, while proving to be reasonably isolated from other pixel clusters under visual inspection, were taken as potential source candidates, where the source position was taken to be a weighted average of each pixel coordinate in the cluster by their TS value.

In sets of 10 point sources from brightest to dimmest (segmented like this to reduce source confusion effects) the sources were fitted simultaneously with the baseline model using the binned likelihood analysis described below in Section 3.4.3, retaining sources with a TS above the detection threshold. In total, 64 new point source candidates remained from this procedure. Performing the analysis below with the 2FIG catalogue once released as a systematic check did not qualitatively change our conclusions.

3.4.3 Binned Likelihood Analysis

We split the data into 19 logarithmically spaced energy bins then performed a maximum likelihood fit for each energy bin separately using the `pyLikelihood` tool. The choice of binning was constrained by trying to keep the bins narrow enough that the spectral components of the emission templates could be approximated by a power-law while also being larger than the Fermi-LAT energy resolution. Once the bin-by-bin method had converged, the inferred spectrum of each source was either fitted by a power-law or an exponential cut-off model. When energy bins had $TS < 1$ or $\Delta F_i/F_i > 1$ they were combined with adjacent energy bins until $TS > 1$ and $\Delta F_i/F_i < 1$.

The errors from the bin-by-bin fit were added in quadrature to the errors caused by the uncertainties in the effective area (Acero et al., 2015). These effective area errors were taken to be f_i^{rel} times the predicted flux for bin i. Where f_i^{rel} is interpolated from the values given in Acero et al. (2015). The spectrum was modelled by an exponential

cut-off if

$$\mathrm{TS}_{\mathrm{curvature}} \equiv 2\left(\log \mathcal{L}(\text{exp. cut-off}) - \log \mathcal{L}(\text{power-law})\right) \geq 9 \tag{3.20}$$

where $\mathcal{L}(i)$ is the maximum likelihood value for model i. This threshold of 9 corresponds to a 2σ difference between the models if equality is met (applying Wilks' Theorem for one new parameter (Wilks, 1938)).

3.4.4 Comparison of Diffuse Emission Models

Before fitting our new templates we identified the most suitable gas template to use in the optimisation. We performed a scan of the likelihood difference between using our interpolation and hydrodynamic gas templates for successive energy bins, displayed in Fig. 3.8. First we fit a model to the Fermi-LAT data comprised of the 3FGL catalogue of point sources (Acero et al., 2015) along with models of the extended sources HESS J1825-137, RX J1713.7-3946, W28, and W30, incorporated from an expanded ROI to account for photon leakage. We then fit these sources simultaneously with our diffuse components described above, fixing the normalisation for the Sun and Moon template fluxes. Summing the likelihood differences between the gas models across energy bins gives $\mathrm{TS}_{\mathrm{Hydrodynamic}} = 2 \times 1362$, where $\mathrm{TS}_{\mathrm{Hydrodynamic}} = \sum_i 2(\log(\mathcal{L}_{\mathrm{Hydrodynamic}_i}) - \log(\mathcal{L}_{\mathrm{Interpolation}_i}))$ for energy bins, i, favouring the hydrodynamic templates which we use for the remainder of this analysis. Though the aggregate TS favours the hydrodynamic templates, this approach to gauging the difference is just a rule-of-thumb guide.

3.4.5 Emission Template Fitting Procedure

Building on our baseline model we evaluated the TS for each of our new templates. Employing the bin-by-bin approach, we fitted the gamma-ray emission to derive spectral model independent fluxes for each template in an energy bin. We use a power-law with spectral index of 2, though the narrow bins mean the results are not sensitive to this index choice. Within each energy bin all point source and included extended template amplitudes were fitted simultaneously.

The template with the greatest improvement to the likelihood was added to the baseline and the remaining new templates were evaluated on top of the new base. Each new template has $n \times 19$ parameters for an integer n. We iterated through this process until the highest TS for a new template was below a 4σ threshold. For a single new

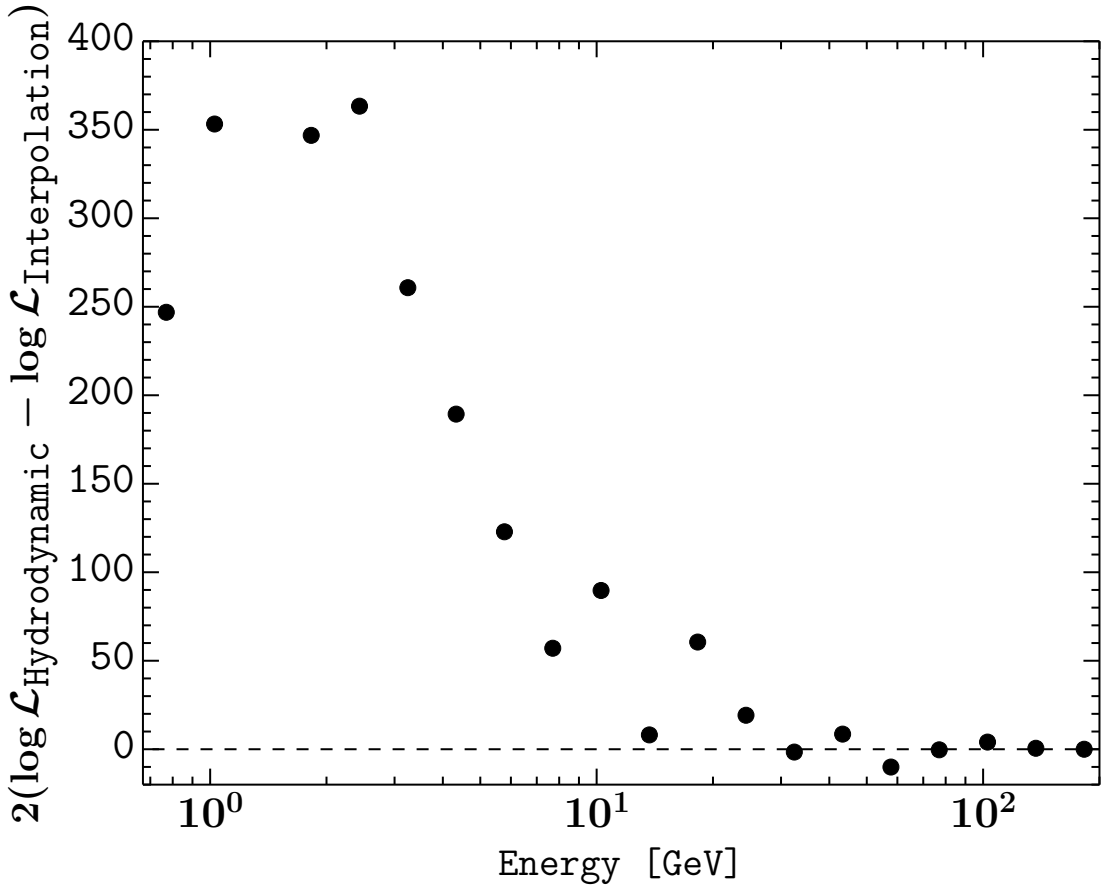

Fig. 3.8 Comparison of the log-likelihood obtained for two different interstellar gas models. The likelihood is compared for hydrodynamic (Pohl et al., 2008) gas maps vs the interpolation ones used in the standard Galactic diffuse emission model. Summing over the energy bins gives $\mathrm{TS}_{\mathrm{Hydrodynamic}} = 2 \times 1362$.

extended emission template, with 19 amplitude parameters across the energy bins, this corresponds to TS<38.4, inferred using Eq. 3.16 and Eq. 3.19.

3.4.6 Results

The results of our maximum likelihood analysis are listed in Table 3.1. The baseline model with new point sources, an X-bulge and a nuclear bulge provided the best fit to the gamma-ray data through our extended template selection pipeline, though this result later changed to a preference for the F98S model when the ROI was expanded to $40^\circ \times 40^\circ$. Depending on the order the nuclear bulge and X-bulge were fitted, the X-bulge provided a $16.1-18\sigma$ improvement to the total likelihood applying Wilks' theorem. This result does not indicate a detection of this bulge template at this significance over any other model, but rather the improvement to the likelihood over not adding any new component. The intention being to explore the use of the Galactic bulge as a tracer of the GCE as an alternative to dark matter.

The best fitting spectral parameters of our templates were found using χ^2 fits to the inferred flux points from each energy bin. A power-law with exponential cut-off ($dN/dE \propto E^{-\Gamma}\exp(-E/E_{\rm cut})$, where N is the photon flux) was preferred at the 3.5σ and 5.1σ level relative to a simple power-law model. The X-bulge had a spectral slope of $\Gamma = 1.9 \pm 0.1$, an energy cut-off $E_{\rm cut} = 10 \pm 5$ GeV, and a luminosity $L = (4.5 \pm 0.3) \times 10^{36}$ erg/s for $E \geq 100$ MeV (with uncertainties hereafter for this chapter stated at the 68% level). While for the nuclear bulge we have $\Gamma = 1.9 \pm 0.1$, $E_{\rm cut} = 13 \pm 4$ GeV and $L = (3.3 \pm 0.3) \times 10^{36}$ erg/s. With the X-bulge and nuclear bulge templates added to the baseline and new point sources, our NFW model of dark matter was not significantly detected. Swapping the X-bulge for the F98S model in this setup produced a qualitatively equivalent result for the NFW fit. Due to high Poisson noise in the Galactic plane for the bulge models, the analysis is likely to become increasingly insensitive to the bulge shape for latitudes within ~ 1 deg of the Galactic plane. The fairly similar improvements to the model produced by the X-bulge and boxy bulge (about 1.5 σ difference) which differ significantly within that latitude range may be the result of this. The luminosity estimate of the NFW fit in the baseline+NP+NFW model is consistent with previous estimates (Macias & Gordon, 2014). Changing the NFW slope to 1.0 did not qualitatively affect these results. In agreement with the results of Bartels et al. (2018) found independently of this work, the the Galactic bulge stellar distribution is preferred over a spherically symmetric NFW-squared excess template.

Table 3.1 Summary of the Likelihood analysis results

Base	Source	$\log(\mathcal{L}_{\text{Base}})$	$\log(\mathcal{L}_{\text{Base+Source}})$	$\text{TS}_{\text{Source}}$	σ	Number of source parameters
baseline	FB	-172461.4	-172422.3	78	6.9	19
baseline	NFW-s	-172461.4	-172265.3	392	18.4	19
baseline	F98S	-172461.4	-172238.7	445	19.7	19
baseline	X-bulge	-172461.4	-172224.1	475	20.5	19
baseline	NFW	-172461.4	-172167.9	587	23.0	19
baseline	NB	-172461.4	-171991.8	939	29.5	19
baseline	NP	-172461.4	-169804.1	5315	55.7	64×19
baseline+NP	FB	-169804.1	-169773.6	61	5.8	19
baseline+NP	NB	-169804.1	-169697.2	214	13.0	19
baseline+NP	F98S	-169804.1	-169663.7	281	15.3	19
baseline+NP	NFW	-169804.1	-169623.3	362	17.6	19
baseline+NP	X-bulge	-169804.1	-169616.2	376	18.0	19
baseline+NP+X-bulge	NFW	-169616.2	-169568.4	96	7.9	19
baseline+NP+X-bulge	NB	-169616.2	-169542.0	148	10.4	19
baseline+NP+X-bulge+NB	NFW	-169542.0	-169531.0	22	2.4	19
baseline+NP+X-bulge+NB	FB	-169542.0	-169525.5	33	3.5	19
baseline+NP+NB	X-bulge	-169697.2	-169542.0	310	16.1	19
baseline+NP+NB	F98S	-169697.2	-169566.0	262	14.6	19
baseline+NP+NFW	X-bulge+NB	-169623.3	-169531.0	185	10.8	2×19
baseline+NP+NFW+NB	X-bulge	-169598.9	-169531.0	136	9.9	19
baseline+NP+F98S+NB	NFW	-169566.0	-169553.3	25	2.7	19

The *baseline* model consists of all 3FGL point sources in the region of interest, Loop I, an ICS template predicted by GALPROP, the hydrodynamic-based gas annuli maps with the corresponding positive and negative dust residual maps, the recommended isotropic emission map, and a model for the Sun and the Moon. Other model templates considered are: the 64 new point sources (NP), the square of a generalised NFW profile with an inner slope $\gamma = 1.2$ or the square of a "standard NFW" (NFW-s) with inner slope $\gamma = 1$, an infrared X-bulge and a boxy bulge template tracing old stars in the Galactic bulge, a nuclear bulge (NB) template and a template accounting for the Fermi bubbles. The maximised likelihoods ($\mathcal{L}$) are given for the Base and Base+Source models and the significance of the new source is given by $\text{TS}_{\text{Source}} \equiv 2(\log(\mathcal{L}_{\text{Base+Source}}) - \log(\mathcal{L}_{\text{Base}}))$. Note that for both likelihoods all parameters are maximised and so the $\mathcal{L}_{\text{Base+Source}}$ will have additional parameters whose number is given in the last column of the table. The conversion between $\text{TS}_{\text{Source}}$ and σ is discussed in Section 3.4.5 and the point source component of Section 3.4.2.

The FB component using catenary curves did not qualitatively affect our results and produced a low TS value in our likelihood analysis pipeline.

3.4.7 CO To Molecular Hydrogen Conversion Factor

Our CO-to-H2 conversion factors, X_{CO}, are plotted in Fig. 3.9 for the corresponding Galactocentric annuli, along with the inferred radial X_{CO} distribution from Strong et al. (2004), and model ${}^{\text{S}}\text{L}^{\text{Z}}6^{\text{R}}20^{\text{T}}\infty\ {}^{\text{C}}5$ from Fig. 25 of Ackermann et al. (2012b). As in Ackermann et al. (2012b), our X_{CO} values in the outer Galaxy have exceedingly large uncertainties which we omit from display. Our conversion factors appear to follow the expected trend (Bolatto et al., 2013) of X_{CO} producing values several times smaller than the normally adopted global value of 2×10^{20} in the inner Galaxy, and CO becoming a weak tracer at larger radii. Performing our likelihood analysis with the 5 annuli bounds, similarly to Ackermann et al. (2017), produced the same qualitative results as above, however, due to the restricted ROI, the 0-1.5 kpc annulus produced an unrealistic X_{CO},

so we retained the 4 annuli approach. These X_{CO} values were not explicitly used in our analysis, but were rather derived as a consistency check with prior gamma-ray works on H2 contributions.

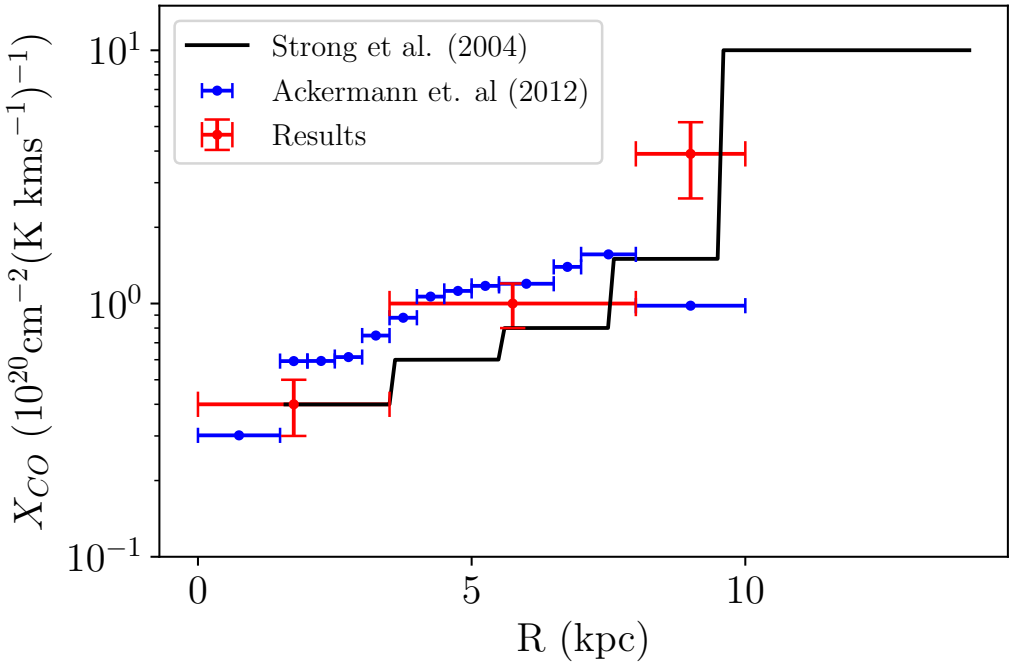

Fig. 3.9 (Red) CO to molecular hydrogen conversion factors (X_{CO}) by annulus excluding the outermost annulus. (Black) X_{CO} from the gamma-ray analysis in Strong et al. (2004). (Blue) Example X_{CO} radial distribution from Ackermann et al. (2012b). The horizontal error-bars in both cases cover the extent of the annuli for which the X_{CO} values were derived.

3.5 Applying our VVV Bulge Model

After expanding the ROI to $40^\circ \times 40^\circ$, the work of Macias et al. (2019) found the F98S model, described in Section 3.4.2, now provided the best fit to the Fermi GCE in a template fitting analysis rather than the X-bulge in the previous section. Better constraints on the DFGB normalisation with this expanded ROI may have lead to this distinction. In that work, a structured model of the Fermi bubbles derived by Ackermann et al. (2017) was used rather than the uniform catenary geometry, along with the newer 3D ICS models produced with GALPROP v56, both of which proved relevant to modelling the excess. The 2FIG catalogue for this ROI was now used in

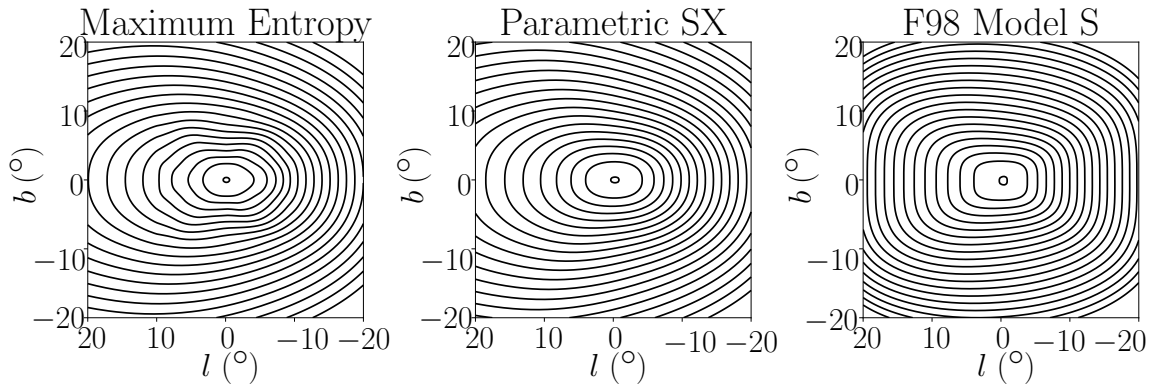

Fig. 3.10 Integrated density, $T(l,b) = \int \rho(s,l,b)\,\mathrm{d}s$, normalised with linearly spaced contours, for the maximum entropy deconvolution, the parametric SX prior density for the deconvolution and the parametric S-model of F98.

the baseline model rather than applying a point source search for potential candidates on top of the 3FGL in the likelihood analysis.

We created a template from our base parametric model and our non-parametric model fitted to the VVV data in Chapter 2 for comparison with the quality of the F98S template fit. We assumed that the density of MSPs is spatially correlated with the RC stellar density. The template (T) for the Fermi-LAT analysis needs to be proportional to the expected flux of the MSPs, so it was constructed using:

$$T(l,b) = \int_s \rho(s,l,b)\,\mathrm{d}s \tag{3.21}$$

where ρ is, as before, the RC+RGBB stellar density of the bulge. Note that an extra factor of s^2 is not necessary as this is the flux so whilst the number density is increasing as s^2 the observed flux is falling as s^2. We show a comparison between the F98S template and templates generated from our parametric and non-parametric fits in Fig. 3.10. Our non-parametric template has a noticeable peanut-like morphology. This may at first seem in contrast to the X-shaped morphology apparent from Fig. 2.12 for example. However, in that figure each slice in z is normalised by the maximum density in that slice. When no such normalisation is done the bulge has a more peanut-like morphology as can be seen from the third panel of the cross-sections in Fig. 3.11.

In fitting to the Fermi-LAT data, we followed the same method as Macias et al. (2019). The bulge template was fitted simultaneously with the resolved point sources, gas correlated templates, inverse-Compton templates (ICS-F98SA50) (Porter et al., 2017), Fermi bubbles templates, isotropic component, and Sun/Moon templates. The

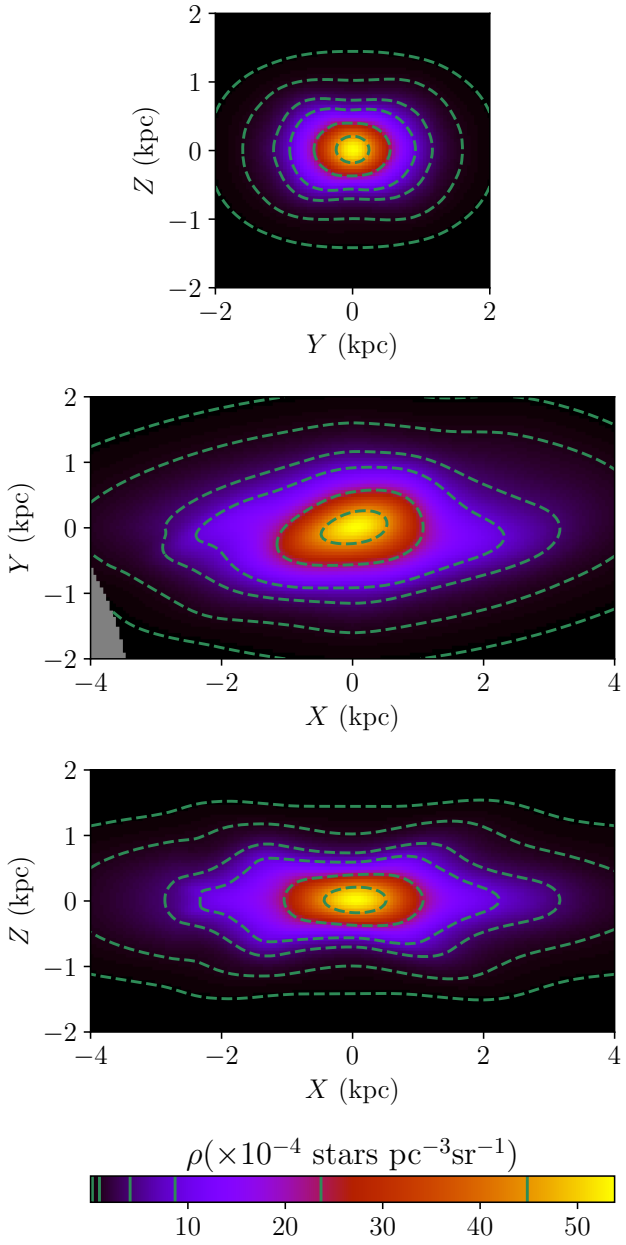

Fig. 3.11 Slices at the Galactic centre of the stellar density across different axis slices for our base non-parametric model. The 3 perpendicular axes are aligned along the bulge angle and centre using α and ΔR_0 from our best fitting parametric model for the base case. Where X is along the main axis of the bar and Z is perpendicular to the Galactic plane.

unresolved MSP Galactic disc component has been found to have an undetectable contribution (Bartels et al., 2018) and so we did not include it. The energy range of the photons used in the Fermi-LAT analysis was 667 MeV to 158 GeV, distributed over 15 logarithmically spaced energy bins. A $40^\circ \times 40^\circ$ region around the Galactic centre was used with $0.5^\circ \times 0.5^\circ$ pixels. This large region of interest was necessary to be able to constrain the background components. Also, no mask was used in the Fermi-LAT analysis. This made our non-parametric method of estimating the bulge from the VVV data particularly suitable as it allowed us to obtain an estimate of the bulge morphology over a $40^\circ \times 40^\circ$ area with no masked regions.

We evaluated the improvement to the fit to the Fermi-LAT data by working out $\mathrm{TS}_{\mathrm{Fermi}} = 2\log\mathcal{L}_{\mathrm{null}} - 2\log\mathcal{L}_{\mathrm{bulge}}$ where $\mathcal{L}_{\mathrm{null}}$ is the maximum likelihood with all the above mentioned templates' normalisations treated as free parameters in each of the 15 energy bands. $\mathcal{L}_{\mathrm{bulge}}$ is the maximum likelihood estimate using all the above mentioned templates and the the bulge template where the template normalisations were all fitted simultaneously. As we are making a non-nested model comparison here, Wilks' theorem does not directly apply, though lacking a suitable statistic we retain the 4σ detection threshold of $\mathrm{TS}_{\mathrm{Fermi}} \geq 34.8$ from the mixture distribution described in the previous analysis as a rough guide. For a more rigorous measure, many simulations should be performed for the modelling. In Table 3.2, we list the change in $\mathrm{TS}_{\mathrm{Fermi}}$ for the different bulge templates[1] we considered. The non-parametric template was preferred by the Fermi-LAT data, with $\Delta\mathrm{TS}_{\mathrm{Fermi}} = 177$ compared to the previous best-fitting template, F98S. A similar value was obtained when using an S-model fitted to the VVV data instead of F98S. Compared to our parametric SX template, our non-parametric template had $\Delta\mathrm{TS}_{\mathrm{Fermi}} = 65$. Our $40^\circ \times 40^\circ$ templates were significantly larger than the area covered by the VVV data. The extrapolated regions of the templates accounted for around half of the magnitude of the TS values listed in Table 3.2. Each successive enhancement in our bulge model, from S to SX to non-parametric, resulted in a steady improvement in the quality of fit to the Fermi data. This provides further evidence that the GCE traces the stellar content of the Galactic bulge. We found that the inferred gamma-ray energy spectra of the bulge was not very sensitive to the bulge morphology and was similar to previous analysis (Macias et al., 2019).

Contour plots of the data and two alternative models are shown in Fig. 3.12. The improvement of the fit when the Galactic bulge component is included is particularly noticeable around $(l,b) = (5^\circ, -5^\circ)$. The contribution of the Galactic bulge to the

[1] https://github.com/chrisgordon1/galactic_bulge_templates

Table 3.2 A comparison of the different bulge templates ability to explain the Fermi-LAT GCE. Where for model i, we list $\Delta TS_{Fermi} = 2\ln(\mathcal{L}_{nonparam}/\mathcal{L}_i)$.

Model	ΔTS_{Fermi}
Non-parametric bulge	0
SX bulge	65
S-bulge	177

Fermi-LAT model fit is shown in Fig. 3.13. The peanut nature for the bulge shape is evident in this figure, even after accounting for the PSF smoothing of the Fermi-LAT instrument. Around the $l = 5^\circ$ region there is a larger ratio of bulge to total signal than in other longitudes displayed. This helps in explaining why that area has one of the most noticeable improvements in fitting to the gamma-ray data presented in Fig. 3.12. Also, this figure shows how typically the bulge component is an order of magnitude smaller than the overall signal. This makes it hard to assign a statistical significance to the difference in ΔTS_{Fermi} values seen in Table 3.2, as small errors in the larger components could cause one template to be preferred over the other. One alternative method to account for this complication may be to use a maximum entropy non-parametric approach to modulate the larger components as handled by the SkyFACT method (Storm et al., 2017), which also found a preference for a boxy bulge model of the GCE in the Fermi-LAT data (Bartels et al., 2018).

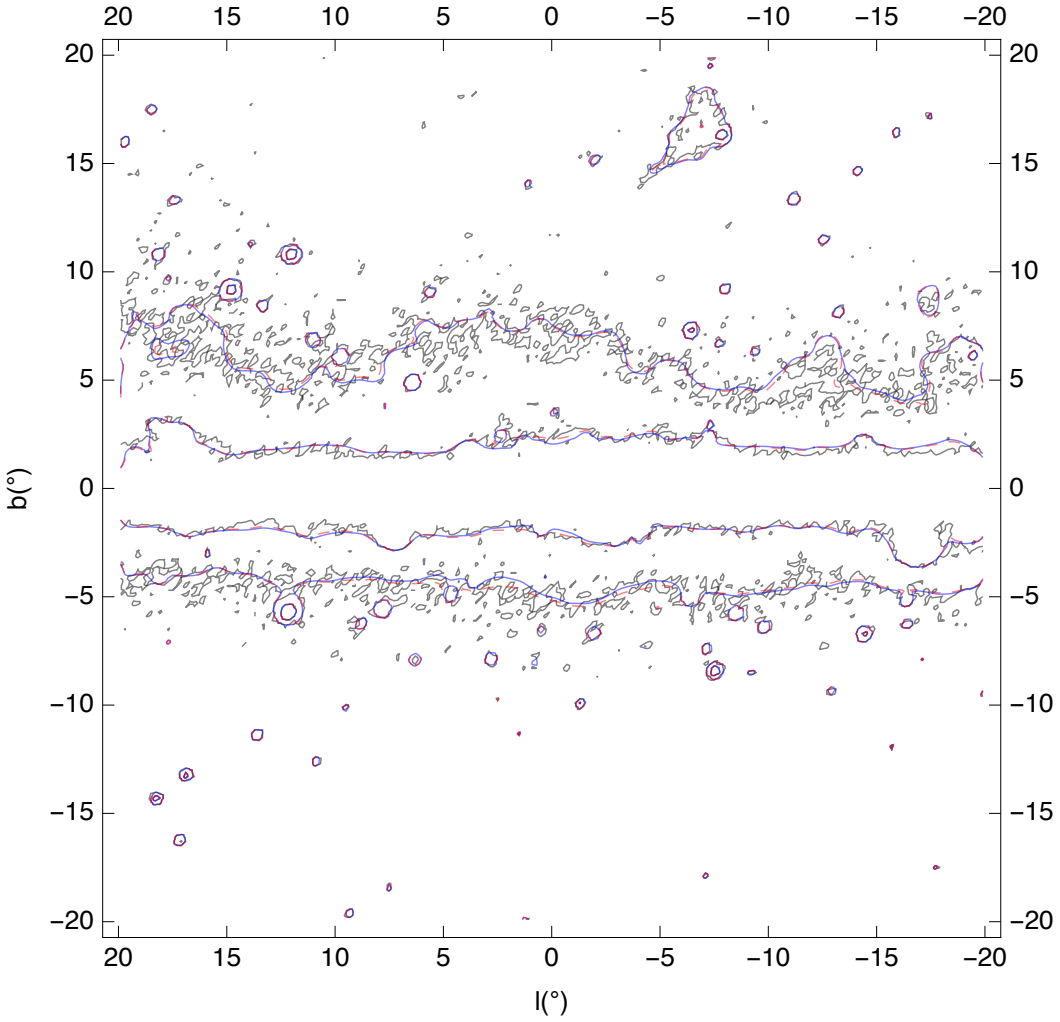

Fig. 3.12 Contours of the Fermi-LAT data (black), a model without a Galactic bulge (blue), and model with our non-parametric Galactic bulge (red, dashed). The energy range is 1.1 to 2.8 GeV and the contour levels are 750 and 2000 in units of photons per square degree.

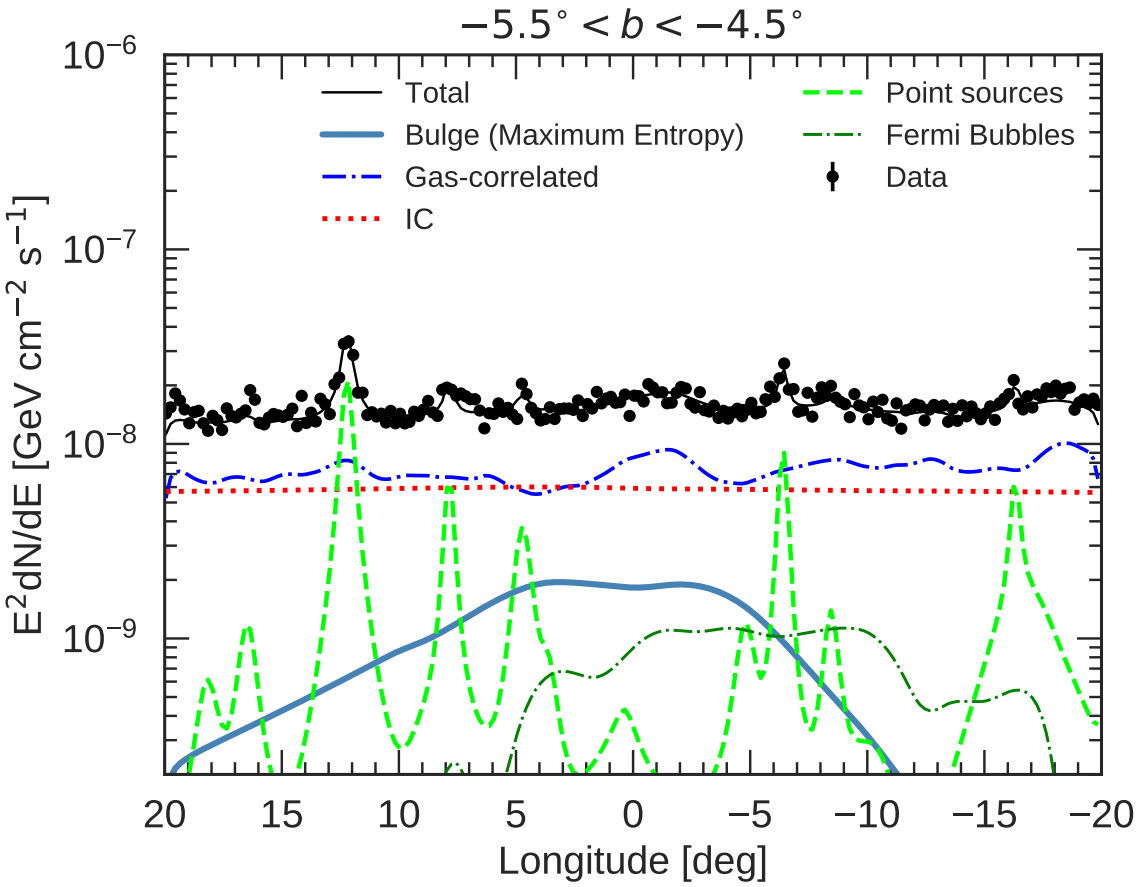

Fig. 3.13 Spatial distribution of the main model components included in the Fermi-LAT fit. The flux profiles in the energy range [1.1,2.8] GeV are displayed. Black dots represent the data and the continuous black line the total best-fitting model. Other components not shown here (*e.g.,* isotropic, Sun, Moon and Loop I) are $\sim \mathcal{O}(1)$ less bright in the region used to construct the profile.

3.6 Conclusions

Modelling the Fermi Galactic centre excess requires accurate models of the DFGB which dominates the sky in the GeV spectrum. Using hydrodynamic simulation-based gas deconvolution to accommodate the lack of kinematic resolution toward the Galactic centre, our initial likelihood tests with the 3FGL found these models provided a better fit to the gamma-ray spectrum than the circular velocity assumption method which requires interpolation in the central region of the Galaxy. Adding this to our baseline model of inverse-Compton, Loop I, isotropic emission and Sun/Moon emission, we compared several extended emission templates describing emission in the Galactic centre not accounted for by these standard components. On a $15^\circ \times 15^\circ$ region on the centre of the Galaxy, we found an X-shaped bulge extracted from the WISE data provided the best fit to the GCE, in particular, when combined with a nuclear bulge component. When the stellar distribution of the bulge region was accounted for by modelling the primary bulge component (as a boxy bulge or X-bulge) and the more central nuclear bulge, dark matter no longer provides a significant contribution to the gamma-ray excess.

On an expanded $40^\circ \times 40^\circ$ ROI the boxy bulge model provided the superior fit in a subsequent analysis. Building on this result, we applied the integrated density templates of our best fitting parametric SX and non-parametric bulge reconstructions using the VVV data. We found our non-parametric template provided a better fit than the F98S model which provided a good fit, disfavouring a dark matter interpretation, in our initial work and in the expanded ROI work. Our best parametric fit to the VVV data also improved on the quality of fit of the F98 S-bulge. This successive improvement using non-spherically distributed stellar bulge models is encouraging as further support of the bulge distributed population of unresolved millisecond pulsars interpretation of the GeV Galactic centre excess over a spherical dark matter halo distribution.

Chapter 4

Summary and Future Work

The reconstruction of stellar bulge distributions and their application in the context of observed anomalies in gamma-ray astronomy, in particular the Fermi GCE, were explored in this work. Deep photometric catalogues in the Near-Infrared band constructed from the VVV survey allowed us to see further into the structure of the Milky Way centre. The properties of RC stars enable distance estimates within a range dependent on age, metallicity, and an intrinsic magnitude dispersion when these other variables are fixed. We explored the use of several deconvolution techniques to model the inner bulge/bar distribution using RC stars. For all techniques we used, we required a luminosity function to describe the absolute magnitude distribution of red giant stars. Our primary luminosity function was constructed using a semi-analytic approach. Taking a bulge age of 10 Gyr and Gaussian distributed metallicity, [Fe/H], with dispersion of 0.4 and solar metallicity mean, we integrated the PARSEC isochrones of Marigo et al. (2017) for a Chabrier IMF. The Red Clump, Asymptotic Giant Branch Bump, and Red Giant Branch were computed separately using evolutionary flags in the isochrones. After subtracting an exponential from the RGB, we could model the RC and RGBB with their isochrone predicted distributions. In producing our North-South symmetrised models, a smoothed maximum entropy approach to fitting the background incorporated the remaining components into one general component along with the discs. We proposed a parametric SX model which typically tested reasonably effectively on realistic simulations and the real data set, but performed poorly on the real data set when a broad dispersion luminosity function was used. Building on this model, using it as a prior, we prepared a fully non-parametric maximum entropy regularised density reconstruction method with algorithmic smoothing in a likelihood optimisation. The hyper-parameters for our regularisers were tuned using simulations of the Galactic

bulge region with realistic disc and bulge models. Along with our best fit parametric SX and non-parametric bulge reconstructions, we performed a series of systematic tests on the robustness of our results. We modified the following aspects in our method to check their impact: the effect of not incorporating the feature behind the bulge into our background, our data mask choice, the background component modelling approach, the semi-analytic luminosity function, the metallicity distribution, the position of the Sun, and the non-parametric deconvolution method used. Barring the last systematic, we performed a TS comparison of all the other systematic checks for the parametric and non-parametric reconstructions for both simulations and real VVV data sets. The impact of these systematics was gauged by comparing the relative change in the TS of the fits between the data and simulation fits.

We derived several bulge properties from our best fit models and their systematics. Using a Chabrier IMF we estimated a total bulge stellar mass in the range 1.33-1.71 $\times 10^{10} M_{\odot}$ from our systematic non-parametric reconstructions on the VVV catalogue. Extracting the X-shaped component from our SX model and systematics, we found a contribution of $18-25\%$ to the bulge mass distribution and a bar angle ranging $18-32^{\circ}$ comparing favourably to the literature. The distance to the Galactic centre in our reconstructions based on the maximum bulge density was 7.9 kpc, from a mean absolute magnitude of the RC at -1.53 mag in K_s. Shifting the RC magnitude distribution to the observed mean RC absolute magnitude in K_s of -1.62 mag, the predicted distance to the Galactic centre becomes 8.24 kpc. Many of the systematics in this analysis were purely methodological in nature, preventing direct reduction in these systematics in future analyses. One systematic in particular that may be improved upon in future work is for the luminosity function. The broad luminosity function of S17 was applied in absence of an alternative systematic check. If the luminosity function were data driven by the bulge by simultaneously fitting the luminosity function and density, or as an iterative approach, the AGBB and RGBB would be accounted for, providing data based uncertainties in their values, allowing further confidence in the features adjacent to the bulge in addition to removing the most impactful systematic. Systematics such as the mask systematic are catalogue dependent. Zero-point correction of magnitudes as part of the catalogue construction and refinement of photometric errors would allow the confident use of a smaller mask.

As part of an exploratory analysis of structure in the data, we relaxed the assumptions that our non-parametric reconstruction match onto the prior outside the defined data region, and that the distribution be symmetric about the Galactic mid-plane. We add the AGBB and the RGB exponential back into our fit along with fitting the

thick and thin Besançon disc models. We identified a structure in front of the bar, ~ 3 kpc from the centre, providing a potential near side counterpart to the spiral arm structure behind the bar noted by Gonzalez et al. (2018) which we observed in our reconstruction on the far side of the bulge ~ 3 kpc from the Galactic centre. We assessed the sensitivity of this feature to the RGBB and AGBB components of the luminosity function. We doubled and zeroed the RGBB and AGBB to gauge the more extreme bounds on these features. The corresponding features behind and in front of the bulge, for these features distance modulus from the RC peak, decreased and increased for the respective doubling and zeroing of the RGBB and AGBB. Though remaining within more realistic systematic bounds would produce a much smaller effect.

Anomalous emission of gamma-rays has been observed in observations from Fermi-LAT. The Fermi Galactic centre excess had a spherically distributed signal after subtracting known gamma-ray emission contributions. Proposed explanations included dark matter, cosmic-ray bursts, and pulsars tracing such a morphology. The gamma-ray sky being dominated by cosmic-ray interactions with the interstellar medium necessitates careful modelling of this distribution to extract the morphological structure of the central excess. The main ISM processes contributing to the gamma-ray sky are inverse-Compton scattering, bremsstrahlung, and the decay of particles such as π^0. We focused on improving on the modelling of bremsstrahlung and π^0 decay via the gas distribution in the Milky Way. We diverged from the standard Fermi diffuse emission model by employing 3-D gas distribution models which were deconvolved using non-circular motions from the Galactic bar rotation to provide kinematic resolution towards the Galactic centre which is lacking when circular motion is assumed. To select our gas distribution model we fitted our hydrodynamic-based deconvolution model and circular-motion-based deconvolution separately to the Fermi data along with our baseline components of inverse-Compton template, Sun and Moon emission templates, an isotropic component, Loop I, and all 3FGL sources in our ROI. The hydrodynamic models performed better in these tests than the standard gas models previously used. Using our baseline model with hydrodynamic gas templates, we carried out a binned likelihood analysis of several extended emission templates: a nuclear bulge, a boxy triaxial bulge, the X-bulge extracted from the WISE observations, a uniform catenary bounded model of the Fermi bubbles, and an NFW dark matter template. In addition, we performed a search for point-source candidates not in the 3FGL which may prove to be a significant contributor to the emission. This component was added to the set of emission templates in the likelihood pipeline. Comparing these new point sources and 3FGL sources in our ROI to the 2FIG catalogue, released subsequent to our point

source scan, substantial overlap between the catalogues was observed. Employing a mixture distribution conversion of the template test statistics, the new point sources had the most significant contribution to the modelling on top of the baseline templates. On our $15^\circ \times 15^\circ$ region of interest, the Fermi bubbles template did not significantly improve the quality of our fit in this analysis. When both a nuclear bulge and stellar bulge, described by either a boxy S-bulge or the WISE X-bulge, are fitted, the dark matter distribution no longer has a significant contribution to the quality of fit. As these are spatial morphology templates we use, no direct nature of the source is gained for the stellar bulge templates other than the process producing the emission tracing such a morphology. We posit MSPs as a possible tracer of the stellar bulge, which may result from the production of MSPs within the bulge, though the current understanding of MSP production in the literature requires significant progress to determine whether or not this candidate holds up as an explanation. The main interpretation we may take from these results is that the excess does not exhibit a more spherical distribution which would be expected from dark matter annihilation.

A follow up treatment of the Fermi GCE used an expanded $40^\circ \times 40^\circ$ region of interest found the boxy S-bulge from Freudenreich (1998) was statistically preferred over the X-bulge distribution extracted from the WISE data, and the Fermi Bubbles now had a significant impact on the modelling. Using our parametric SX model and non-parametric model extracted from the VVV catalogue in a similar likelihood analysis, we found an improved likelihood fit by the parametric SX model over the S-bulge and further improvement by the even more data driven non-parametric reconstruction. This progressive improvement in fitting the gamma-ray data using deeper infrared surveys of the Galactic bulge distribution and increasingly data-driven methods is encouraging for the non-dark matter explanations of the GCE such as MSPs tracing the stellar distribution. Exploring alternative methods to the test statistic as a measure of significance for extended sources may be required to better gauge the impact of these improved stellar bulge models. One approach for improving on the gamma-ray analysis via more clearly understood statistical significance would involve simulation. By producing realistic Fermi data simulations with a known bulge component, the proposed bulge models may be fitted, producing a distribution of TSs. The distributions of TSs for each model can be compared to gauge significance.

In pursuit of further refinement of our modelling of the DFGB there are several natural extensions to our work. During the course of this work, the HI4PI survey of the 21-cm emission has been released which provides substantially finer resolution of the HI gas Doppler velocities. There also may be significant impact on GCE modelling

from the continuum emission in the 21-cm spectrum. We have begun to utilise these components as ways to improve our modelling with modification to the hydrodynamic deconvolution method.

References

Abazajian K. N., 2011, The consistency of Fermi-LAT observations of the galactic center with a millisecond pulsar population in the central stellar cluster, J. Cosmology Astropart. Phys., 2011, 010

Abazajian K. N., Kaplinghat M., 2012, Detection of a gamma-ray source in the Galactic Center consistent with extended emission from dark matter annihilation and concentrated astrophysical emission, Phys. Rev. D, 86, 083511

Abazajian K. N., Canac N., Horiuchi S., Kaplinghat M., 2014, Astrophysical and dark matter interpretations of extended gamma-ray emission from the Galactic Center, Phys. Rev. D, 90, 023526

Abdo A. A., et al., 2013, The Second Fermi Large Area Telescope Catalog of Gamma-Ray Pulsars, ApJS, 208, 17

Acero F., et al., 2015, Fermi Large Area Telescope Third Source Catalog, ApJS, 218, 23

Acero F., et al., 2016, Development of the Model of Galactic Interstellar Emission for Standard Point-source Analysis of Fermi Large Area Telescope Data, ApJS, 223, 26

Ackermann M., et al., 2012a, The Fermi Large Area Telescope on Orbit: Event Classification, Instrument Response Functions, and Calibration, ApJS, 203, 4

Ackermann M., et al., 2012b, Fermi-LAT Observations of the Diffuse γ-Ray Emission: Implications for Cosmic Rays and the Interstellar Medium, The Astrophysical Journal, 750, 3

Ackermann M., et al., 2014, The Spectrum and Morphology of the Fermi Bubbles, ApJ, 793, 64

Ackermann M., et al., 2017, The Fermi Galactic Center GeV Excess and Implications for Dark Matter, ApJ, 840, 43

Ajello M., et al., 2016, Fermi-LAT Observations of High-Energy Gamma-Ray Emission toward the Galactic Center, ApJ, 819, 44

Alonso-García J., et al., 2018, Milky Way demographics with the VVV survey. IV. PSF photometry from almost one billion stars in the Galactic bulge and adjacent southern disk, A&A, 619, A4

Alpar M. A., Cheng A. F., Ruderman M. A., Shaham J., 1982, A new class of radio pulsars, Nature, 300, 728

Araki S., 1985, PhD thesis, MIT., http://hdl.handle.net/1721.1/80445

Athanassoula E., 2005, On the nature of bulges in general and of box/peanut bulges in particular: input from N-body simulations, MNRAS, 358, 1477

Athanassoula E., Morin S., Wozniak H., Puy D., Pierce M. J., Lombard J., Bosma A., 1990, The shape of bars in early-type barred galaxies., MNRAS, 245, 130

Atwood W. B., et al., 2009, The Large Area Telescope on the Fermi Gamma-Ray Space Telescope Mission, ApJ, 697, 1071

Baade W., 1946, A Search For the Nucleus of Our Galaxy, PASP, 58, 249

Babusiaux C., 2016, Correlations between Kinematics and Metallicity in the Galactic Bulge: A Review, Publ. Astron. Soc. Australia, 33, e026

Babusiaux C., et al., 2010, Insights on the Milky Way bulge formation from the correlations between kinematics and metallicity, A&A, 519, A77

Bartels R., Storm E., Weniger C., Calore F., 2018, The Fermi-LAT GeV excess as a tracer of stellar mass in the Galactic bulge, Nature Astronomy, 2, 819

Bergström L., 2012, Dark matter evidence, particle physics candidates and detection methods, Annalen der Physik, 524, 479

Bergström L., Ullio P., Buckley J. H., 1998, Observability of γ rays from dark matter neutralino annihilations in the Milky Way halo, Astroparticle Physics, 9, 137

Binney J., Merrifield M., 1998, Galactic Astronomy. Princeton University Press

Binney J., Gerhard O. E., Stark A. A., Bally J., Uchida K. I., 1991, Understanding the kinematics of Galactic centre gas, MNRAS, 252, 210

Bissantz N., Gerhard O., 2002, Spiral arms, bar shape and bulge microlensing in the Milky Way, MNRAS, 330, 591

Bissantz N., Englmaier P., Binney J., Gerhard O., 1997, The microlensing optical depth of the COBE bulge, MNRAS, 289, 651

Bissantz N., Englmaier P., Gerhard O., 2003, Gas dynamics in the Milky Way: second pattern speed and large-scale morphology, MNRAS, 340, 949

Blitz L., Spergel D. N., 1991, Direct evidence for a bar at the Galactic center, ApJ, 379, 631

Bolatto A. D., Wolfire M., Leroy A. K., 2013, The CO-to-H_2 Conversion Factor, ARA&A, 51, 207

Boyarsky A., Malyshev D., Ruchayskiy O., 2011, A comment on the emission from the Galactic Center as seen by the Fermi telescope, Physics Letters B, 705, 165

Burbidge E. M., Burbidge G. R., 1959, Three Unusual so Galaxies., ApJ, 130, 20

Calore F., Cholis I., McCabe C., Weniger C., 2015a, A tale of tails: Dark matter interpretations of the Fermi GeV excess in light of background model systematics, Phys. Rev. D, 91, 063003

Calore F., Cholis I., Weniger C., 2015b, Background model systematics for the Fermi GeV excess, J. Cosmology Astropart. Phys., 2015, 038

Cao L., Mao S., Nataf D., Rattenbury N. J., Gould A., 2013, A new photometric model of the Galactic bar using red clump giants, MNRAS, 434, 595

Carlson E., Profumo S., Linden T., 2016, Cosmic-Ray Injection from Star-Forming Regions, Phys. Rev. Lett., 117, 111101

Casandjian J.-M., 2015, The Fermi-LAT model of interstellar emission for standard point source analysis, arXiv e-prints, p. arXiv:1502.07210

Chabrier G., 2003, Galactic Stellar and Substellar Initial Mass Function, PASP, 115, 763

Chan V. C., Bovy J., 2019, The Gaia DR2 parallax zero point: Hierarchical modeling of red clump stars, arXiv e-prints, p. arXiv:1910.00398

Chernoff H., 1954, On the distribution of the likelihood ratio, Ann. Math. Statist., 25, 573

Cholis I., Evoli C., Calore F., Linden T., Weniger C., Hooper D., 2015, The Galactic Center GeV excess from a series of leptonic cosmic-ray outbursts, J. Cosmology Astropart. Phys., 2015, 005

Ciambur B. C., Graham A. W., 2016, Quantifying the (X/peanut)-shaped structure in edge-on disc galaxies: length, strength, and nested peanuts, MNRAS, 459, 1276

Clarke J. P., Wegg C., Gerhard O., Smith L. C., Lucas P. W., Wylie S. M., 2019, The Milky Way bar/bulge in proper motions: a 3D view from VIRAC & Gaia, arXiv e-prints, p. arXiv:1903.02003

Clarkson W. I., et al., 2011, The First Detection of Blue Straggler Stars in the Milky Way Bulge, ApJ, 735, 37

Clemens D. P., 1985, Massachusetts-Stony Brook Galactic plane CO survey: the galactic disk rotation curve., ApJ, 295, 422

Coleman B., Paterson D., Gordon C., Macias O., Ploeg H., 2020, Maximum entropy estimation of the Galactic bulge morphology via the VVV Red Clump, MNRAS, 495, 3350

Combes F., Sanders R. H., 1981, Formation and properties of persisting stellar bars., A&A, 96, 164

Combes F., Debbasch F., Friedli D., Pfenniger D., 1990, Box and peanut shapes generated by stellar bars., A&A, 233, 82

Dame T. M., Hartmann D., Thaddeus P., 2001, The Milky Way in Molecular Clouds: A New Complete CO Survey, ApJ, 547, 792

Daylan T., Finkbeiner D. P., Hooper D., Linden T., Portillo S. K. N., Rodd N. L., Slatyer T. R., 2016, The characterization of the gamma-ray signal from the central Milky Way: A case for annihilating dark matter, Physics of the Dark Universe, 12, 1

Degrange B., Fontaine G., 2015, Introduction to high-energy gamma-ray astronomy, Comptes Rendus Physique, 16, 587

Dehnen W., Binney J. J., 1998, Local stellar kinematics from HIPPARCOS data, MNRAS, 298, 387

Dékány I., Minniti D., Catelan M., Zoccali M., Saito R. K., Hempel M., Gonzalez O. A., 2013, VVV Survey Near-infrared Photometry of Known Bulge RR Lyrae Stars: The Distance to the Galactic Center and Absence of a Barred Distribution of the Metal-poor Population, ApJ, 776, L19

Delahaye T., Fiasson A., Pohl M., Salati P., 2011, The GeV-TeV Galactic gamma-ray diffuse emission. I. Uncertainties in the predictions of the hadronic component, A&A, 531, A37

Dickey J. M., Lockman F. J., 1990, H I in the galaxy., ARA&A, 28, 215

Dwek E., et al., 1995, Morphology, near-infrared luminosity, and mass of the Galactic bulge from COBE DIRBE observations, ApJ, 445, 716

Einasto J., 1979, in Burton W. B., ed., IAU Symposium Vol. 84, The Large-Scale Characteristics of the Galaxy. pp 451–458

Erwin P., et al., 2015, Composite bulges: the coexistence of classical bulges and discy pseudo-bulges in S0 and spiral galaxies, MNRAS, 446, 4039

Fermi-LAT Collaboration 2017, Characterizing the population of pulsars in the inner Galaxy with the Fermi Large Area Telescope, arXiv e-prints, p. arXiv:1705.00009

Ferrière K. M., 2001, The interstellar environment of our galaxy, Reviews of Modern Physics, 73, 1031

Ferrière K., Gillard W., Jean P., 2007, Spatial distribution of interstellar gas in the innermost 3 kpc of our galaxy, A&A, 467, 611

Field G. B., 1959, The Spin Temperature of Intergalactic Neutral Hydrogen., ApJ, 129, 536

Fragione G., Antonini F., Gnedin O. Y., 2018, Disrupted globular clusters and the gamma-ray excess in the Galactic Centre, MNRAS, 475, 5313

Freudenreich H. T., 1998, A COBE Model of the Galactic Bar and Disk, ApJ, 492, 495

Gaensler B. M., Madsen G. J., Chatterjee S., Mao S. A., 2008, The Vertical Structure of Warm Ionised Gas in the Milky Way, Publ. Astron. Soc. Australia, 25, 184

Gaggero D., Valli M., 2018, Impact of cosmic-ray physics on dark matter indirect searches, arXiv e-prints, p. arXiv:1802.00636

Gaggero D., Taoso M., Urbano A., Valli M., Ullio P., 2015, Towards a realistic astrophysical interpretation of the gamma-ray Galactic center excess, J. Cosmology Astropart. Phys., 2015, 056

García Pérez A. E., et al., 2018, The Bulge Metallicity Distribution from the APOGEE Survey, ApJ, 852, 91

Gardner E., Debattista V. P., Robin A. C., Vásquez S., Zoccali M., 2014, N-body simulation insights into the X-shaped bulge of the Milky Way: kinematics and distance to the Galactic Centre, MNRAS, 438, 3275

Girardi L., 1999, A secondary clump of red giant stars: why and where, MNRAS, 308, 818

Girardi L., 2016, Red Clump Stars, ARA&A, 54, 95

Gonzalez O. A., et al., 2018, The structure behind the Galactic bar traced by red clump stars in the VVV survey, MNRAS, 481, L130

Goodenough L., Hooper D., 2009, Possible Evidence For Dark Matter Annihilation In The Inner Milky Way From The Fermi Gamma Ray Space Telescope, arXiv e-prints, p. arXiv:0910.2998

Gordon C., Macías O., 2013, Dark matter and pulsar model constraints from Galactic Center Fermi-LAT gamma-ray observations, Phys. Rev. D, 88, 083521

Gravity Collaboration et al., 2019, A geometric distance measurement to the Galactic center black hole with 0.3% uncertainty, A&A, 625, L10

Grenier I. A., Casandjian J.-M., Terrier R., 2005, Unveiling Extensive Clouds of Dark Gas in the Solar Neighborhood, Science, 307, 1292

Hajdu G., Dékány I., Catelan M., Grebel E. K., 2019, On the optimal calibration of VVV photometry, arXiv e-prints, p. arXiv:1908.06160

Hall O. J., et al., 2019, Testing asteroseismology with Gaia DR2: hierarchical models of the Red Clump, MNRAS, 486, 3569

Harris W. E., 2010, A New Catalog of Globular Clusters in the Milky Way, arXiv e-prints, p. arXiv:1012.3224

He C., Ng C. Y., Kaspi V. M., 2013, The Correlation between Dispersion Measure and X-Ray Column Density from Radio Pulsars, ApJ, 768, 64

Heiles C., Troland T. H., 2003, The Millennium Arecibo 21 Centimeter Absorption-Line Survey. II. Properties of the Warm and Cold Neutral Media, ApJ, 586, 1067

Hohl F., 1971, Numerical Experiments with a Disk of Stars, ApJ, 168, 343

Hooper D., Linden T., 2011, Origin of the gamma rays from the Galactic Center, Phys. Rev. D, 84, 123005

Hui C. Y., Cheng K. S., Taam R. E., 2010, Dynamical Formation of Millisecond Pulsars in Globular Clusters, ApJ, 714, 1149

Israel F. P., 1997, H_2 and its relation to CO in the LMC and other magellanic irregular galaxies, A&A, 328, 471

Jaynes E. T., 1957, Information Theory and Statistical Mechanics, Physical Review, 106, 620

Johannesson G., Orlando E., 2013, in International Cosmic Ray Conference. p. 3106 (arXiv:1307.0197)

Jungman G., Kamionkowski M., Griest K., 1996, Supersymmetric dark matter, Phys. Rep., 267, 195

Kalberla P. M. W., Kerp J., 2009, The Hi Distribution of the Milky Way, ARA&A, 47, 27

Kalberla P. M. W., Burton W. B., Hartmann D., Arnal E. M., Bajaja E., Morras R., Pöppel W. G. L., 2005, The Leiden/Argentine/Bonn (LAB) Survey of Galactic HI. Final data release of the combined LDS and IAR surveys with improved stray-radiation corrections, A&A, 440, 775

Knödlseder J., 2016, The future of gamma-ray astronomy, Comptes Rendus Physique, 17, 663

Kormendy J., 2016, in Laurikainen E., Peletier R., Gadotti D., eds, Astrophysics and Space Science Library Vol. 418, Galactic Bulges. p. 431 (arXiv:1504.03330), doi:10.1007/978-3-319-19378-6_16

Kormendy J., Kennicutt Robert C. J., 2004, Secular Evolution and the Formation of Pseudobulges in Disk Galaxies, ARA&A, 42, 603

Kunder A., et al., 2016, Before the Bar: Kinematic Detection of a Spheroidal Metal-poor Bulge Component, ApJ, 821, L25

Laurikainen E., Salo H., Athanassoula E., Bosma A., Herrera-Endoqui M., 2014, Milky Way mass galaxies with X-shaped bulges are not rare in the local Universe., MNRAS, 444, L80

Lee Y.-W., Joo S.-J., Chung C., 2015, The Milky Way without X: an alternative interpretation of the double red clump in the Galactic bulge, MNRAS, 453, 3906

Lee Y.-W., Kim J. J., Johnson C. I., Chung C., Jang S., Lim D., Kang Y., 2019, The Globular Cluster Origin of the Milky Way Outer Bulge: Evidence from Sodium Bimodality, ApJ, 878, L2

Levine E. S., Blitz L., Heiles C., 2006, The Vertical Structure of the Outer Milky Way H I Disk, ApJ, 643, 881

López-Corredoira M., 2016, A case against an X-shaped structure in the Milky Way young bulge, A&A, 593, A66

López-Corredoira M., 2017, Absence of an X-shaped Structure in the Milky Way Bulge Using Mira Variable Stars, ApJ, 836, 218

López-Corredoira M., Hammersley P. L., Garzón F., Simonneau E., Mahoney T. J., 2000, Inversion of stellar statistics equation for the Galactic bulge, MNRAS, 313, 392

López-Corredoira M., Lee Y. W., Garzón F., Lim D., 2019, Distribution of red clump stars does not support the X-shaped Galactic bulge, A&A, 627, A3

Macias O., Gordon C., 2014, Contribution of cosmic rays interacting with molecular clouds to the Galactic Center gamma-ray excess, Phys. Rev. D, 89, 063515

Macias O., Gordon C., Crocker R. M., Coleman B., Paterson D., Horiuchi S., Pohl M., 2018, Galactic bulge preferred over dark matter for the Galactic centre gamma-ray excess, Nature Astronomy, 2, 387

Macias O., Horiuchi S., Kaplinghat M., Gordon C., Crocker R. M., Nataf D. M., 2019, Strong evidence that the galactic bulge is shining in gamma rays, J. Cosmology Astropart. Phys., 2019, 042

Maraston C., 1998, Evolutionary synthesis of stellar populations: a modular tool, MNRAS, 300, 872

Marigo P., et al., 2017, A New Generation of PARSEC-COLIBRI Stellar Isochrones Including the TP-AGB Phase, ApJ, 835, 77

Martinez-Valpuesta I., Gerhard O., 2011, Unifying A Boxy Bulge and Planar Long Bar in the Milky Way, ApJ, 734, L20

Mattox J. R., et al., 1996, The Likelihood Analysis of EGRET Data, ApJ, 461, 396

Mauro F., Moni Bidin C., Chené A. N., Geisler D., Alonso-García J., Borissova J., Carraro G., 2013, The VVV-SkZ_pipeline: an automatic PSF-fitting photometric pipeline for the VVV survey, Rev. Mex. Astron. Astrofis., 49, 189

McWilliam A., Zoccali M., 2010, Two Red Clumps and the X-shaped Milky Way Bulge, ApJ, 724, 1491

Minniti D., Zoccali M., 2008, in Bureau M., Athanassoula E., Barbuy B., eds, IAU Symposium Vol. 245, Formation and Evolution of Galaxy Bulges. pp 323–332 (arXiv:0710.3104), doi:10.1017/S1743921308018048

Minniti D., et al., 2010, VISTA Variables in the Via Lactea (VVV): The public ESO near-IR variability survey of the Milky Way, New Astron., 15, 433

Miwa T., Noguchi M., 1998, Dynamical Properties of Tidally Induced Galactic Bars, ApJ, 499, 149

Nataf D. M., 2016, The Controversial Star-Formation History and Helium Enrichment of the Milky Way Bulge, Publ. Astron. Soc. Australia, 33, e023

Nataf D. M., Udalski A., Gould A., Fouqué P., Stanek K. Z., 2010, The Split Red Clump of the Galactic Bulge from OGLE-III, ApJ, 721, L28

Nataf D. M., Udalski A., Gould A., Pinsonneault M. H., 2011, OGLE-III Detection of the Anomalous Galactic Bulge Red Giant Branch Bump: Evidence of Enhanced Helium Enrichment, ApJ, 730, 118

Navarro J. F., Frenk C. S., White S. D. M., 1996, The Structure of Cold Dark Matter Halos, ApJ, 462, 563

Ness M., Freeman K., 2016, The Metallicity Distribution of the Milky Way Bulge, Publ. Astron. Soc. Australia, 33, e022

Ness M., Lang D., 2016, The X-shaped Bulge of the Milky Way Revealed by WISE, AJ, 152, 14

Ness M., et al., 2013, ARGOS - IV. The kinematics of the Milky Way bulge, MNRAS, 432, 2092

Nishiyama S., et al., 2013, Magnetically Confined Interstellar Hot Plasma in the Nuclear Bulge of Our Galaxy, ApJ, 769, L28

Olling R. P., Merrifield M. R., 1998, Refining the Oort and Galactic constants, MNRAS, 297, 943

Paterson D., Coleman B., Gordon C., 2019, Further evidence that the Milky Way bar has undergone a buckling phase, arXiv e-prints, p. arXiv:1911.04716

Pfenniger D., Friedli D., 1991, Structure and dynamics of 3D N-body barred galaxies., A&A, 252, 75

Pietrinferni A., Cassisi S., Salaris M., Castelli F., 2004, A Large Stellar Evolution Database for Population Synthesis Studies. I. Scaled Solar Models and Isochrones, ApJ, 612, 168

Planck Collaboration et al., 2018, Planck 2018 results. VI. Cosmological parameters, arXiv e-prints, p. arXiv:1807.06209

Ploeg H., Gordon C., Crocker R., Macias O., 2017, Consistency between the luminosity function of resolved millisecond pulsars and the galactic center excess, J. Cosmology Astropart. Phys., 2017, 015

Pohl M., Englmaier P., Bissantz N., 2008, Three-Dimensional Distribution of Molecular Gas in the Barred Milky Way, ApJ, 677, 283

Portail M., Wegg C., Gerhard O., Martinez-Valpuesta I., 2015a, Made-to-measure models of the Galactic box/peanut bulge: stellar and total mass in the bulge region, MNRAS, 448, 713

Portail M., Wegg C., Gerhard O., 2015b, Peanuts, brezels and bananas: food for thought on the orbital structure of the Galactic bulge, MNRAS, 450, L66

Portail M., Gerhard O., Wegg C., Ness M., 2017, Dynamical modelling of the galactic bulge and bar: the Milky Way's pattern speed, stellar and dark matter mass distribution, MNRAS, 465, 1621

Porter T. A., Jóhannesson G., Moskalenko I. V., 2017, High-energy Gamma Rays from the Milky Way: Three-dimensional Spatial Models for the Cosmic-Ray and Radiation Field Densities in the Interstellar Medium, ApJ, 846, 67

Raha N., Sellwood J. A., James R. A., Kahn F. D., 1991, A dynamical instability of bars in disk galaxies, Nature, 352, 411

Rattenbury N. J., Mao S., Sumi T., Smith M. C., 2007, Modelling the Galactic bar using OGLE-II red clump giant stars, MNRAS, 378, 1064

Renaud F., et al., 2013, A sub-parsec resolution simulation of the Milky Way: global structure of the interstellar medium and properties of molecular clouds, MNRAS, 436, 1836

Robin A. C., Reylé C., Derrière S., Picaud S., 2003, A synthetic view on structure and evolution of the Milky Way, A&A, 409, 523

Rojas-Arriagada A., et al., 2014, The Gaia-ESO Survey: metallicity and kinematic trends in the Milky Way bulge, A&A, 569, A103

Saha K., Gerhard O., 2013, Secular evolution and cylindrical rotation in boxy/peanut bulges: impact of initially rotating classical bulges, MNRAS, 430, 2039

Saito R. K., Zoccali M., McWilliam A., Minniti D., Gonzalez O. A., Hill V., 2011, Mapping the X-shaped Milky Way Bulge, AJ, 142, 76

Saito R. K., et al., 2012, VVV DR1: The first data release of the Milky Way bulge and southern plane from the near-infrared ESO public survey VISTA variables in the Vía Láctea, A&A, 537, A107

Sanders J. L., Smith L., Evans N. W., Lucas P., 2019, Transverse kinematics of the Galactic bar-bulge from VVV and Gaia, MNRAS, p. 1626

Schechter P. L., Mateo M., Saha A., 1993, DoPHOT, A CCD Photometry Program: Description and Tests, PASP, 105, 1342

Schlegel D. J., Finkbeiner D. P., Davis M., 1998, Maps of Dust Infrared Emission for Use in Estimation of Reddening and Cosmic Microwave Background Radiation Foregrounds, ApJ, 500, 525

Self S. G., Liang K.-Y., 1987, Asymptotic properties of maximum likelihood estimators and likelihood ratio tests under nonstandard conditions, Journal of the American Statistical Association, 82, 605

Sellwood J. A., 1989, Meta-stability in galactic discs, MNRAS, 238, 115

Sellwood J. A., 2014, Secular evolution in disk galaxies, Reviews of Modern Physics, 86, 1

Sharma S., Bland-Hawthorn J., Johnston K. V., Binney J., 2011, Galaxia: A Code to Generate a Synthetic Survey of the Milky Way, ApJ, 730, 3

Shaver P. A., McGee R. X., Newton L. M., Danks A. C., Pottasch S. R., 1983, The galactic abundance gradient., MNRAS, 204, 53

Shen J., Rich R. M., Kormendy J., Howard C. D., De Propris R., Kunder A., 2010, Our Milky Way as a Pure-disk Galaxy—A Challenge for Galaxy Formation, ApJ, 720, L72

Simion I. T., Belokurov V., Irwin M., Koposov S. E., Gonzalez-Fernandez C., Robin A. C., Shen J., Li Z. Y., 2017, A parametric description of the 3D structure of the Galactic bar/bulge using the VVV survey, MNRAS, 471, 4323

Skrutskie M. F., et al., 2006, The Two Micron All Sky Survey (2MASS), AJ, 131, 1163

Smartt S. J., Venn K. A., Dufton P. L., Lennon D. J., Rolleston W. R. J., Keenan F. P., 2001, Chemical abundances in the inner 5 kpc of the Galactic disk, A&A, 367, 86

Sodroski T. J., et al., 1995, The Ratio of H 2 Column Density to 12CO Intensity in the Vicinity of the Galactic Center, ApJ, 452, 262

Solomon P. M., Barrett J. W., 1991, in Combes F., Casoli F., eds, IAU Symposium Vol. 146, Dynamics of Galaxies and Their Molecular Cloud Distributions. p. 235

Spera M., Mapelli M., Bressan A., 2015, The mass spectrum of compact remnants from the PARSEC stellar evolution tracks, MNRAS, 451, 4086

Spergel D. N., Malhotra S., Blitz L., 1996, in Minniti D., Rix H.-W., eds, Spiral Galaxies in the Near-IR. p. 128, doi:10.1007/978-3-540-49739-4_19

Stanek K. Z., Udalski A., Szymański M., Kałużny J., Kubiak Z. M., Mateo M., Krzemiński W., 1997, Modeling the Galactic Bar Using Red Clump Giants, ApJ, 477, 163

Steinmetz M., Muller E., 1995, The formation of disc galaxies in a cosmological context: structure and kinematics, MNRAS, 276, 549

Steinmetz M., Navarro J. F., 2002, The hierarchical origin of galaxy morphologies, New Astron., 7, 155

Stetson P. B., 1987, DAOPHOT: A Computer Program for Crowded-Field Stellar Photometry, PASP, 99, 191

Stetson P. B., 1994, The Center of the Core-Cusp Globular Cluster M15: CFHT and HST Observations, ALLFRAME Reductions, PASP, 106, 250

Storm E., Weniger C., Calore F., 2017, SkyFACT: high-dimensional modeling of gamma-ray emission with adaptive templates and penalized likelihoods, J. Cosmology Astropart. Phys., 2017, 022

Strong A. W., Moskalenko I. V., Reimer O., 2000, Diffuse Continuum Gamma Rays from the Galaxy, ApJ, 537, 763

Strong A. W., Moskalenko I. V., Reimer O., Digel S., Diehl R., 2004, The distribution of cosmic-ray sources in the Galaxy, γ-rays and the gradient in the CO-to-H_2 relation, A&A, 422, L47

Strong A. W., Moskalenko I. V., Porter T. A., Jóhannesson G., Orlando E., Digel S. W., 2010, GALPROP: Code for Cosmic-ray Transport and Diffuse Emission Production (ascl:1010.028)

Strong A. W., Orlando E., Jaffe T. R., 2011, VizieR Online Data Catalog: GALPROP programme (Strong+, 2011), VizieR Online Data Catalog, pp J/A+A/534/A54

Surot F., et al., 2019, Mapping the stellar age of the Milky Way bulge with the VVV. II. Deep JKs catalogs release based on PSF photometry, arXiv e-prints, p. arXiv:1907.01972

Toomre A., 1966, in Geophysical Fluid Dynamics, notes on the 1966 Summer Study Program in Geophysical Fluid Dynamics at the Woods Hole Oceanographic Institution, ref. no. 66-46, p. 111

Udalski A., Szymanski M., Kaluzny J., Kubiak M., Mateo M., 1992, The Optical Gravitational Lensing Experiment, Acta Astron., 42, 253

Vásquez S., et al., 2013, 3D kinematics through the X-shaped Milky Way bulge, A&A, 555, A91

Wegg C., Gerhard O., 2013, Mapping the three-dimensional density of the Galactic bulge with VVV red clump stars, MNRAS, 435, 1874

Wegg C., Gerhard O., Portail M., 2015, The structure of the Milky Way's bar outside the bulge, MNRAS, 450, 4050

Weiland J. L., et al., 1994, COBE diffuse infrared background experiment observations of the galactic bulge, ApJ, 425, L81

Westerhout G., 1957, The distribution of atomic hydrogen in the outer parts of the Galactic System, Bull. Astron. Inst. Netherlands, 13, 201

Wilks S. S., 1938, The large-sample distribution of the likelihood ratio for testing composite hypotheses, Ann. Math. Statist., 9, 60

Wilson T. L., Rohlfs K., Hüttemeister S., 2009, Tools of Radio Astronomy. Springer Berlin Heidelberg, doi:10.1007/978-3-540-85122-6

Wolleben M., 2007, A New Model for the Loop I (North Polar Spur) Region, ApJ, 664, 349

Zoccali M., Valenti E., 2016, The 3D Structure of the Galactic Bulge, Publ. Astron. Soc. Australia, 33, e025

Zoccali M., Hill V., Lecureur A., Barbuy B., Renzini A., Minniti D., Gómez A., Ortolani S., 2008, The metal content of bulge field stars from FLAMES-GIRAFFE spectra. I. Stellar parameters and iron abundances, A&A, 486, 177

Zoccali M., et al., 2017, The GIRAFFE Inner Bulge Survey (GIBS). III. Metallicity distributions and kinematics of 26 Galactic bulge fields, A&A, 599, A12

de Vaucouleurs G., 1964, in Kerr F. J., ed., IAU Symposium Vol. 20, The Galaxy and the Magellanic Clouds. p. 195